OCT Guided Micro-Vascular Robotic Surgery:
Design, Calibration and Telemanipulation

By

Haoran Yu

Dissertation

Submitted to the Faculty of the

Graduate School of Vanderbilt University

in partial fulfillment of the requirements

for the degree of

DOCTOR OF PHILOSOPHY

in

Mechanical Engineering

August, 2016

Nashville, Tennessee

Approved:

Nabil Simaan, Ph.D.

Nilanjan Sarkar, Ph.D.

Karen Joos, Ph.D., M.D.

Pietro Valdastri, Ph.D.

Karl Zelik, Ph.D.

To my parents and my wife,

who supported and encouraged me

throughout the creation of this dissertation.

ACKNOWLEDGMENTS

Many thanks to Vanderbilt ARMA lab. Thanks to Vanderbilt discovery grant and Vanderbilt ViSE fellowship to provide funding support. Thanks to Prof. Nabil Simaan in guiding me towards my Ph.D. degree with his profession, knowledge and patience. Thanks to Dr. Karen Joos of supporting me with her extraordinary clinical background. Thanks to my other committee members Prof. Nilanjan Sarkar, Prof. Pietro Valdastri and Prof. Karl Zelik for being able to advise me upon this dissertation. Thanks to all ARMA members especially Jason Pile and ARMA alumni Dr. Andrea Bajo for their generous help in research when I am in need.

ABSTRACT

Retinal surgery requires surgeons to manipulate delicate structures with very high precision while contending with perception and manipulation challenges due to the limited repertoire of tools available to them. Current commercial robotic systems are unable to support tasks of orbital manipulation and intraocular dexterity. In addition, the emerging use of optical coherence tomography (OCT) as a feedback modality for surgeons presents questions regarding the value of such feedback and the ways such information can be used by the robot and the surgeon to improve safety and accuracy of retinal surgery. Current OCT and robotic systems are unable to support real-time intervention control and to provide sectional information of the anatomy (B-mode imaging), which is necessary for surgeon feedback during the operation.

This dissertation presents design, modeling, calibration and control of robotic systems for increasing the safety of micro-surgery on constrained organs such as the eye. To address the limitations listed above a dual-arm robotic system is improved and customized to meet the needs of safe orbital manipulation. A new modeling approach for constrained telemanipulation of such robots is also developed and demonstrated experimentally. New approaches for calibration of custom B-mode OCT probes and their integration for control feedback and assistive telemanipulation are investigated. Finally, calibration of dual arm robotic systems for manipulation of partially constrained organs is presented with the aim of facilitating eventual clinical deployment.

This work provides the theoretical and technological basis for the design and integration of future OCT-guided robotic systems. Results of investigation of the utility of OCT feedback with and without robotic assistance point to the value of a combined solution integrating both technologies. Evaluation of telemanipulation algorithms suggests that the combined use of vision and OCT feedback for assistive telemanipulation control can improve task execution accuracy and safety. The evaluation of the new calibration algorithms

for such systems demonstrate the robustness and efficacy of our approaches compared to previous works.

TABLE OF CONTENTS

LIST OF TABLES

LIST OF FIGURES

Chapter 1

Introduction

1.1 Background on Ophthalmic Surgery

Retina interventions require recision, hand stability and multi-tool intraocular manipulation. A traditional ophthalmic surgery setup is shown in Fig.1.1(a) and Fig.1.1(b). A main surgeon and two assistant surgeons are needed to coordinate with each other to perform the whole surgical procedure. The main surgeon sits superior to the patients head and performs most of the surgical tasks including manipulation of the surgical tools and the light source. One assistant surgeon sits beside the patients head to provide irrigation and removal of fluids and to adjust the placement of the external visualization lenses. The assistant surgeon sits on the other side of the patient for tool delivery to the main surgeon. The surgical tools include picks, micro tweezers, vitrectomy cutters, micro injection tool and other tools dependent on the requirements of the procedure. The main surgeon supports his/her hands on a frame around the patient's head, holds two surgical instruments (usually one light source and one operational tool), and operates using a microscope while visualizing the retina through a dilated iris.

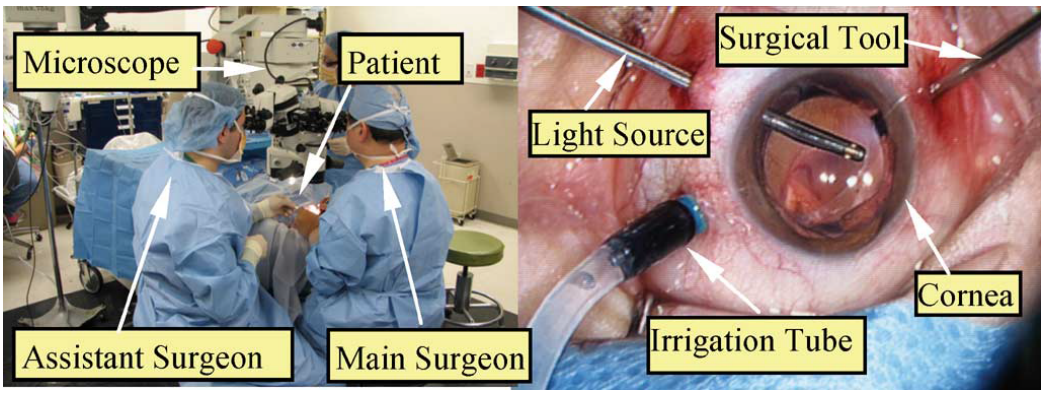

Figure 1.1: a. Surgical setup; b. Microscope top view. Picture from [1]

This traditional setup has several limitations. The human eye is an extremely sensitive anatomy where high precision procedure is needed and manual intervention lacks hand stability and sub-micron precision. Current surgical tools provide limited sensory feedback with only the stereo type microscope and the feeling from surgical tool to the hand. Current surgical setup is ergonomically uncomfortable and could result in neck pain and lower back pain due to the surgeon's fatigue [6, 7]. Current imaging techniques through the surgical microscope provide limited depth perception. The main surgeon has to manipulate multiple tools and the eyeball at the same time while holding his/her hand steady. Due to the required remote center of motion (RCM) motion, the tool movement under microscope top view is inverted from the surgeon's hand movement. The following section will review retinal interventions that could benefit from robotic intervention.

1.2 Clinical Condition Motivating This Research

Retinal vascular disease is a leading cause of blindness. Retinal microsurgical interventions treat various retinal diseases, such as branch retinal vein occlusion (BRVO), central retinal vein occlusion (CRVO), macular hole, epiretinal membrane (ERM), retinal detachment and diabetic retinopathy. In this section, reviews on description of these retina diseases, severeness of the condition and traditional surgical interventions for treatment are summarized. These reviews guide the clinical motivation of this dissertation research.

Branch retinal vein occlusion (BRVO) is the second most common retinal vascular disorder following diabetic retinopathy. Population-based studies reflect an overall adult prevalence of 4.42 per 1000 people or 13.9 million people worldwide with BRVO [8] and occurrence increases with age. BRVO can cause a decrease in vision due to ischemia or edema of the macula, and/or vitreous hemorrhage. More than half of patients with BRVO develop visual acuity worse than 20/40. BRVO typically occurs at arteriovenous crossing sites with the artery positioned anterior to the vein producing compression [9]. The Branch Vein Occlusion Study [10] and the Standard Care versus Corticosteroid for Retinal Vein

Occlusion Study [11] demonstrated that grid laser is helpful for resolving macular edema. Alternatives have been sought because retinal hemorrhages interfere with laser treatment and laser induced scarring can decrease vision. Medical therapies include intravitreal injection of corticosteroids or vascular endothelial growth factor (VEGF) inhibitors to treat the retinal edema rather than the underlying blood flow obstruction. However, a significant proportion of patients are unresponsive to medical therapy and retain macular edema and poor vision. In [12], an update of literature review summarizes the treatment alternatives. The first report of surgical decompression as a successful potential treatment for BRVO with a vitrectomy and technically challenging separation of the common adventitial sheath of the crossing artery and vein (sheathotomy) was published in 1988 by Osterloh and Charles [13]. Multiple reports have suggested that vitrectomy with sheathotomy may improve vision in patients with recalcitrant macular edema unresponsive to laser therapy and/or medical therapy [14, 15, 16, 17, 18, 19, 20, 21, 22]. One study reported no difference between sheathotomy versus intravitreal triamcinolone acetonide injection, but they did not limit their subjects to medically recalcitrant edema [23]. Because a one-year course of anti-VEGF ranibizumab may exceed $23,000, [24] the cost of a highly successful surgical intervention could be cost-effective in BRVO treatment. Precise robotic control would likely reduce iatrogenic surgical complications of vitreous hemorrhage [14] or localized retinal detachment [25] at the arteriovenous sheathotomy site. Alternatively, micro-vascular cannulation has been proposed by several groups to restore blood flow and prevent recurrent occlusion [26, 27, 28, 29]. We hypothesize that a better solution for recalcitrant vascular occlusions would be microsurgical interventions that allow accurate placement of micro-stents. To successfully apply these micro-vascular techniques, the stenting procedures need to be adapted for micro-vessels of the retina. The accurate and reproducible deployment of stents with diameters below the 200 microns range require a high degree of intra-ocular dexterity.

Diabetic retinopathy is the most common cause of vision loss for people with dia-

betes. As a consequence of diabetic retinopathy, fluid will build up in macula that results in diabetic macular edema (DME) [30]. Diabetic retinopathy usually progress in four stages: mild nonproliferative retinopathy, moderate nonproliferative retinopathy, severe nonproliferative retinopathy and proliferative diabetic retinopathy (PDR) [30]. For DME, several treatment [30, 31, 32] were proposed including injecting anti-VEGF agents [33, 34, 35, 36, 37, 38, 39, 40], laser photocoagulation [41, 42, 43, 44, 45], corticosteroids [46, 47, 48, 49] and the combination of different therapies [50, 51, 52]. The PDR is usually treated with scatter laser surgery (sometimes called panretinal laser surgery or panretinal photocoagulation) [53, 54, 55, 56, 57, 58, 59]. More recent studies also focus on effect of anti-VEGF not only in DME but also in PDR [60].

For BRVO and diabetic disease listed above, they all involve surgical interventions such as vitrectomy, sheathotomy, micro-injection and laser therapy. These surgical interventions require surgeon to manipulate on small objects such as blood vessel. The blood vessels on human retina are usually $\leqslant 100\mu m$ in diameter. This requires the surgical procedure to be carried out under extreme precision and also maintain certain intraocular dexterity. Hence robotic assistance is needed to fulfill these requirements.

A macular hole is a small break in the macula, located in the center of the retina. A macular hole may markedly reduce central visual acuity. Macular holes are related to aging and usually occur in people over age 60 [61]. A population-based retrospective chart review was performed in Minnesota and reported the prevalence of macular hole to be around 0.1 to 0.8 in adults aged ¿40 years and an age- and sex-adjusted incidence in 7.8 persons and 8.69 eyes per 100,000 population per year [62]. In subjects with myopia, the prevalence of macular hole may reach 6% [63]. Since a surgical approach for macular holes was described in 1991, this previously inoperable blinding condition has become an efficacious vitreoretinal surgical procedure, with a success rate over 90% [64, 65, 66, 67, 68, 69, 70]. Several authors have found that peeling of the internal limiting membrane (ILM) improves anatomic closure rate and visual outcome in macular hole surgery, especially in cases with

a poorer prognosis [71, 72, 73, 74, 75, 76, 77, 78, 79]. As a result of treatment, in the case of macular hole, the hole diamter should be $\leqslant 400\mu m$, traction has to be present, and ERM should be absent. However, peeling of the ILM without damaging other retinal layers is exceptionally challenging; the ILM is only 1.8 to 4.8 microns thick in humans [80]. Chromovitrectomy dyes are employed to improve visualization of the ILM, but indocyanine green dye is toxic to the retina pigment epithelium [81, 82, 83] and others are less effective for visualization [84].

Wrinkled tissue known as epiretinal membranes (ERM) (or macular pucker) can also develop overlaying the retina to distort vision. Idiopathic ERM can cause reduced vision and metamorphopsia by several mechanisms, including tissue covering and/or distorting the macula; low traction retinal detachment of the posterior pole; vascular leakage with intraretinal oedema; and obstruction of axoplasmic flow [85, 86]. It typically affects the central vision while peripheral vision remains unaffected. The thickness of ERM averages about $61 \pm 28\mu m$ [87]. Not all ERM require treatment. However rarely, when vision deteriorates to the point where it affects daily routine activities, surgery may be recommended [88]. Vitreous surgery is often used to remove the epiretinal tissues [85, 86, 89, 90, 91, 92]. Several group of researchers [93, 94] also studied about the difference between "single peeling" (in which only the ERM peeled) and "double peeling" (in which the ILM is also stained and peeled). The "double peeling" has significant acuity outcomes in the long term.

Proliferative vitreoretinopathy (PVR) is the clinical condition previously known variously as massive vitreous retraction, massive preretinal retraction, or massive periretinal proliferation [95]. It usually follows rhegmatogenous retinal detachment (RRD) secondary to the occurrence and proliferation of ectopic cell sheets in the vitreous and/or periretinal area [96]. It occurs in 5-10% of all RRD [97] and is implicated in redetachment after surgery in 75% of cases[98, 97, 96]. PVR is the most common cause of failure following retinal reattachment surgery and often can lead to blindness [99]. For moderate management of PVR, buckling and encircling procedures may achieve a sustained closure of all

retinal breaks and the release of circumferential traction caused by alterations in the vitreous base [100, 101, 102]. For severe PVR, surgery is required in eyes with PVR-associated retinal detachments to peel away the thin yet tenacious membranes that exert traction on the retina causing persistent retinal detachment [103]. The aims of surgery are to relieve the tractional forces, to close the retinal break while restoring the normal anatomy and the ciliary body function[96].

For all the surgical treatment that involve vitrectomy and membrane peeling, sub-micron level accuracy is needed. The membrane thickness vary between 10 $100\mu m$ (ILM and ERM). Hence novel dual-arm robotic assistance that could dampen human tremor and increased precision would represent a major advance for these surgery. Also, membrane peeling procedure needs intraocular dexterity to dynamically change the approaching angle of engaging the surgical grasp with membrane edge and should be capable of following dexterous path to lift and remove membranes.

1.3 Related Work

The following review of related works will highlight the need for new approaches for constrained dual-arm manipulation of hollow organs, image guided intervention using OCT and accompanying robot design and control algorithms. Each review will start with the goal of the related research, followed by brief summary of other groups' work, and then move onto limitations of these works and the contribution of this dissertation.

1.3.1 Review of Robot-Assisted Ophthalmic Surgery

Robot-assisted ophthalmic surgery has been shown to enhance surgical accuracy while overcoming physiological tremor. In the past two decades, robotic retinal surgery has been steadily advancing surgeons capabilities to carry out increasingly complex tasks in the laboratory setting. Initial telemanipulation control and feature extraction improved accuracy in sub-retinal injections [104] (Fig. 1.2(a)). An alternative wire-actuated telemanipulation

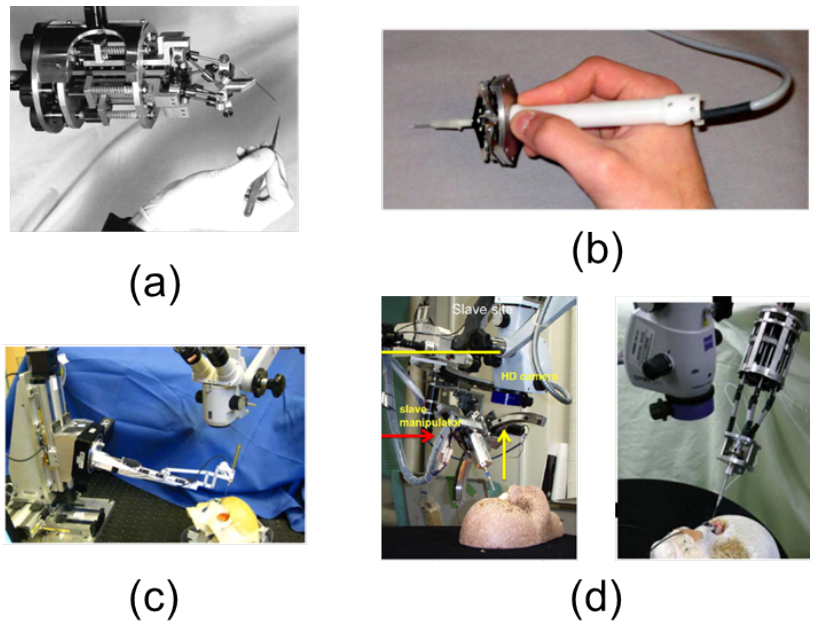

Figure 1.2: Related work on robot-assisted ophthalmic surgery

robotic slave was designed by Das, *et al.*, for assistance in experimental ophthalmic surgery [105]. Instead of using telemanipulated robots, Taylor, *et al.*, used the concept of hands-on or cooperative manipulation of a steady-hand robot for micro-manipulation [106] (Fig. 1.2(c)). Riviere, *et al.* also reported instrument tremor reduction with robotic assistance [107] (Fig. 1.2(b)). Mitsuishi *et al.* [108, 26] developed a parallel robot for vitreoretinal surgery (Fig. 1.2(d)). With an endoscope, Bettini, *et al.*, demonstrated the utility of robotic vision-guided control laws that enforced motion constraints and/or provided corrective assistive motions to guide users in micromanipulation tasks [109]. An extension of this approach recently was demonstrated in a hand-held tremor-cancelling robot [110]. Ueta, *et al.*,[26] built a prototype robot and demonstrated feasibility for pointing, retinal vessel sheathotomy, and retinal microvascular injection in cadaver porcine eyes. A dual-arm robotic system capable of both orbital and intraocular manipulation was proposed by Wei, *et al.* [4]. This system was mathematically modeled for four modes including: movement of the eye using external robotic tools; movement of intraocular robotic instruments within a stabilized eye; maintenance of intraocular instrument positions relative to the retina

during controlled eye movements; and simultaneous movements of the eye and intraocular instruments. This group demonstrated the feasibility of micro-stent deployment in a chick chorioallantoic membrane vascular model [111], and subsequently demonstrated an algorithm for force sensing and telemanipulation assistance for microvascular stent deployment [5]. Improved vessel cannulation with robotic assistance was also found by Becker, *et al.* [112]. Noda, *et al.* [113] reported telerobotic assistance improved lateral movement accuracy, tool stability, and depth perception accuracy in a phantom eye model. Improvements have been made in tremor cancellation, precision pointing, force feedback, and assistive virtual fixtures.

Virtual fixtures assistive control laws have been used by several groups [114, 115] for vision-guided micro-manipulation and tremor filtering. Previous robotics research demonstrated key technologies for increasing safety during ophthalmic surgery by using virtual fixtures [116], reducing tremor [107, 106], and providing force measurements [117]. These works used either hand-held devices (e.g. Micron [107]) or stable cooperative manipulation platforms such as the Steady-Hand robot [106]. While these works focused on stabilizing/-manipulating straight needles inside the eye, in [1] and [4] our group has put forth a concept of a dual-arm system capable of providing both ocular and intra-ocular dexterous manipulation. We have developed the mathematical framework for coordinated manipulation of hollow organs such as the eye but have not implemented these concepts experimentally. In [118] we proposed and demonstrated feasibility of stent deployment in an open setup without consideration of remote center of motion constraints due to tool manipulation through the scleral wall. This work was recently extended in [5] to demonstrate an assistive telemanipulation framework for force sensing and stent deployment.

Despite the progress made, two main fundamental design limitations remain: to date, there are no designs capable of both offering ocular manipulation and stabilization under the microscope while offering intraocular dexterity beyond the limitations of using straight needles and instruments. In addition, with the exception of our own works [111, 119]

there are no existing designs and control algorithms that allow sheathotomy and/or with-/without stent/MVCS deployment. Despite the success of stenting procedures in cardiac vascular applications [120, 121], micro-vascular stenting in ophthalmic retinal surgery remains unexplored due to lack of instruments that address the challenges of this procedure. Micro-vascular stenting requires high precision and intraocular dexterity of surgical tools. A new design with quickly exchangeable tools shall be implemented, which will allow coordinated control of the eye while respecting the kinematic constraints imposed by the incision points in the sclera and providing dexterity to cover all regions of the retina.

1.3.2 Review of *In-vivo* Dexterous Mechanisms in Ophthalmic Surgery

Most of the robotic retinal surgical setups have a straight robotic stem [106, 107]. The disadvantage of the straight tool is lacking intra-ocular dexterity. In retinal surgery, the surgical tool has to obey the sclera incision point constraint thus reducing the controllable DoF inside the eye to four. Moreover, the yaw motion around the tool stem does not help much in most of the surgical interventions, thus leaving the surgeon with only the translational manipulation. Specifically, in retina surgical interventions such as internal limiting membrane (ILM) peeling and vessel cannulation, the tool requires different approaching angles to avoid damaging the retina and to increase the success rate.

Ikuta and Kato [2, 3] designed a hand-held forceps with an active joint and fiberscope to address the lack of dexterity inside the eye, Fig. 1.3(a). Maneuverability and feasibility test was carried out on pig eyes. This design was the first strike towards intra-ocular dexterous tool in ophthalmic surgery and therefore encountered a couple of issues: no tremor cancellation since it is a hand-held tool; high cost in manufacturing the wire actuated active joint; surgeon has to be able to maintain hand stability while adjusting the approaching angle. Wei and Simaan [1, 4] from our group proposed the idea of 3-DoF Intra-ocular Dexterous Robot (IODR) that consists of a pre-shaped active cannula, a pushing stent and a guide wire, shown in Fig. 1.3(b). The kinematic framework for the hybrid robotic system

when incorporated with the parallel robot was discussed in [4]. However, the prototype of IODR stood alone to be tested and a compact IODR remained to be developed and added to a parallel robot. Furthermore, the proposed hybrid robotic control algorithm needs to be implemented and experiments on both phantom retina model and animal eyes should be carried out to compare this system to straight robotic tools. This work aims to fulfill these needs.

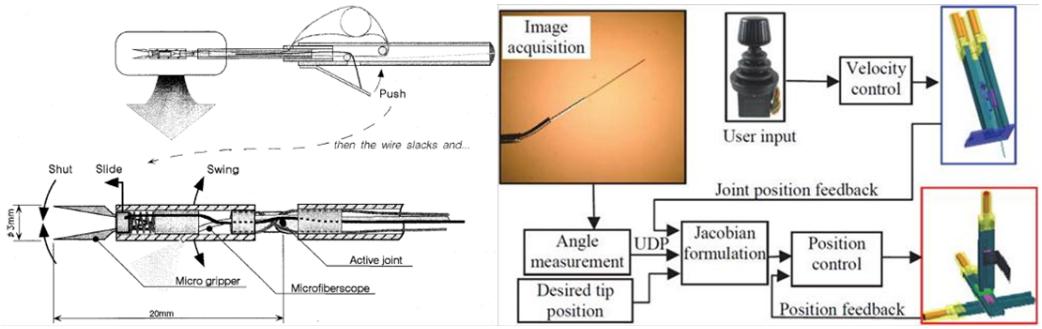

Figure 1.3: a. Ikuta and Kato, hand-held forceps with an active joint [2, 3]; b. Wei and Simaan, IODR [4].

1.3.3 Review of Robot Calibration

The robot calibration is the process of enhancing the accuracy of a robot manipulator through modification of the robot model used by the control software. In multi-arm manipulation (Fig. 1.4), robot arms carry different surgical tools to manipulate inside the human anatomy. To achieve the dexterity of the robot manipulator, the robot system is usually very complicated. Mechanical assembly error will come along with high degree of freedom (DoF) mechanisms. Thus, the robot calibration and the robot tool registration are necessary for accurate robotic control. A specific problem encountered in surgical robotics is that most human anatomy has soft tissues and the advantage of robot-assisted surgery is stability and safety. However, the robot is not as ”smart” in adapting itself to different anatomy when doing intra-ocular manipulation, e.g. retinal surgery. Human anatomy like

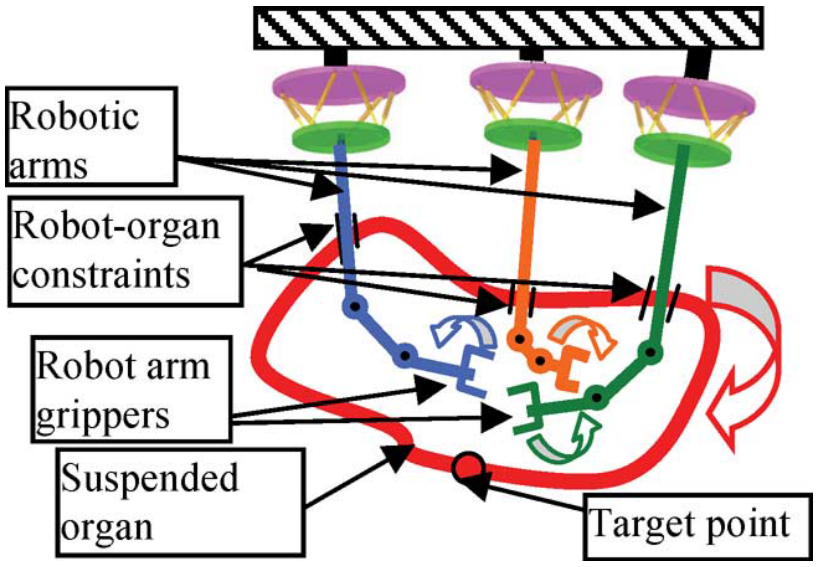

Figure 1.4: Common setup of multi-arm robotic structure in manipulating the hollow suspended organ, [4]

eyeball varies in size and is extremely vulnerable, thus there is a need for online calibration of the dimension of hollow suspended organs.

One calibration process will encompass four distinct actions: determination of a mathematical model that represents the robot geometry and its motion (kinematic modeling); measurement of the position and orientation of the robot end-effector in world coordinates (pose measurement); identification of the relationship between joint angles and end-point positions (kinematic identification); modification of control commands to allow a successful completion of a programmed task (kinematic compensation).

Robotic calibration methods have been steadily developed through the past 30 years. Hayati [122] in 1983 derived an error mapping method for serial robot to relate homogeneous error transformation matrix with measured joint assembly error. Zhuang and Roth [123] extended this work by developing two singularity-free models, called CPC and MCPC. Yang and Chen [124] in 1997 did serially connected modular robot calibration. Kikuchi and Arai [125] proposed plug and produce concept for realizing easy reconfiguration when a new device is installed.

Since early 1990's, several groups have also made significant progress on parallel robot

calibration. Hayward's group [126] proposed a method for autonomous kinematic calibration of a 3-DOF redundant parallel robot and also introduced the observability indices for choosing optimal robot calibration configurations. Zhuang [127] in 1997 worked out self-Calibration of Parallel Mechanisms and the calibration of the Stewart platform was done by installing a proper number of redundant sensors in specific locations and creating a suitable measurement residual. Khalil [128] did simulation on 6 DOF Stewart Gough platform self calibration without a measuring sensor for robot configuration, instead they put mechanical locks on the universal/spherical joints to reduce the robotic DOF and form calibration equation with known joint angles.

Although multiple groups have done good works on self calibration of hybrid robotic systems, none of them addressed issues of calibrating the vulnerable hollow organs while using robotic hands to manipulate them. Especially in ophthalmic surgery, surgeons usually make an initial guess for the eyeball geometry and position of the sclera incision points. In the following dissertation we propose rapid calibration algorithms for the robotic control system to quickly calibrate related parameters made from pre-operative measurements.

1.3.4 Review of OCT Application in Ophthalmic Surgery

Optical coherence tomography (OCT) has become widely used as an important diagnostic and surgical pre-planning tool in ophthalmology. This imaging modality provides valuable depth information of various disease processes within the retina. Perioperative scans, including hand-held or microscope-coupled systems, produce information regarding the extent and location of vitreomacular traction [129, 130, 131], macular holes [129, 130, 132], and visually significant epiretinal membranes including characterization of membrane edges [129, 130, 133, 134]. Improved real-time intraoperative location of these edges would improve success rates of complete membrane removal and would reduce the use of potentially toxic dyes to visualize the membranes. Dayani, *et al.* published the first approach to using intraoperative OCT imaging with a hand-held external device to evaluate

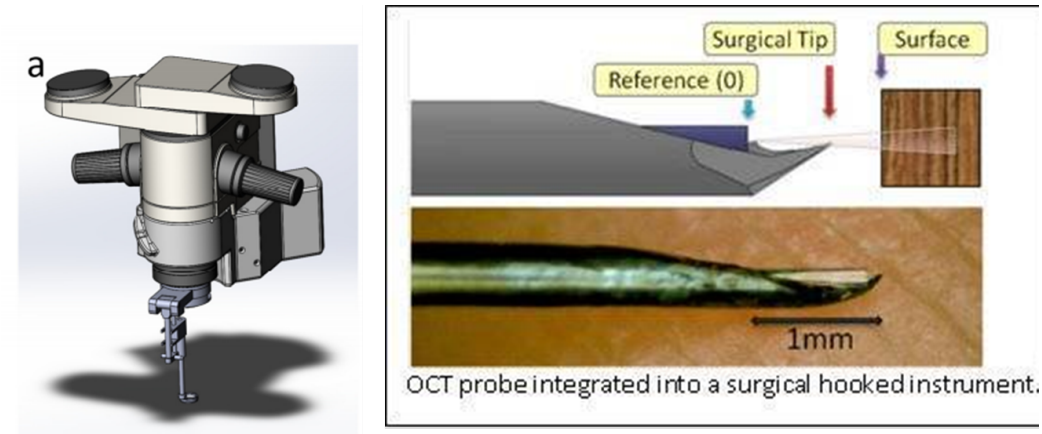

Cleveland Clinic, OCT integrated with microscope

JHU, A-mode OCT probe with a needle tip

Figure 1.5: a. Ehlers from Cleveland clinic, B-mode ex-vivo OCT probe integrated with microscope; b. Kang and Taylor from JHU, A-mode OCT probe with customized needle tip integrated in front.

the retina prior to incision, and to evaluate retinal changes and procedure completeness during planned interruptions of the surgical procedures [129]. Binder, *et al.* performed a foundational study with an external microscope-mounted OCT operating room system to image retinal changes immediately following surgical manipulations [130]. Several other surgical microscope-mounted OCT systems with heads-up displays are being developed to provide real-time visualization in the operating room for anterior segment [135], and for posterior segment [136, 137, 131, 132, 138, 130, 139] surgery. Improvements have been made to permit imaging during a procedure [135, 131, 132, 138, 139]. Three-dimensional surgical systems are also being developed [138, 139, 140]. Artifacts of motion, variable illumination, and tilt affect 3D-OCT images necessitating ongoing post-processing algorithm developments for static clinical 3D-OCT images [141]. Surgical limitations have included the complete blockage of the underlying retinal image by shadowing from standard stainless steel intraocular instruments, as well as problematic tracking of instrument movements within the OCT image, thus reducing useful real-time surgical guidance [137, 142, 143, 144]. A forward-viewing intraocular surgical B-scan OCT probe co-planar with an intraocular in-

strument would provide a mechanism to bypass these issues and directly view the tissue structures in real time. In addition, an intraocular probe would bypass media obstructions including corneal opacities, miosis, and lenticular opacities that degrade an external OCT image. A miniature probe would permit cross-sectional images of epiretinal membranes and their edges thus enabling surgeons to scan the retina to determine if the membrane peeling was satisfactorily completed prior to removing the instruments. Besides imaging macular pathology, an intraocular probe would be able to transmit direct images of peripheral membranes and lesions without the distortions inherent in peripheral images with external OCT systems [145, 146].

OCT is routinely employed in the ophthalmic clinic to evaluate retinal diseases. However, it is not used routinely intraoperatively in vitreoretinal surgery. Small OCT side-scanning probes have been developed to examine tubular tissues (e.g. [147, 148, 149]). Probes as small as 0.36 mm have been developed, but they project views from the side rather than directly in front of the catheter tip [149]. OCT was combined with the operating microscope, but its lateral resolution was 5-times less than with a hand-held OCT probe system during laryngoscopy [150]. A forward-imaging OCT device has been used to image bladders, but its diameter is relatively large, measuring $5.8mm \times 3mm$ [151]. The standard micro electro-mechanical system (MEMS) scanning mirror component of an OCT forward-imaging probe has been reduced to a diameter of 1 mm [152] but just the mirror alone is still larger than the 0.91 mm requirement for an ophthalmic intraocular surgical probe. Others have used various designs (e.g. [153, 154, 155, 156, 157]) but the smallest is 1.65 mm in diameter [156]. To address the size challenge, using the OCT A-scan component alone permits miniaturization of the sensing probe. Iftimia, *et al.* [158] developed an OCT A-scan 250 μm diameter probe to measure one-dimensional information in solid tissues for fine needle biopsy guidance. A bare fiber A-scan probe has also been proposed for intraocular surgery [159, 160]. External movement of the fiber would be required to retrieve 2-D images [159]. Shen, *et al.* proposed new OCT probe designs that overcome

the limitations of these previous works: lack of real-time feedback or lack of B-mode imaging capabilities [161] (sample B-mode OCT images, see Fig. 1.6 from [162]). This work capitalizes on new emerging technologies providing real-time B-mode imaging with an interactive rate of 5 to 10 Hz [161]. It opens up the possibility of using the OCT technology as feedback modality in control and assistive telemanipulation during robot-assisted ophthalmic surgery. It also helps to focus the dissertation towards its stated goals of developing new algorithms for hand-eye calibration and distortion rectification.

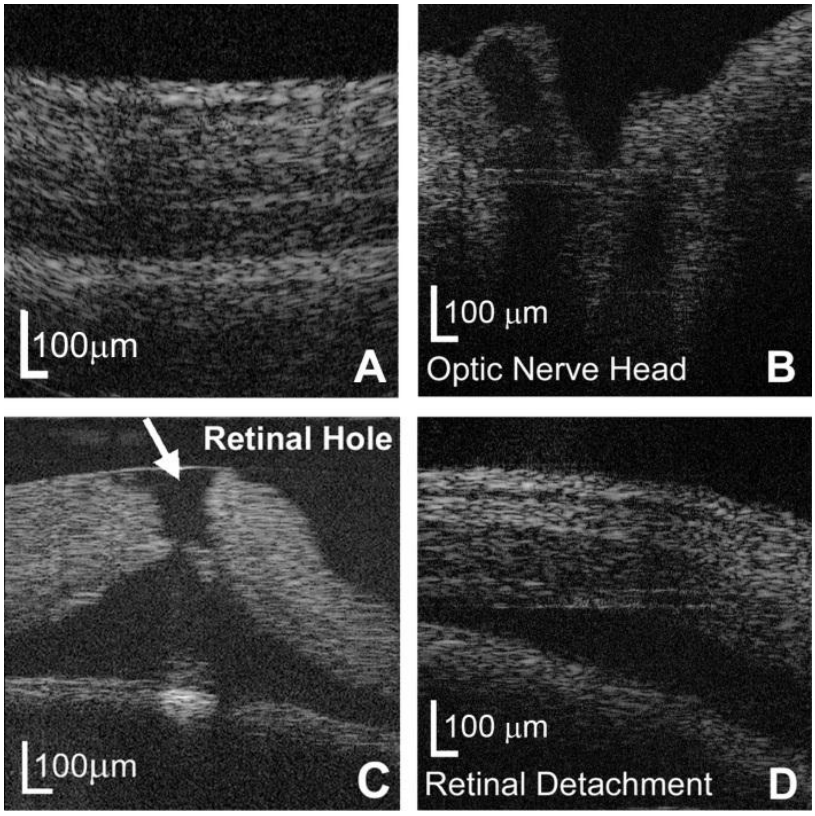

Figure 1.6: The miniature intraocular probe is able to (a) distinguish layers of the retina, (b) image the optic nerve in a porcine eye, (c) image a retinal hole, and (d) visualize a retinal detachment.

1.3.5 Review of OCT Calibration

Several groups have put forward OCT image calibration algorithms. Westphal, *et al.* [163] corrected the nonlinear axial scanning and non-telecentric scan patterns, as well as re-

fraction correction in layered media, proposed a backward transformation approach based on Fermats principle, and validated the distortion correction on the anterior chamber angle of the eye. Xie, *et al.* [164] proposed a general correction method for the image distortion in laser galvanometric scanning system. Podoleanu, *et al.* [165] proposed a different procedure based on the refraction law only and they also considered the case of angular scanning specifically for retina imaging. Ortiz, *et al.* [166] addressed the measurement and correction of fan distortion from obtaining quantitative topographic data from OCT and process with computer simulations to quantify the effect and to evaluate its dependence on the scanning mirror separation and design of the collimating lens, as well as to estimate the optimal axial position of that lens to minimize the fan distortion. The same group [167] developed a method for 3-D optical distortion (refraction) correction on anterior segment OCT images. Tian, *et al.* [168] corrected the distortion caused by refraction by resizing the original axial and transverse resolution, automatically detecting the corneal epithelium and correcting the refraction using Snells law. They also reported to have tested their algorithm on 40 HD-OCT images and provided accurate measurements in about 1 second. Sun, *et al.* [169] developed a prototype neurosurgical hand-held optical coherence tomography (OCT) imaging probe. A mirror was used for calibration to find the artificially induced curvature of a flat surface and the scan angle as it appears in the OCT image, which were then input to custom software and the corrected images are automatically generated. Siedlecki, *et al.* [170] proposed a method to correct optical coherence tomography (OCT) images of posterior surface of the crystalline lens incorporating its gradient index distribution and explored its possibilities for posterior surface shape. In particular, the availability of algorithms to correct for distortions introduced by the scanning architecture of the systems (fan distortion) [171, 163, 165, 164] and for distortions arising from refraction by preceding surfaces (optical distortions) [163, 165, 167] opens the possibility for full OCT based topography of not only the anterior surface of the cornea but also internal surfaces of the ocular components.

These previous works mainly focused on ex-vivo scanning OCT technology which could not particularly be applied directly onto our customized in-vivo B-scan OCT system. Kang, *et al.* [172] presented an axial motion distortion-corrected optical coherence tomography system and a data processing system configured to correct distortion in the images caused by net axial motion by calculating an estimate of the net axial motion using Doppler shift, and then shifting the A-scans according to the estimate. Liu, *et al.* [173] proposed a manually scanned hand-held OCT system that provided real-time scanning speed correction and distortion-free imaging based upon a customized developed in-vivo A-scan OCT probe. Liu, *et al.* [160] presented a new real-time automatic spectral calibration (ASC) method for Fourier domain optical coherence tomography (FD OCT), which incorporated known robot motion to calibrate physical pixel spacing of the A-scan in static or dynamic environments. However, our customized OCT probe automatically produces a real-time B-scan image. The distortion created by this probe is not only a result of the fan distortion or the optical distortion, but also the nonlinear scanning from the mechanical design of the electro-magnetic actuation unit which incorporates the adjustment of the scanning frequency and the mechanical friction. Thus we need to propose a more general calibration method for in-vivo B-mode OCT scanning probes that does not need to calibrate the probes intrinsic design parameters. Thin plate splines (TPS) was used for ultrasound image dewarping [174, 175, 176, 177]. To the best of our knowledge, there have been no prior work dealing with OCT image dewarping using TPS.

1.4 Contribution and Organization of this dissertation

1.4.1 Potential Clinical Impact of this Work

In addition to advancing clinical outcomes, this proposed research is motivated by the limitations of current tools available to ophthalmic surgeons. While other areas of surgery (e.g. orthopedic surgery [178, 179, 180, 181, 182, 183, 184, 185, 186, 187, 188, 189],

urology [190, 191, 192, 193, 194, 195, 196], cardiac surgery [197, 198, 199, 200, 201, 202, 203], laparoscopic abdominal surgery [204, 205, 206, 207, 208, 209, 210, 211, 212, 213, 214, 215, 216, 217], and neurosurgery [218, 219, 220, 221, 222, 223]) have significantly benefited from robotic assistance and in-vivo imaging, ophthalmic surgery has lagged due to technological challenges. The best ophthalmic surgeons are still limited by the lack of distal intraocular dexterity, physiologic human tremor, lack of force-feedback, limited visualization and confined intraocular access. As a result of these limitations ophthalmic surgeons are challenged with the most complicated dexterous bimanual operations on the delicate retina including its vasculature.

This dissertation, although focused on micro-vascular retinal surgery, has the potential to impact other surgical specialties including microsurgical otolaryngological, neurosurgical, and micro-vascular procedures. This research will guide the application of new technology for treating these diseases and may open new avenues for surgical approaches to previously untreatable conditions.

1.4.2 Theoretical and Application Gaps

Theoretical gaps for this dissertation aim to summarize the limitation of related work to our proposed study and to delineate the theoretical contribution introduced in this dissertation.

The first contribution of this dissertation is the modeling framework for rapid calibration and deployment of cooperative systems operating on hollow suspended organs. No other group has developed similar algorithms to help the robot in studying the organ geometry. In robotic retinal surgery, related works have adopted hand-held device [107], cooperative controlled robot [188] and mechanically constrained RCM point [224], while none of these robot structures allows the robot to the study the kinematic constraint due to different eye sizes. Thus, this will increase the danger of tearing the eyeball since the robotic control is based on an estimated anatomical model. We aim to propose an online calibration regime

that could be implemented into any active robotic arms such as [108, 4]. The theoretical gaps in this topic requires these questions to be addressed: (1) How do we define the calibration parameters and measurements? (2) What is the impact of noisy measurements on the calibration accuracy?

The second theoretical contribution is to delineate the appropriate collaborative telemanipulation virtual fixtures for dual-arm retinal surgery. There are several works on telemanipulation for ophthalmic surgery. However, none of the existing works addresses these questions: (1) How to define a virtual fixture on the fly based on in-vivo imaging data? (2) How to define assistive virtual fixture for dual-arm manipulation on a suspended organ. Other works such as [225, 226] addressed virtual fixtures for knot tying where the tools operate in free space. Here we have to design virtual fixtures possibly assisting the user to respect anatomical constraints of the incision points in the eye and also at the same time we have to impose virtual fixtures at the tool tip when interacting with the retina. Essentially, what is unique about our work is that we are dealing with defining virtual fixtures for tools that interact with the anatomy at more than one point (incision point and tool tip). Furthermore, this work needs to define dexterity measures for specific micro-vascular tasks (membrane peeling, sheathotomy, stent deployment) and explore the redundancy of robot stems to help define path planning towards carrying out these tasks.

The third theoretical contribution is that we carry out the first stride towards developing real-time visual servoing technology combining B-mode OCT and robotics. Other groups [227] have used A-mode OCT in guiding robotic ophthalmic surgery. However the idea of B-mode OCT guided control and assistive telemanipulation was first proposed by our group in [228]. Theoretical gaps that come along with this topic include: (1) calibration of the distorted OCT image; (2) OCT and robot integration; (3) 3D visual based assistive telemanipulation architecture. The result of this study will contribute to the society by providing a calibration protocol for any B-mode OCT probe absent of intrinsic parameters, a robotic actuated tool with inline OCT integration and a combined 3D virtual fixture law

for any ophthalmic system setup including OCT and microscope.

Application gaps for this dissertation show the important realistic obstacles when carrying out the theoretical contribution. The human eye ball is a very sensitive anatomy, so the ophthalmic surgery usually needs extreme precision, ideally under 10 microns. Current surgical tools have limited intraocular dexterity and sensory feedback. For instance, a hand-held instrument will have a tool tip movement opposite to surgeon's hand movement and also straight tools have limited accessible region in human retina. Current surgical tools also lack a sense of force applied on the constraints including incision points and retina surface. Current visualization techniques have limited depth perception. Traditionally, surgeons will have the microscope top view and/or an ophthalmic endoscope view. None of these provides a depth imaging of the retina.

1.4.3 Dissertation Goals

The dissertation goals are derived from the theoretical gaps and application needs. The following are the key dissertation goals:

A. Design, construct and control an accurate, rigid and stand alone hybrid robotic system for computer-aided dexterous retinal surgery.

To meet the requirements of micro-vascular surgery, this robotic system should be capable of manipulating and stabilizing the eye under a microscope. Also, quick changeable tools that can be attached to the robot arms should provide dexterity inside the eye (intraocular dexterity). We will design and integrate devices that enable the deployment of micro-stents, micro-vascular cannulation, and ERM/ILM peeling. We hence integrated a dual-arm parallel robot system due to its rigidity and high payload-to-weight ratio, and precision advantages compared to serial robots. Design gaps on this dissertation goal stem from a need for having a well-built and well-calibrated parallel robot, which requires taking into account eliminating possible assembly errors in parallel robot design and also at the same time work out a parallel robot self-calibration algorithm. Also the observability

and optimal choices of robot configuration in self-calibration should also be considered. The control of this hybrid robotic system requires fundamental kinematic modeling of the system, the study of kinematic redundancy resolution and a proposed design of path planning for each individual surgical intervention. The detailed theoretical gap driving this dissertation goal is defined as follows. What mechanical improvement can we do to reduce the number of unknown calibration parameters in parallel robot self-calibration algorithm? What kind of retinal interventions could we use our Intraocular Dexterous Robot (IODR) on?

B. Rapid calibration of hollow partially constrained objects

Retinal micro-vascular surgery needs accurate eye parameters for the hybrid robotic system to drive the robot in 3-D. Traditionally surgeons will make an initial guess of eye parameters including eye ball position, eye ball radius, and 2 insertion points position before retina surgery. Mainly these guesses will base on experience and some pre-operative measurements. A rapid calibration method is required to be able to offer the robot accurate calibrated anatomy parameters. An anatomy like the eye is usually flexible, so this calibration should be done intra-operatively. The detailed theoretical gap on this dissertation goal is defined as follows. What kind of applicable measurement could we use in this calibration problem? How much does the noise influence on the calibration convergence? What influence does the flexibility of the eyeball have on our calibration algorithm?

C. OCT calibration, OCT-robot integration and evaluation

To be able to use the B-mode OCT technology in guiding the robotic motion, we need to calibrate the customized OCT probe to overcome distortion and achieve accurate resolution. A calibrated OCT probe will also benefit retina dimension measurement and allow the robot to improve control accuracy and robustness. Inherently, for the real-time OCT stream, there is a need of a rapid image segmentation algorithm running at the same frequency of the OCT frame acquisition speed. In dual arm robotic setup (Fig. 1.7), two robotic arms will be holding the OCT probe and the tool (e.g. ophthalmic gripper, IODR,

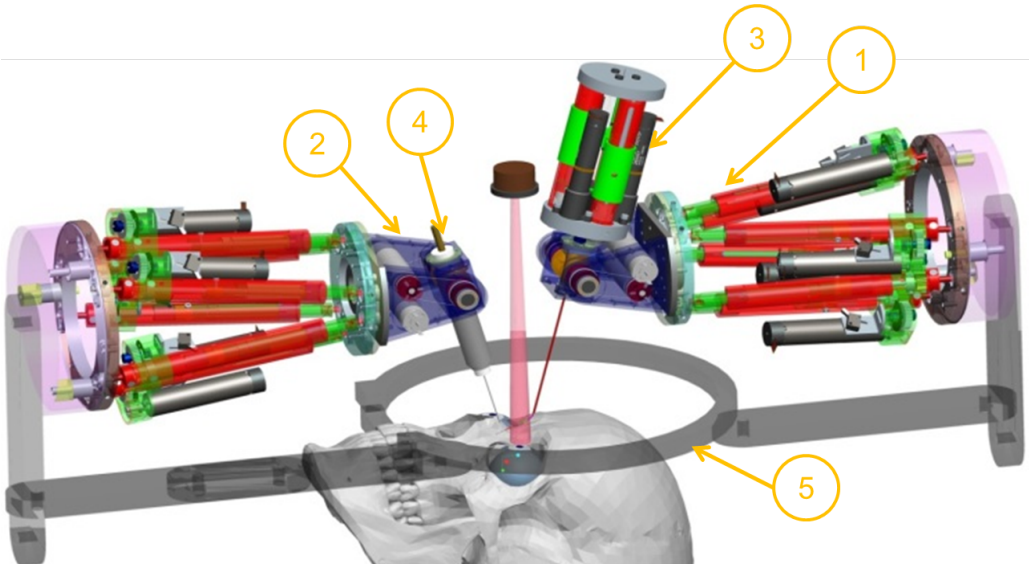

Figure 1.7: Dual arm OCT-guided robotic setup with one robot arm holding the tool and the other robot arm holding the OCT probe: ① Stewart-gough platform; ② Differential wrist; ③ IODR; ④ B-mode OCT probe; ⑤ Base frame.

and etc). However the ophthalmic surgery usually requires multiple tools, so integrating the ophthalmic tool inline with the OCT probe could improve efficiency.

Also, case studies for evaluating the contribution of robotic assistance with OCT guidance could statistically evaluate the influence of using this combined technology. The detailed theoretical gap on this dissertation goal is defined as follows. What image segmentation algorithm should we use for the noise gray-scale B-mode OCT images? How do we calibrate the OCT probe without known the intrinsic parameters of the probe? How do we implement the tool and the OCT together and actuate the tool? What kind of surgical interventions could serve as good representative for evaluation of OCT guidance and robotic assistance?

D. Real-time OCT visual servoing and assistive telemanipulation

A real-time OCT visual servoing will allow surgeons to have a 3D visualization of the retina region and also provides the robot control algorithm a virtual fixture to safely direct the robot end-effector. To address this issue, we first design and integrate B-mode Optical Coherence Tomography (OCT) imaging tools that allow measurement of distance from the

retina and provide cross-sectional images of the retina. And then we design telemanipulation algorithms that use information from OCT images to safeguard against inadvertent trauma and guide surgeons in deployment of micro-stents and retinal interventions. The detailed theoretical gap on this dissertation goal is defined as follows. How do we address the requirement of accuracy and responsiveness in the visual servoing algorithm? How do we improve the sampling rate of the real-time OCT image capturing? How do we combine the 2-D microscope information with the OCT depth information to form a 3-D virtual fixture?

1.4.4 Dissertation Outline

Chapter 2 summarizes the previous work done by former ARMA lab member Wei in [1, 4] and presents new kinematic framework involved in the dissertation. A single arm constrained ocular and intra-ocular telemanipulation architecture is presented in the chapter and also in [228]. With a differential wrist (currently under development) that provides roll and yaw motion on robot stem, a new single-arm 11-DoF robotic control algorithm (6 DoF on parallel robot, 2 DoF on differential wrist and 3 DoF on IODR) needs to be carried out. This redundant robotic system could be mainly used to perform surgical interventions that require intraocular dexterity such as ILM membrane peeling. An application of this robotic system on preliminary experiments in middle ear surgery is also presented.

Chapter 3 discusses the integration of the dual-arm OCT guided robot system. It starts with the mechanical modification we implemented upon the design of the customized Stewart-Gough parallel robot to improve accuracy and reduce unknown calibration parameters. The design of the differential wrist and the IODR is also presented in this chapter. Then it moves on to briefly introduce the intraocular B-mode OCT probe developed by our collaborating group. The feasible tilting angle towards the scanning object plane and work space inside the eye is explored with the customized OCT probe. A combined forward-imaging B-scan OCT probe and forceps design is carried out to put a gripper in line with

the scanning beam and the technical performance is provided. An OCT image segmentation algorithm involving speckle filtering, active contour, edge detection is explored. Then we present the OCT and robot integration and introduce the control algorithm for dual rate OCT visual servoing. An evaluation experiment to test visual servoing precision and latency is presented. The chapter ends with the supporting electronics design for the overall system.

Chapter 4 first presents a self calibration algorithm for the proposed Stewart-Gough parallel robot. Then the chapter moves on to rapid hollow organ calibration including RCM point calibration and rapid organ calibration. The calibration is analyzed with simulation and noise analysis. An experimental setup is also proposed for future test. OCT image calibration uses thin plate spline method with a copper grid as the calibration pattern.

Chapter 5 presents our pilot data about the influence of OCT guidance and robot assistance on traditional manual retina interventions. This work has been presented in [229]. In this study, we construct comparison groups among manual intervention, robot-assisted intervention, OCT-guided manual intervention and OCT-guided robot-assisted intervention on two surgical tasks: retina approaching and phantom membrane peeling. Quantitative data analysis proved that even without any virtual fixture law, the combination of OCT feedback and robot assistance has already dominated any other comparison groups.

Chapter 6 discusses the telemanipulation architecture, microscope based 2D and OCT combined 3D virtual fixtures. A dedicated robotics telemanipulator is designed for initial study in open environment and video stream from both microscope and OCT is segmented and fed back to control loop in real-time. The virtual fixture law is used to implement an assistive telemanipulation that is demonstrated in several experiments. Tracking error is reported on both microscope based and OCT guided virtual fixture. A semi-automated micro cannulation is performed using the telemanipulator under 3D virtual fixture.

Chapter 7 summarizes all proposed work by chapters, draws conclusion on how this work overcomes the theoretical and application gaps. There are also discussions on future

work that could stem and benefit from the framework presented in this dissertation.

Chapter 2

Kinematic Modeling Framework for Constrained Manipulation

In this chapter, we describe the mathematical background for our custom-built hybrid robotic system (see the right arm in Fig. 1.7). The kinematic modeling is the fundamental framework for path planning in different tasks. It not only guides the system integration in Chapter 3, but also leads to control/telemanipulation framework in Chapter 3 and 6. Thus experimental evaluations carried out in Chapter 5 and 6 are selecting different control modes developed in this chapter. The chapter starts with summarizing the previous work on this robotic system and distinguishing this research by describing the main differences. Then this chapter will focus on developing a kinematic framework for task priority redundancy resolution.

2.1 Prior Work

Wei and et al. [1, 4] presented a unified mathematical framework for modeling and evaluating the kinematic performance measures of multiple robotic arms that manipulate and operate within a hollow suspended organs. This framework was applied to the novel two-armed hybrid robotic system that has been proposed in [1, 4]. Each robotic arm is composed from a 2-DoF IODR (Intraocular Dexterity Robot in Fig. 2.1) and a 6-DoF parallel robot. In [1], a deployable design of an IODR was not achieved and this proposal will present a new design. This design will allow 5 DoF for the surgical tools inside the eye, as compared to 4-DoF tools currently used. The 2-DoF IODR provides intraocular dexterity while the parallel robot provides global precise positioning of the eye and the surgical tool inside the eye. The repertoire of manipulation tasks in ophthalmic surgical procedures was segmented into four cases of intraocular and orbital manipulations as shown in Fig.2.2. The

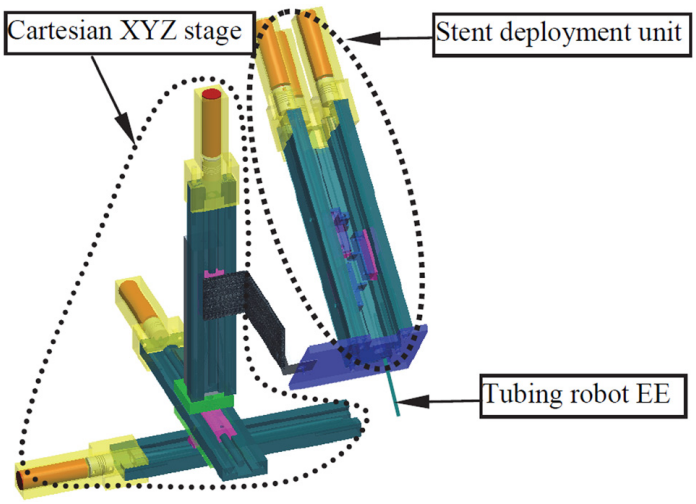

Figure 2.1: CAD model of the IODR with XYZ robot and Vermex slides. Figure reproduced from [5]

four different cases are shown in Fig. 2.2 and are described as following:

1. Case 1: Intraocular operation with eye stabilization. This case quantifies the ability of the robotic system to perform a specified surgical task inside the eye (Fig. 2.2(a)).

2. Case 2: Eye manipulation with constrained intraocular motions. This case evaluates orbital dexterity, a measure of how well the robotic arms can rotate the eye, while respecting kinematic constraints at the incision points and maintaining zero velocity of the forceps relative to the retina (Fig. 2.2(b)).

3. Case 3: Eye manipulation with unconstrained intraocular motion. This case evaluates the orbital dexterity without constraint of the forceps relative to the retina (Fig. 2.2(c)).

4. Case 4: Simultaneous eye manipulation and intraocular operation. This case measures the kinematic dexterity of simultaneous intraocular operation and orbital manipulation as the robot rotates the eye and operates inside it (Fig. 2.2(d)).

The kinematic nomenclature is shown in Fig. 2.2(e). However, the work presented only the simulation results of the proposed manipulation cases. This thesis will be utilizing

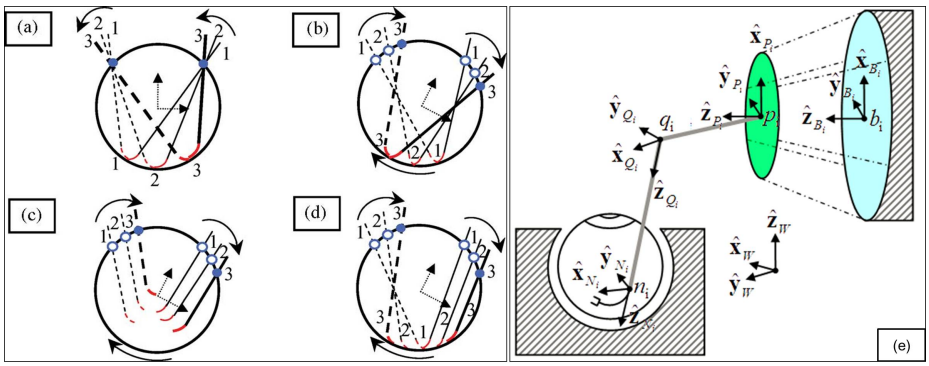

Figure 2.2: Kinematic demonstration of the four manipulation cases. Solid lines denote the first arm, while the dotted lines denote the second arm; the thick lines and solid circles denote the final position of the arms and the entry ports. Figure reproduced from [4]

the kinematic modeling of the previous work while diverging at several aspects according to the specific applications. The main purpose of this thesis will be focusing on robotic control and telemanipulation of the whole 22 DoF hybrid robotic system. Furthermore, the integration of the robotic control algorithm will be implemented in Chapter 3 instead of only having the simulation analysis. The main differences of this dissertation in kinematic framework derivation includes:

1. A 3-DoF IODR will be redesigned and modeled for applications such as retina vessel cannulation and internal limiting membrane (ILM) peeling.

2. Kinematic framework for a single-arm robotic system will be developed from the proposed Case 1 in [4]. However two more DoF will be added between the IODR and the parallel robot. The newly added robot will serve as a 2 DoF rotational actuator which we call Differential Wrist. The design of this actuator will be discussed in Chapter 3.

3. The kinematic modeling and algorithm for Rapid Hollow Organ Calibration will be proposed in Chapter 4 to study an important research topic omitted from the previous work in [4]. The main reason for this study is to address issues in the assumption made in [4] that the robot knows the kinematic and geometric parameters of the

unknown hollow organ.

2.2 Constrained Kinematics for a Single-arm Robot with a Rigid Tool

In [228], we presented a kinematic framework for a single-arm system with a rigid gripper on the parallel robot moving platform. This kinematic modeling was carried out in order to test the ability of the robot in performing intraocular and ocular manipulation without intraocular dexterity. This simplified kinematic modeling is also the fundamental for our real-time robotic control, telemanipulation, and future modeling of more complicated intraocular dexterous robots.

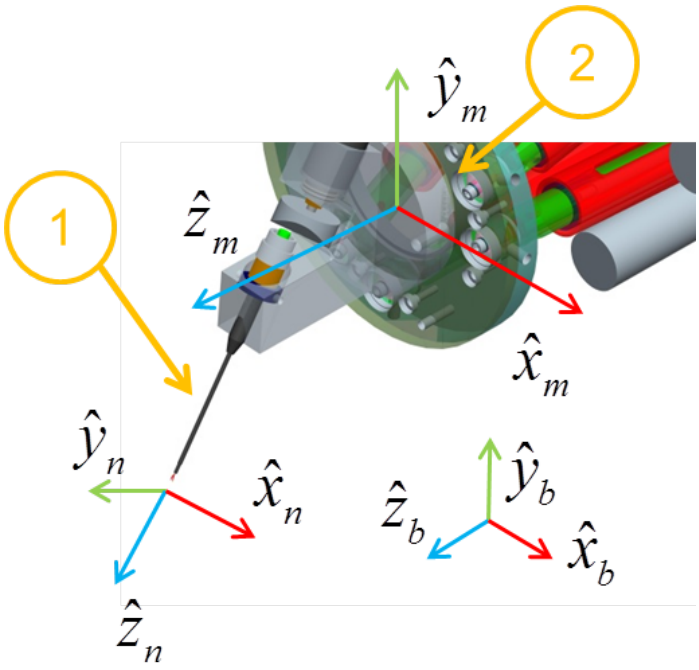

Figure 2.3: Single-arm Robot with a Rigid Tool: ① Custom-made cam driven gripper; ② Parallel robot moving platform

2.2.1 Kinematic Nomenclature

Figure 2.4 depicts the eyeball and a single-arm robotic system. We define the following coordinate systems to derive the system kinematics. The world coordinate system $\{w\}$ is

at an arbitrarily predetermined point with respect to the patient's anatomy. The Stewart-Gough base coordinate system $\{b\}$ of the i^{th} robot is at the center of the base platform of the parallel robot. Without loss of generality, we assume that this frame is aligned with the robot base frame $\{b\}$. The organ coordinate system $\{o\}$ is at the center of eyeball. The moving platform coordinate system of the parallel robot $\{m\}$ is located at the center of the moving platform. This frame is parallel to $\{b\}$ when the parallel robot legs are at a predetermined equal length defining its home configuration. The dimension of the robot arm $\overline{mdn}$ varies for different tool sets. We assume that the origin of frame $\{d\}$ lies at the quick-change interface through which the stent deployment robot or other tools are deployed. This frame is defined by rotating by angle θ about the $\hat{\mathbf{x}}_m$ axis. The end-effector frame $\{n\}$ is placed a the tip of the robot stem and it is parallel to $\{d\}$. For brevity of presentation, we will treat point $\mathbf{n}$ as the end effector of the robot, thus not explicitly modeling the kinematics of the stenting robot, which was presented in [5]. We also define $\mathbf{p}$ as the sclera incision point on the eyeball and $\mathbf{p}'$ as its corresponding, instantaneously copunctal, point on the robot stem $\overline{dn}$. Henceforth, unless otherwise specified, all vectors are defined in world coordinate system $\{w\}$. Also, we will use throughout this paper subscript s and m to designate entities of the slave robot and the master interface, respectively.

2.2.2 Kinematic Modeling for Constrained Intraocular Telemanipulation

This telemanipulation mode allows the surgeon to command the robot's gripper inside the eyeball while keeping the eyeball fixed. This is achieved by transforming the commanded end effector twist (obtained from the master movement) into a kinematically compatible desired end-effector twist.

Let $\mathbf{t}_{n_m} \in \mathbf{R}^{[6\times1]}$ and $\mathbf{t}_{n_s} \in \mathbf{R}^{[6\times1]}$ be the unconstrained master command twist and the constrained end effector twist of the slave robot. The unconstrained master twist is given

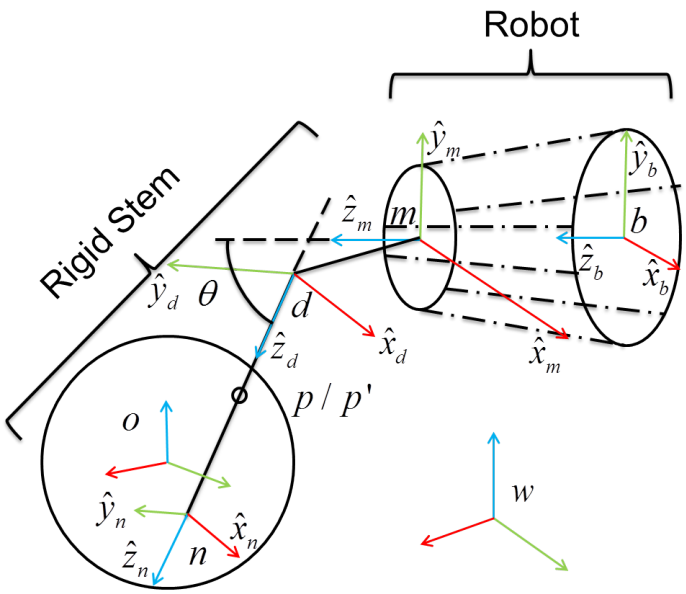

Figure 2.4: Kinematic nomenclature of on robot arm with an eyeball

by the linear velocity $\mathbf{v_{n_m}}$ and angular velocity $\boldsymbol{\omega}_{n_m}$:

$$\mathbf{t}_{n_m} = [\mathbf{v}_{n_m}{}^T, \boldsymbol{\omega}_{n_m}{}^T]^T \tag{2.1}$$

Similarly, we define the telemanipulation slave twist $\mathbf{t}_{n_s} = [\mathbf{v}_{n_s}{}^T, \boldsymbol{\omega}_{n_s}{}^T]^T$. We assume that the known parameters are the organ geometry, the robot configuration and the master end-effector commanded twist $\mathbf{t}_{n_m}$. The kinematic constraint due to the eye incision is expressed by requiring that the velocity projections of point $\mathbf{p}'$ and point $\mathbf{p}$ along the plane perpendicular to the robot stem are equal. Since during this operation mode the eye is stationary, $\mathbf{v}_{p_s} = \mathbf{0}$. This results in:

$$(\mathbf{I} - \hat{\mathbf{z}}_n^T \hat{\mathbf{z}}_n)\mathbf{v}_{p'_s} = (\mathbf{I} - \hat{\mathbf{z}}_n^T \hat{\mathbf{z}}_n)\mathbf{v}_{p_s} = \mathbf{0} \tag{2.2}$$

where $\hat{\mathbf{z}}_n$ is shown in Fig. 2.4.

Equation (2.2) means that $\mathbf{v}_{p'_s}$ can have a velocity relative to $\{p\}$ only along $\hat{\mathbf{z}}_n$. Let $\mathbf{v}_{p'_m}$ designate the unconstrained velocity of point **p**' as given by the master interface. Also,

Let $\mathbf{v}_{p'_s}$ designate the constrained velocity of point **p'** as given to the slave robot high level controller. Equating the component of $\mathbf{v}_{p'_m}$ along the robot stem to the component of $\mathbf{v}_{p'_s}$ along the robot stem results in the following constraint filter in Eq.(2.3).

$$\mathbf{v}_{p'_s} = (\mathbf{v}_{p'_m}^T \hat{\mathbf{z}}_n)\hat{\mathbf{z}}_n \tag{2.3}$$

where $\mathbf{v}_{p'_m}$ is calculated using:

$$\mathbf{v}_{p'_m} = \mathbf{v}_{n_m} - \boldsymbol{\omega}_{n_m} \times (\mathbf{n} - \mathbf{p}) \tag{2.4}$$

Finally, the constrained end effector twist is given by:

$$\mathbf{v}_{n_s} = \mathbf{v}_{p'_s} + \boldsymbol{\omega}_{n_s} \times (\mathbf{n} - \mathbf{p}), \quad \boldsymbol{\omega}_{n_s} = \boldsymbol{\omega}_{n_m} \tag{2.5}$$

2.2.3 Kinematic Modeling for Constrained Ocular Telemanipulation

Though one needs at least two robotic stems to manipulate the eye [4], in this section we model manipulating the eye using one stem assuming external constraint such as friction is able to prevent unconstrained rotation about the axis connecting the eye center point o and incision point p.

This telemanipulation mode allows the surgeon to tilt the eyeball about its center using the robot stem. The kinematic constraint due to the eye incision is given by Eq.(2.2), which requires that $\mathbf{v}_{p'_s}$ and $\mathbf{v}_{p_s}$ share the same projection of velocity on the $\hat{\mathbf{x}}_n$-$\hat{\mathbf{y}}_n$ plane. We also prevent the robot stem from moving freely along $\hat{\mathbf{z}}_n$ direction as this may inadvertently result in perforation of the retina. We thus specify zero slip velocity along the stem and the kinematic constraint is:

$$\mathbf{v}_{p'_s} = \mathbf{v}_{p_s} \tag{2.6}$$

During constrained ocular telemanipulation the eye is purely rotating hence $\mathbf{v}_{p_s}^T \hat{\mathbf{r}} = 0$, where

$\hat{\mathbf{r}}$ designates a unit vector pointing from the incision point to the eye center.

$$\hat{\mathbf{r}} = \frac{\mathbf{p} - \mathbf{o}}{\|\mathbf{p} - \mathbf{o}\|} \tag{2.7}$$

Thus from Eq.(2.6), $\mathbf{v}_{p'_s}^T \hat{\mathbf{r}} = 0$. Thus, $\mathbf{v}_{p'_s}$ is obtained from projecting $\mathbf{v}_{p'_m}$ onto the tangential plane of the eyeball at $\mathbf{p}$, resulting in the constraint filter of Eq.(2.8). The constraint end effector twist is also given by Eq.(2.5).

$$\mathbf{v}_{p'_s} = \mathbf{v}_{p'_m} - (\mathbf{v}_{p'_m}^T \hat{\mathbf{r}})\hat{\mathbf{r}} \tag{2.8}$$

2.2.4 Experimental Evaluation

We used the glass eyeball model shown in (Fig. 2.5-a). This model was made from a small light bulb (OD 34mm), whose top was cut by diamond knife, and replaced by a rapid prototyped cover with three access holes of 1.5mm in diameter placed 9mm from top and separated by 120°. For eyeball tilting, we used the Constrained Ocular Telemanipulation. We evaluated tilting about all three axes. Figure 2.6 shows tilting about the x–axis. During these experiments the maximal linear and angular velocity of the robot were limited to 10 mm/sec and 10°deg/sec. We also used translational and rotational scalings: $k_t = 0.15$, $k_r = 0.5$. Theoretically, we must have two robot stems to fully constrain the eyeball. Since friction acted symmetrically as we tilted the eyeball about the x and y axes we were able to complete these motions. However, rotation about the z axis failed since this motion suffers more unbalanced friction from the support bearing, which results in tilting in the x and y directions. We also designed a membrane peeling experiment to demonstrate the Constrained Intraocular Telemanipulation. We coated the bottom of the glass eyeball model with agar layer [230] and used liquid bandage (NEW-SKIN 0.3 FL OZ. Liquid Bandage) to create the membrane [231] (Fig. 2.5-b). We mixed 1g of agar with 50mL distilled water, heated it to boiling for 1 min, cooled it down to 70° and then poured it

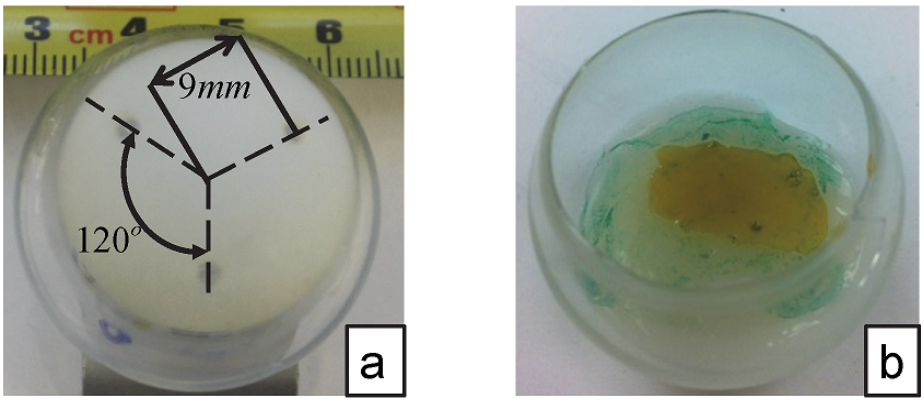

Figure 2.5: Customized phantom eye model a) Customized top; b) Agar-coated (green) glass eyeball with liquid bandage membrane (yellow)

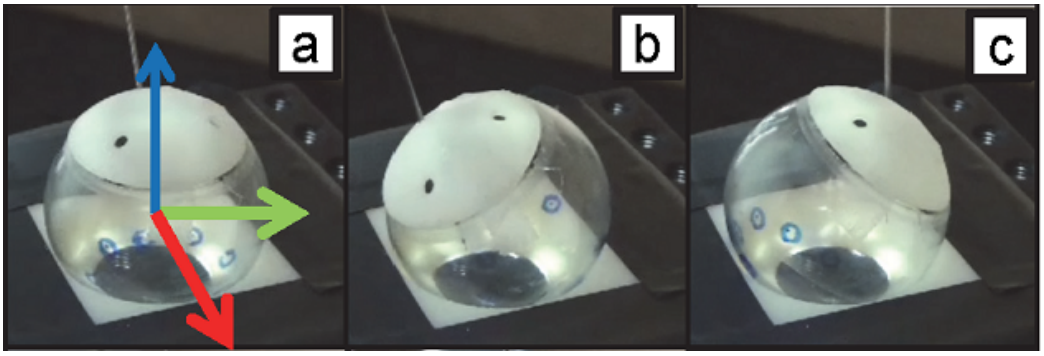

Figure 2.6: a)∼c): Demonstration of ocular motion about the x–axis

in the eyeball model. For OCT related experiments, the agar model needs to be opaque to provide imaging contrast. We thus mixed 1.2g of coffee mate into the agar after boiling. Air bubbles were eliminated using a sequence of de-airing cycles in a vacuum chamber while agar model was cooling down. We used a custom-made cam actuation unit for controlling an ophthalmic surgical gripper (BAUSCH+LOMB Storz vitreoretinal surgical gripper). A full membrane peeling procedure including insertion, grasping, lifting and detaching is shown in Fig. 2.7.

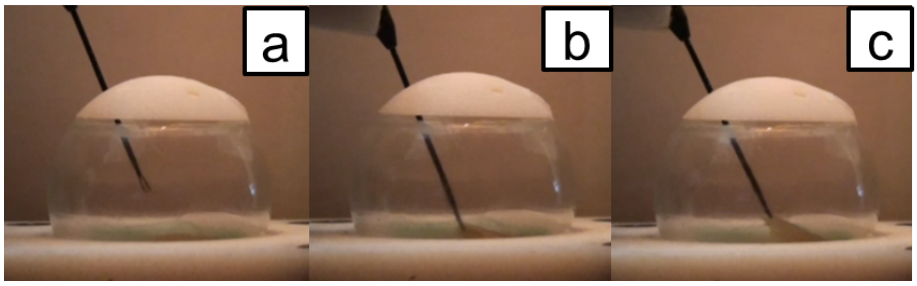

Figure 2.7: Membrane peeling experiment a) $\sim$ c) Membrane peeling procedures: inserting, lifting, detaching.

2.3 Constrained Kinematics for a Single-arm Robot with an Intraocular Dexterous Tool

In surgical interventions, such as ILM membrane peeling, surgeons are limited by the lack of intraocular dexterity with straight tools such as Alcon Grieshaber and Bausch Lomb Stroz grippers. This is the main reason for driving us towards developing an intraocular dexterous robot IODR. Since this is a highly redundant tool, during surgical interventions such as micro cannulation and membrane peeling the robot stem, even incorporated with the differential wrist and the IODR, will be treated as a straight tool in telemanipulation to be guided to target point $\mathbf{t}$ on the eye retina. During telemanipulation, the differential wrist and the IODR are both at the home configuration. Once the end-effector reaches the target point, the surgeon will be able to release the software-implemented lock on differential wrist and the IODR and allow the adjustment inside the eye. The reason for this arrangement is for the purpose of allowing the surgeon have a concise and straight-forward

telemanipulation sequence. This section is focused on developing the fundamental kinematic structure of the proposed robotic system and a situation will be presented to show the result of redundancy resolution. Future work will be focused on the path planning discussed above.

2.3.1 Nomenclature

The basic nomenclature is similar to what we have discussed in Fig. 2.4, but with the addition of a differential wrist and an IODR. Fig. 2.8 shows the new robot architecture. The differential wrist will be implemented between frame $\{m\}$ and $\{d\}$. We assume that the origin of frame $\{d\}$ lies at the center of the differential wrist actuation unit through which the IODR or other tools are deployed. For the differential wrist, the frame $\{d\}$ is defined as rotating by angle β_1 (ranging from 45° to 135°) about the $\hat{\mathbf{x}}_m$ axis from the frame $\{m\}$ and then rotating by angle β_2 (ranging from 0° to 360°) about the new $\hat{\mathbf{z}}_d$ axis in sequence. The end-effector frame $\{n\}$ is placed at the tip of the IODR stem and it is parallel to $\{d\}$ when at the homing position. The 3-DoF IODR has one DoF controlling the pre-shaped tube to allow the frame $\{n\}$ to rotate about $\hat{\mathbf{x}}_d$ axis with $-\gamma$ angle (red solid line in Fig. 2.4(b), γ ranging from 0° to 90°, the curvature of the preshaped tube is given by $\kappa = 1/\rho$). The second DoF will be controlling a straight guiding tube (green solid line in Fig. 2.4(b), the length of this guide wire is noted as s). The third DoF will be controlling the opening/closing of the gripper in membrane peeling task or a thin guide wire in the cannulation task. The tip of the supporting tube is $\{d_1\}$ and the tip of the bending tube is $\{d_2\}$. Although the Nitinol tube to build the robot stem is not rigid, we could assume that points $\mathbf{d}$, $\mathbf{p}$, $\mathbf{d_1}$, $\mathbf{d_2}$ and $\mathbf{n}$ are all in the same plane. The approach angle is defined as the η, which is the angle between axis $\hat{\mathbf{z}}_\mathbf{n}$ and the local tangential direction. σ is defined as the angle of the robot stem rotating about the axis pointing from incision point $\mathbf{p}$ to the target point $\mathbf{t}$. The home configuration for the differential wrist is $\beta_1 = 30^\circ$ and $\beta_2 = 0^\circ$. The home configuration for the IODR is $\gamma = 0^\circ$ and $s = 0$ as shown in Fig. 2.8.

2.3.2 Kinematic Constraint

The kinematic constraint on the incision point has been discussed before in Eq. (2.2). However in this kinematic derivation, we will treat the sclera constraint as a relation between the eyeball angular velocity and the joint speed. The other kinematic constraint is based on the desired slave twist at end-effector **n** that drives the robot towards target point **t**.

During the path planning of the surgical interventions, the controllable dimension for the tool is decided according to the surgeon's need. During ILM membrane peeling, we choose three independent components as the control input. The first input is an angular velocity $\dot{\eta}$, which changes the approach angle of the tool to the retina. The second input is also an angular velocity $\dot{\sigma}$ as shown in Fig. 2.8(b), which controls the rotation angle of the robot stem about the axis pointing from the incision point **p** to the target point **t**. The purpose of this second control input is to allow the surgeon to adjust the approach direction of the tool to the membrane edge. The third input is the linear velocity of the guiding tube $\dot{s}$.

The known parameters in this control algorithm includes:

1. Robot joint values:
   (a) $q_1 \sim q_6$ for parallel robot joint values.
   (b) q_7 and q_8 for two independent control on differential wrist angle β_1 and β_2 respectively.
   (c) $q_9 \sim q_{11}$ for three independent control on the IODR of the pre-shaped bending tube, the guiding tube and the gripper/guide wire.
2. All frames defined in robot base frame $\{b\}$: moving platform $\{m\}$, origin of the differential wrist $\{d\}$, incision point $\{p\}$, eye center $\{o\}$, tip of the supporting tube $\{d_1\}$, tip of the bending tube $\{d_2\}$, tip of the end-effector $\{n\}$ and the target position $\mathbf{t} = \mathbf{n}$.

3. Augmented configurational space velocity $\dot{\psi}$: $\dot{\psi} \triangleq [\mathbf{v}_m^T, \boldsymbol{\omega}_m^T, \dot{\beta}_1, \dot{\beta}_2, \dot{\gamma}, \dot{s}]^T$

4. Control input: $\dot{\mathbf{x}} = [\mathbf{v}_n^T, \boldsymbol{\omega}_n^T, \boldsymbol{\omega}_o^T]^T$

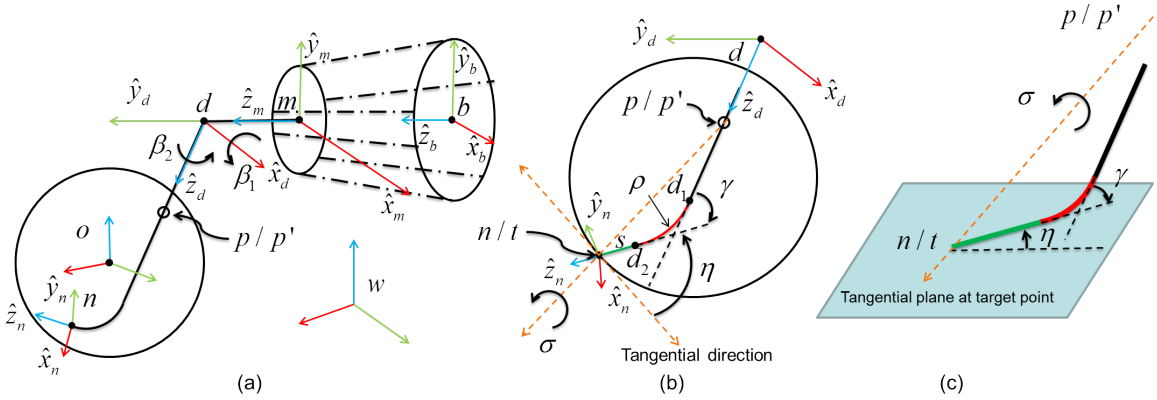

Figure 2.8: Kinematic nomenclature of on robot arm with an eyeball

2.3.3 Jacobian Derivation

The kinematic modeling presented in this section aims to find the Jacobian from the joint space to the task space. Since the parallel robot resolved rates is usually solved with closed form inverse kinematics, we choose the twist of the moving platform $\mathbf{t}_m = [\mathbf{v}_m{}^T, \boldsymbol{\omega}_m{}^T]^T$ instead of the parallel robot's linear actuator velocity as our joint space input. We first construct the direct kinematics of the IODR with the twist of frame $\{d\}$ as the input: $\mathbf{t}_d = [\mathbf{v}_d{}^T, \boldsymbol{\omega}_d{}^T]^T$.

$$\begin{aligned} \mathbf{v}_d &= \mathbf{v}_m + \boldsymbol{\omega}_m \times (\mathbf{d} - \mathbf{m}) \\ \boldsymbol{\omega}_d &= \boldsymbol{\omega}_m + \dot{\beta}_1 \hat{\mathbf{x}}_d + \dot{\beta}_2 \hat{\mathbf{z}}_d \end{aligned} \tag{2.9}$$

Thus, the velocity between frame $\{d\}$ and the input are:

$$\begin{bmatrix} \mathbf{v}_d \\ \boldsymbol{\omega}_d \end{bmatrix} = \mathbf{J}_d \begin{bmatrix} \mathbf{v}_m \\ \boldsymbol{\omega}_m \\ \dot{\beta}_1 \\ \dot{\beta}_2 \end{bmatrix} \tag{2.10}$$

where $\mathbf{J}_d$ is a 6×8 Jacobian

$$\mathbf{J}_d = \begin{bmatrix} \mathbf{I}_{3\times3} & \left[-(\mathbf{d}-\mathbf{m})\times\right] & \mathbf{0}_{3\times1} & \mathbf{0}_{3\times1} \\ \mathbf{0}_{3\times3} & \mathbf{I}_{3\times3} & \hat{\mathbf{x}}_d & \hat{\mathbf{z}}_d \end{bmatrix} \in \mathbf{R}^{[6\times8]} \tag{2.11}$$

Here notation $\left[\mathbf{a}\times\right]$ is the cross product matrix.

Similarly, the twist at the frame $\{d_1\}$ obtained as a parallel translation from frame $\{d\}$ and show in Fig. 2.8(b) is:

$$\begin{aligned} \mathbf{v}_{d_1} &= \mathbf{v}_d + \boldsymbol{\omega}_d \times (\mathbf{d_1} - \mathbf{d}) \\ \boldsymbol{\omega}_{d_1} &= \boldsymbol{\omega}_d \end{aligned} \tag{2.12}$$

And rewriting the above equation in the Jacobian term:

$$\begin{bmatrix} \mathbf{v}_{d_1} \\ \boldsymbol{\omega}_{d_1} \end{bmatrix} = \mathbf{J}_{d_1} \begin{bmatrix} \mathbf{v}_m \\ \boldsymbol{\omega}_m \\ \dot{\beta}_1 \\ \dot{\beta}_2 \end{bmatrix} \tag{2.13}$$

Where

$$\mathbf{J}_{d_1} = \begin{bmatrix} \mathbf{I}_{3\times3} & \left[-(\mathbf{d_1}-\mathbf{d})\times\right] \\ \mathbf{0}_{3\times3} & \mathbf{I}_{3\times3} \end{bmatrix} \mathbf{J}_d \in \mathbf{R}^{[6\times8]} \tag{2.14}$$

The twist at the frame $\{d_2\}$ is:

$$\begin{aligned} \mathbf{v}_{d_2} &= \mathbf{v}_{d_1} + \boldsymbol{\omega}_{d_1} \times (\mathbf{d_2} - \mathbf{d_1}) + \rho\,\dot{\gamma}\hat{\mathbf{z}}_{d_2} \\ \boldsymbol{\omega}_{d_2} &= \boldsymbol{\omega}_{d_1} - \dot{\gamma}\hat{\mathbf{x}}_{d_1} \end{aligned} \tag{2.15}$$

The twist at the frame $\{n\}$ is:

$$\begin{aligned} \mathbf{v}_n &= \mathbf{v}_{d_2} + \dot{s}\hat{\mathbf{z}}_{d_2} \\ \boldsymbol{\omega}_n &= \boldsymbol{\omega}_{d_2} \end{aligned} \tag{2.16}$$

Combining the two equations above results in the twist at the frame $\{n\}$:

$$\begin{aligned} \mathbf{v}_n &= \mathbf{v}_{d_1} + \boldsymbol{\omega}_{d_1} \times (\mathbf{d_2} - \mathbf{d_1}) + \rho\,\dot{\gamma}\hat{\mathbf{z}}_{d_2} + \dot{s}\hat{\mathbf{z}}_{d_2} \\ \boldsymbol{\omega}_n &= \boldsymbol{\omega}_{d_1} - \dot{\gamma}\hat{\mathbf{x}}_{d_1} \end{aligned} \tag{2.17}$$

Thus rewriting Eq.(2.17) in matrix format results in:

$$\begin{bmatrix} \mathbf{v}_n \\ \boldsymbol{\omega}_n \end{bmatrix} = \begin{bmatrix} \mathbf{I}_{3\times3} & \left[-(\mathbf{d_2} - \mathbf{d_1})\times\right] & \hat{\mathbf{z}}_{d_2} & \hat{\mathbf{z}}_{d_2} \\ \mathbf{0}_{3\times3} & \mathbf{I}_{3\times3} & -\hat{\mathbf{x}}_{d_1} & \mathbf{0}_{3\times1} \end{bmatrix} \begin{bmatrix} \mathbf{v}_{d_1} \\ \boldsymbol{\omega}_{d_1} \\ \dot{\gamma} \\ \dot{s} \end{bmatrix} \tag{2.18}$$

And from Eq. (2.13), by adding all the joint speed on the right side, we obtain:

$$\begin{bmatrix} \mathbf{v}_{d_1} \\ \boldsymbol{\omega}_{d_1} \\ \dot{\gamma} \\ \dot{s} \end{bmatrix} = \begin{bmatrix} \mathbf{J}_{d_1} & \mathbf{0}_{6\times2} \\ \mathbf{0}_{2\times8} & \mathbf{I}_{2\times2} \end{bmatrix} \begin{bmatrix} \mathbf{v}_m \\ \boldsymbol{\omega}_m \\ \dot{\beta}_1 \\ \dot{\beta}_2 \\ \dot{\gamma} \\ \dot{s} \end{bmatrix} \tag{2.19}$$

So from Eq. (2.18) and (2.19), the overall Jacobian $\mathbf{J}_n$ can be written as following:

$$\mathbf{J}_n = \begin{bmatrix} \mathbf{I}_{3\times3} & \left[-(\mathbf{d_2}-\mathbf{d_1})\times\right] & \hat{\mathbf{z}}_{d_2} & \hat{\mathbf{z}}_{d_2} \\ \mathbf{0}_{3\times3} & \mathbf{I}_{3\times3} & -\hat{\mathbf{x}}_{d_1} & \mathbf{0}_{3\times1} \end{bmatrix} \begin{bmatrix} \mathbf{J}_{d_1} & \mathbf{0}_{6\times2} \\ \mathbf{0}_{2\times8} & \mathbf{I}_{2\times2} \end{bmatrix} \in \mathbf{R}^{[6\times10]} \tag{2.20}$$

with the relation between the joint speed and end-effector twist:

$$\begin{bmatrix} \mathbf{v}_n \\ \omega_n \end{bmatrix} = \mathbf{J}_n \begin{bmatrix} \mathbf{v}_m \\ \omega_m \\ \dot{\beta}_1 \\ \dot{\beta}_2 \\ \dot{\gamma} \\ \dot{s} \end{bmatrix} \tag{2.21}$$

The kinematic modeling above did not take into account the sclera incision constraint. The RCM constraint requires the robot stem and the eye incision point to share the same velocity projected onto the normal plane of stem axis ($\hat{\mathbf{z}}_d$). This constraint could be summarized as following:

$$\begin{aligned} \hat{\mathbf{x}}_d^T \mathbf{v}_p &= \hat{\mathbf{x}}_d^T \mathbf{v}_{p'} \\ \hat{\mathbf{y}}_d^T \mathbf{v}_p &= \hat{\mathbf{y}}_d^T \mathbf{v}_{p'} \end{aligned} \tag{2.22}$$

Let matrix $\mathbf{G}$ be defined as:

$$\mathbf{G} \triangleq [\hat{\mathbf{x}}_d, \hat{\mathbf{y}}_d]^T \in \mathbf{R}^{[2\times3]} \tag{2.23}$$

The constraint equation Eq.(2.22) becomes:

$$\mathbf{G}\mathbf{v}_p = \mathbf{G}\mathbf{v}_{p'} \tag{2.24}$$

The instantaneous speed of the incision point on the stick p' could be calculate from rigid

body kinematics of the robot stem and the instantaneous speed of the incision point on the eyeball $\mathbf{p}$ could be calculated from the angular motion $\boldsymbol{\omega}_o$ of the eyeball.

$$\begin{aligned} \mathbf{v}_p &= \boldsymbol{\omega}_o \times (\mathbf{p} - \mathbf{o}) \\ \mathbf{v}_{p'} &= \mathbf{v}_d + \boldsymbol{\omega}_d \times (\mathbf{p} - \mathbf{d}) \end{aligned} \tag{2.25}$$

And we could write these relation in matrix format:

$$\begin{aligned} \mathbf{v}_p &= \left[-(\mathbf{p} - \mathbf{d})\times \right] \boldsymbol{\omega}_o \\ \mathbf{v}_{p'} &= \left[\mathbf{I}_{3\times 3} \quad \left[-(\mathbf{p} - \mathbf{d})\times \right] \right] \mathbf{J}_d \begin{bmatrix} \mathbf{v}_m \\ \boldsymbol{\omega}_m \\ \dot{\beta}_1 \\ \dot{\beta}_2 \end{bmatrix} \end{aligned} \tag{2.26}$$

So the overall constraint equation is:

$$\mathbf{G} \left[\mathbf{I}_{3\times 3} \quad \left[-(\mathbf{p} - \mathbf{d})\times \right] \right] \mathbf{J}_d \begin{bmatrix} \mathbf{v}_m \\ \boldsymbol{\omega}_m \\ \dot{\beta}_1 \\ \dot{\beta}_2 \end{bmatrix} = \mathbf{G} \left[-(\mathbf{p} - \mathbf{d})\times \right] \boldsymbol{\omega}_o \tag{2.27}$$

Finally we define the following matrices, which will be used in the following section.

$$\begin{aligned} \mathbf{A} &\triangleq \mathbf{G} \left[\mathbf{I}_{3\times 3} \quad \left[-(\mathbf{p} - \mathbf{d})\times \right] \right] \mathbf{J}_d \in \mathbf{R}^{[2\times 8]} \\ \mathbf{B} &\triangleq \mathbf{G} \left[-(\mathbf{p} - \mathbf{d})\times \right] \in \mathbf{R}^{[2\times 3]} \end{aligned} \tag{2.28}$$

2.3.4 Redundancy Resolution

Combining Eq. (2.21) and (2.27), we have the overall Jacobian relating the control input and output. The control input includes parallel robot moving platform twist, the configu-

rational speeds of the differential wrist and the joint speeds of the IODR. The augmented configurational space speed is defined as $\dot{\psi}$. The control output includes the end-effector twist and the angular velocity of the eyeball.

$$\begin{bmatrix} \mathbf{J}_n \\ \mathbf{A}\ \mathbf{0}_{2\times 2} \end{bmatrix} \begin{bmatrix} \mathbf{v}_m \\ \omega_m \\ \dot{\beta}_1 \\ \dot{\beta}_2 \\ \dot{\gamma} \\ \dot{s} \end{bmatrix}_{10\times 1} = \begin{bmatrix} \mathbf{I}_{6\times 6} & \mathbf{0}_{6\times 3} \\ \mathbf{0}_{2\times 6} & \mathbf{B} \end{bmatrix} \begin{bmatrix} \mathbf{v}_n \\ \omega_n \\ \omega_o \end{bmatrix}_{9\times 1} \tag{2.29}$$

Based on the definition of $\dot{\psi}$ and $\dot{\mathbf{x}}$, the constraint equation (2.29) is rewritten as:

$$\mathbf{J}_A \dot{\psi} = \mathbf{J}_B \dot{\mathbf{x}} \tag{2.30}$$

2.3.5 Task Priority Redundancy Resolution for Intraocular Manipulation

Equation (2.29) presents nine equations with ten configuration speeds. While one could use the minimum norm solution $\dot{\psi} = {J_A}^{+} J_B \dot{\mathbf{x}}$. This may not be the best approach. Instead, we consider a task priority redundancy resolution [232] because the robot must satisfy the scleral constraints and the safe eye manipulation task while using the remaining redundancy to satisfy ene-effector motion within the eye. The other rationale is that the IODR together with the wrist and the parallel robot can satisfy only five independent DoF within the eyeball due to the incisional constraints imposed by the sclera. This suggests that $\mathbf{v}_n$ and ω_n are not independent therefore reducing the number of independent equations in Eq. (2.29) to 8 independent equations.

Following the task priority redundancy resolution in [232], the Jacobians could be de-

fined as following:

$$\begin{aligned}
\mathbf{J}_1 &= \begin{bmatrix} \mathbf{A} & \mathbf{0}_{2\times 2} \end{bmatrix} \in \mathbf{R}^{[2\times 10]} \\
\mathbf{J}_2 &= \begin{bmatrix} \mathbf{0}_{2\times 6} & \mathbf{B} \end{bmatrix} \in \mathbf{R}^{[2\times 9]} \\
\mathbf{J}_3 &= \mathbf{J}_n \in \mathbf{R}^{[6\times 10]} \\
\mathbf{J}_4 &= \begin{bmatrix} \mathbf{I}_{6\times 6} & \mathbf{0}_{6\times 3} \end{bmatrix} \in \mathbf{R}^{[6\times 9]}
\end{aligned} \tag{2.31}$$

The redundancy resolution will have:

$$\begin{aligned}
&\textit{First task } (\textit{Sclera Constraint}): \ \mathbf{J}_1\dot{\psi} = \mathbf{J}_2\dot{\mathbf{x}} = \dot{\mathbf{y}}_1 \\
&\textit{Second task } (\textit{Eye Manipulation}): \ \mathbf{J}_3\dot{\psi} = \mathbf{J}_4\dot{\mathbf{x}} = \dot{\mathbf{y}}_2
\end{aligned} \tag{2.32}$$

From the first subtask, we could have the solution to $\dot{\psi}$, where $\mathbf{k}_1$ is the remaining redundancy in the system for future subtasks.

$$\dot{\psi} = \mathbf{J}_1{}^{+}\dot{\mathbf{y}}_1 + (\mathbf{I} - \mathbf{J}_1{}^{+}\mathbf{J}_1)\mathbf{k}_1 \tag{2.33}$$

For the second subtask, we substitute $\mathbf{J}_3\dot{\psi} = \dot{\mathbf{y}}_2$ into Eq.(2.3.5) and get:

$$\dot{\mathbf{y}}_2 - \mathbf{J}_3\mathbf{J}_1{}^{+}\dot{\mathbf{y}}_1 = \mathbf{J}_3(\mathbf{I} - \mathbf{J}_1{}^{+}\mathbf{J}_1)\mathbf{k}_1 \tag{2.34}$$

Let us define:

$$\widetilde{\mathbf{J}_3} = \mathbf{J}_3(\mathbf{I} - \mathbf{J}_1{}^{+}\mathbf{J}_1) \tag{2.35}$$

We could rewrite Eq.(2.3.5) as following:

$$\dot{\mathbf{y}}_2 - \mathbf{J}_3\mathbf{J}_1{}^{+}\dot{\mathbf{y}}_1 = \widetilde{\mathbf{J}_3}\mathbf{k}_1 \tag{2.36}$$

Then the solution to $\mathbf{k}_1$ is in Eq. (2.3.5) and $\mathbf{k}_2$ is for any more subtasks.

$$\mathbf{k}_1 = \widetilde{\mathbf{J}_3}^+(\dot{\mathbf{y}}_2 - \mathbf{J}_3\mathbf{J}_1{}^+\dot{\mathbf{y}}_1) + (\mathbf{I} - \widetilde{\mathbf{J}_3}^+\widetilde{\mathbf{J}_3})\mathbf{k}_2 \tag{2.37}$$

We could get the relation in Eq. (2.3.5) from [233].

$$(\mathbf{I} - \mathbf{J}_1{}^+\mathbf{J}_1)\widetilde{\mathbf{J}_3}^+ = \widetilde{\mathbf{J}_3}^+ \tag{2.38}$$

Then from Eq.(2.3.5), (2.3.5) and (2.3.5), we obtain the solution for the second task as:

$$\begin{aligned} \dot{\psi} &= \mathbf{J}_1{}^+\dot{\mathbf{y}}_1 + \widetilde{\mathbf{J}_3}^+(\dot{\mathbf{y}}_2 - \mathbf{J}_3\mathbf{J}_1{}^+\dot{\mathbf{y}}_1) + (\mathbf{I} - \widetilde{\mathbf{J}_3}^+\widetilde{\mathbf{J}_3})\mathbf{k}_2 \\ &= \mathbf{J}_1{}^+\mathbf{J}_2\dot{\mathbf{x}} + \widetilde{\mathbf{J}_3}^+(\mathbf{J}_4\dot{\mathbf{x}} - \mathbf{J}_3\mathbf{J}_1{}^+\mathbf{J}_2\dot{\mathbf{x}}) + (\mathbf{I} - \widetilde{\mathbf{J}_3}^+\widetilde{\mathbf{J}_3})\mathbf{k}_2 \end{aligned} \tag{2.39}$$

In this redundancy resolution solution for two subtasks, joint limits is another important constraint. Among configurational space velocities $\dot{\psi} = [\mathbf{v}_m, \boldsymbol{\omega}_m, \dot{\beta}_1, \dot{\beta}_2, \dot{\gamma}, \dot{s}]^T$, $\dot{\beta}_2$ is the only one without any joint limits. Let's define a as the lower limit, b as the higher limit, w_h as the highest weight, w_l as the lowest weight, and q_i as the i^{th} joint value. The weight element for the i^{th} joint will be given by a soft well function in Eq.(2.3.5) and the plot of this function with different p value is shown in Fig. 2.9. $p = 15$ controls the shape of the well.

$$W_i = w_h - w_l + \frac{w_h - w_l}{2}(1 - tanh(p(q-b))) - \frac{w_h - w_l}{2}(1 - tanh(p(q-a))) \tag{2.40}$$

The overall weight matrix is:

$$\mathbf{W} = diag([W_i]) \tag{2.41}$$

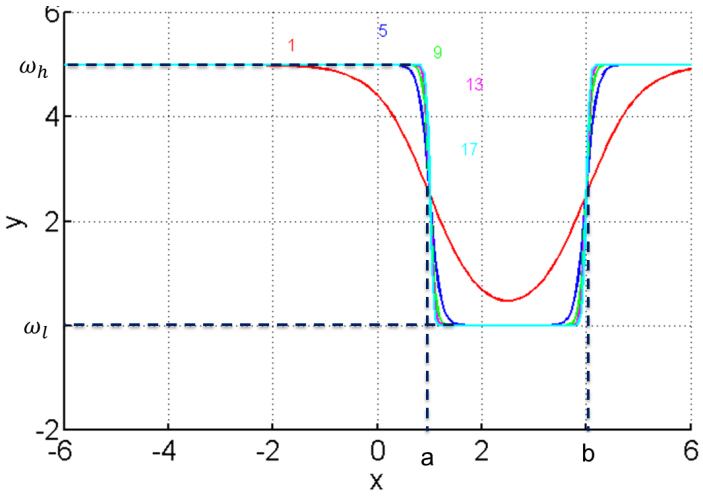

Figure 2.9: Soft Well.

2.3.6 Simulation

In Figure 2.10(a), the robot was commanded to move to a target configuration. Figure 2.10(b) and (c) shows the result of the robot end-effector $\{n\}$ converging to the target configuration $\{t\}$ in both translation and orientation.

2.4 Conclusions

In this chapter we summarized the previous work done by Wei in [1, 4] and pointed out the missing parts for safe telemanipulation. We presented our telemanipulation framework in [228] with straight tools and developed two constrained telemanipulation strategies that enable safe ocular manipulation and constrained intraocular tool manipulation while keeping the eye fixed. We introduced five more DoF into the robot system, with 2 DoF controlling the roll and yaw motion of the tool stem and 3 DoF controlling the bending, pushing and grasping at the stem tip. The Jacobian between the task space twist $\dot{\mathbf{x}}$ and the augmented configuration space velocity $\dot{\psi}$ is derived for this hybrid robotic system. Then the constraint on sclera incision point is introduced as a Jacobian relating the eyeball angular velocity $\boldsymbol{\omega}_o$ and $\dot{\psi}$. A task priority redundancy resolution is implemented to perform

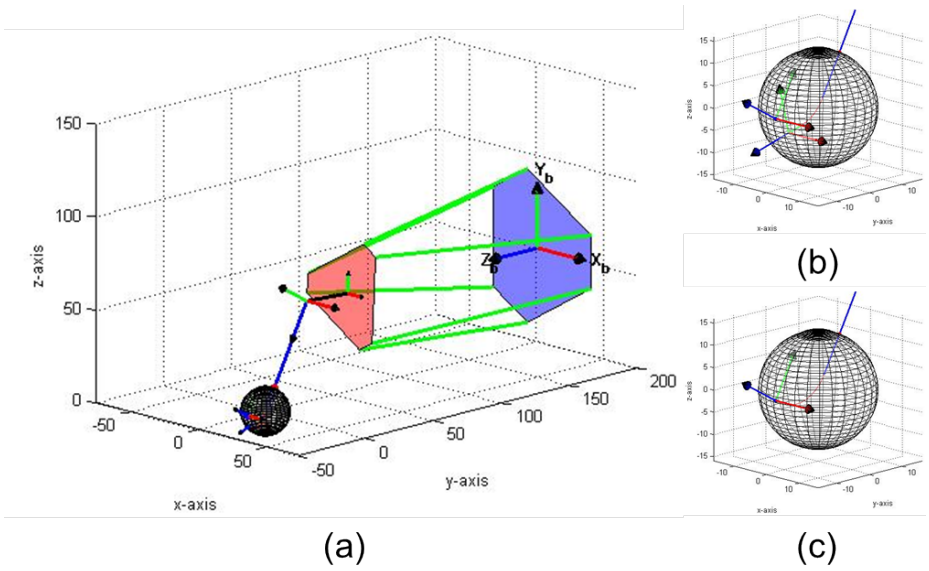

Figure 2.10: Simulation setup with the robot converging from the original setup to the desired setup.

resolved rates on the targeting tasks with the primary task to obey the sclera constraint and secondary task for intraocular manipulation. Simulation shows good convergence using this algorithm. The kinematic nomenclature and kinematic modeling presented in this chapter contributes to the evaluation study in Chapter 5 and the telemanipulation architecture in Chapter 6

Chapter 3

System Integration of OCT-guided Dual-arm Hybrid Robotic System

The purpose of this dissertation aims at presenting a dual-arm hybrid robotic system that integrates the OCT imaging for ophthalmic surgery. Chapter 2 presents the background kinematic modeling of the proposed robotic system. In this chapter, we focus on mechanical design and overall system integration. The chapter starts with improving the existing customized Stewart-Gough platform and designing the proposed IODR from Chapter 2. Design parameters of the B-mode OCT probe customized by our collaborating group and the integration of this OCT probe into our robotic system are presented. An experiment is carried out to evaluate the latency and accuracy of our proposed OCT-guided visual servoing. A customized multi-axes electric control box is also designed for this hybrid robotic system but details are not included in this dissertation.

3.1 Hybrid Robot Integration

3.1.1 Redesign of a Mini Stewart-Gough Platform

Wei Wei and Jian Zhang who worked formerly in the ARMA lab presented the first prototype of the Stewart-Gough parallel robot. The robot is a 6-SPS parallel robot with 6 custom designed linear actuators. The spherical joint are customized MBO bearings. The actuation unit contains six Steinmeyer 3mm ball screws and it is actuated by Maxon RE13 motor assemblies. The robot homing position is determined by limit switches mounted on each linear actuator.

The actual robot had several issues that resulted in mechanical assembly errors affecting accuracy and rigidity. The key problems are summarized as the following:

1. The old design had all the spherical joints press fit into the moving and base platform.

The disadvantage lies in three aspects: first, over time, the press fit will get loose and the spherical joint could slide inside the hole thus destroying the calibration of the robot; second, the press fit will result in the pressure on the ball bearing thus increasing the friction on the spherical joint and making it harder to drive the robot leg; third, the kinematic modeling assumed that the center of all the spherical joints lie in the same plane and the center of all the joints determine the origin of the frame attached to the moving and the base platform. If the spherical joint could slide inside the hole, the assumption will no longer hold and a calibration algorithm has to be integrated to calibrate the error along the sliding direction.

2. The old design had the linear actuator run by the Steinmeyer ball screw and the axial transition was prevented by a friction clamp. The problem with this design is that the clamp's set screw may get loose through time resulting in backlash in the linear actuator.

3. The old gear transmission from the motor to the gear on the ball screw had a gear ratio of more than 2:1. The problem of this gear ratio is that both the output torque on the gear attached to the ball screw and the resolution of control are worsened by half.

With the problems listed above, we made modification to the linear actuators, the moving and base platforms of the robot to overcome all the issues that may negatively affect the accuracy and rigidity of the robot. The new design is shown in Fig. 3.1. Some specifications and dimensions on this customized parallel robot is shown in Table 3.1 and Fig. 3.2.

The moving and base platform were redesigned and manufactured with accurate machined step that prevents the bearing from popping out. A moving platform lock plate and screws with washers were added to lock the wall of the spherical joints against the step. Set screws on the side have been added to adjust the friction between the ball and the wall of

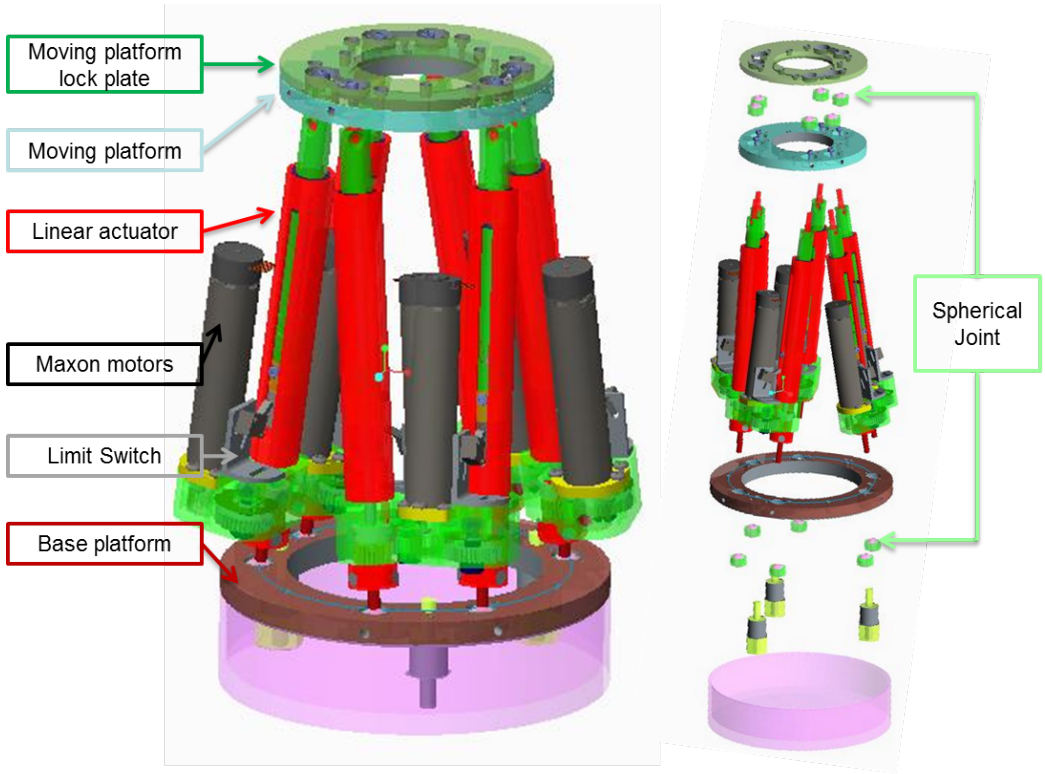

Figure 3.1: Stewart-Gough Platform assembly with 6 linear actuated legs and spherical joints.

Table 3.1: Parallel robot design parameters

Design parameters	
Base platform diameter	100mm
Base platform separation angle	20°
Moving platform diameter	70mm
Moving platform separation angle	15°
Leg stroke	120 to 180 mm
Maximum leg linear speed	10.356 mm/s
Leg moving resolution	5.89×10^{-5}mm/count

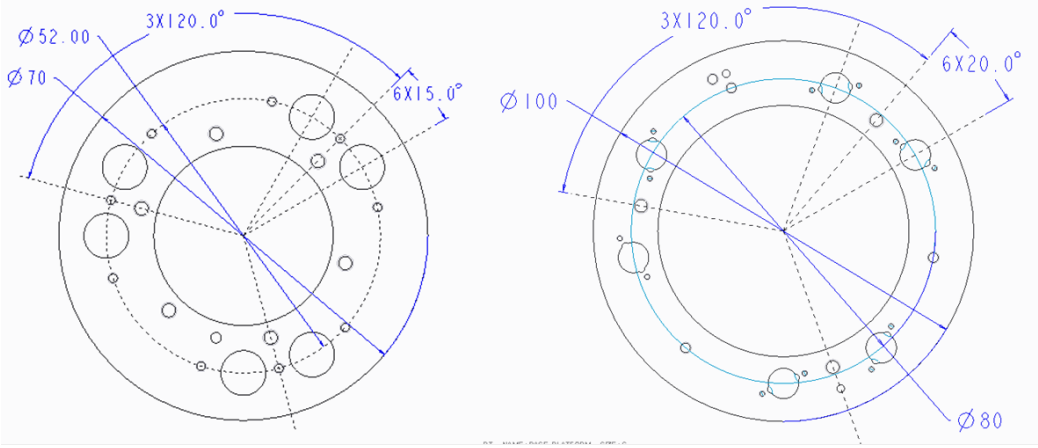

Figure 3.2: (a) Parallel robot moving platform dimensions. (b) Parallel robot base platform dimensions

the ball bearing. To evenly distribute the pressure on the wall, 3 slots have been cut outside of the ball bearing's wall in 120 degrees separation. An M2 nut was added to the end of the ball screw step to prevent the screw from being pulled out. A tiny amount of screw lock glue was added and the M2 nut was adjusted well to avoid friction between the face of the gear and the angular contact bearing. The three-gear design was carried out in Fig. 3.3 to replace the original two gear transmission. The input and output gear had a gear ratio of 1:1, thus maintaining a higher output torque and controllable resolution. The distance between the gears could also be adjusted (see Fig. 3.3).

3.1.2 Differential Wrist

A first version of the differential wrist was previously designed by former visiting students at ARMA lab. The initial design concept was done by Brian Lawson during an internship at ARMA lab. The design explored the possibilities including gear transmission and finalized the design with a wire actuated robot. The design did not turn into an assembled robot due to problems of transmission manufacturability and assembly. The proposed redesign is shown in Fig. 3.4. The differential wrist design contains three bevel gears. If

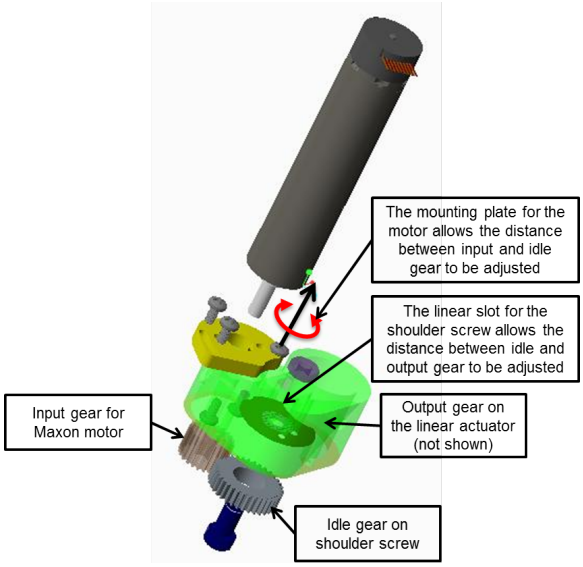

Figure 3.3: The input gear from the motor and output gear on the linear actuator has a gear ratio of 1:1 to allow the maximum possible output torque. The distance between the gears could all be adjusted as shown in the figure.

two input bevel gears rotate in opposite directions with the same angular velocity, the tool frame will have a pure yaw motion. On the other hand, if two input bevel gears rotate at the same angular velocity in the same direction, the tool frame will have a pure roll motion. Any other case will result in a combined roll and yaw rotation on the tool axis. The key challenges, as stated above, could be summarized in two aspects:

1. The intra-ocular dexterous robot has a weight of approximately 200 grams and the center of mass sits around 50mm above the center of the differential wrist. Thus the required torque to drive this robot will be approximately 100Nmm. So choosing the correct motor assemblies and the timing belt assemblies will be very important.

2. The shaft design is essential for meeting two requirements. First, the center piece that contains the three bevel gears should be assembled independently and the distance between the gears should be adjustable. The reason for this requirement is that the quick exchangeable plugin for the tool should be constrained well enough thus not allowing any motion besides the input from the two bevel gears. If the two input

bevel gears could slide along the axial direction, the tool to robot registration will no longer be accurate. Second, the transmission box that contains the timing belt assembly should be able to slide onto the differential gear box and the shaft position should be adjusted to avoid over constraint on the design.

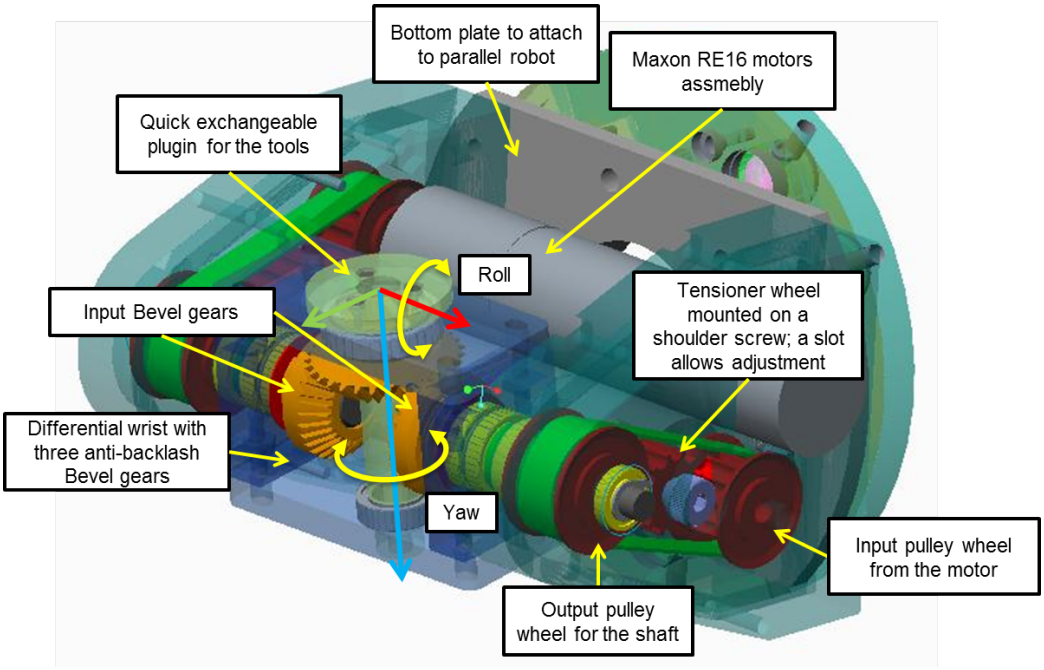

Figure 3.4: Differential wrist with 2 DoF controlling the roll and yaw motion of the tool stem.

The overall differential wrist design is shown in Fig. 3.4 with the bottom plate being attached to the Stewart-Gough parallel robot. Two RE16 motor assemblies (maximum continuous output torque 200Nmm) were used to supply the actuation for the two input bevel gears. The maximum continuous output torque for this motor assembly is sufficient to drive the assembly with the IODR. Tools including IODR and the OCT probe could be quickly attached to the center of the wrist box with a standard collet to hold the supporting stem. Details about the timing belt assembly is shown in Fig. 3.4. The timing belt is chosen from SDP-SI (GT2 Pitch 3mm, width 6mm, Kevlar reinforced Neoprene). The input pulley wheel has a tooth of 12 and the output pulley wheel 16, thus making the gear ratio 3:4. Both pulley wheels are customized to cut to a certain width for compactness. A tension wheel

was mounted on the shoulder screw and could slide with a slot on the cover to provide adjustment on the timing belt.

The shaft transmission is shown in Fig. 3.5. Each input bevel gear is mounted on the shaft and fixed onto the cover with two deep groove bearings, a shaft step and a snap ring. There are slots on the cover of the wrist box which allows sliding in the shaft axial direction. These slots are for adjusting the distance between the input bevel gear and the center bevel gear. Then the supporting box with the timing belt assembly was input onto the shaft and the position was locked with two flanged deep groove bearings, a shaft step and a snap ring. There are also slots on the bottom plate to allow adjustment on the shaft position to avoid over constraint.

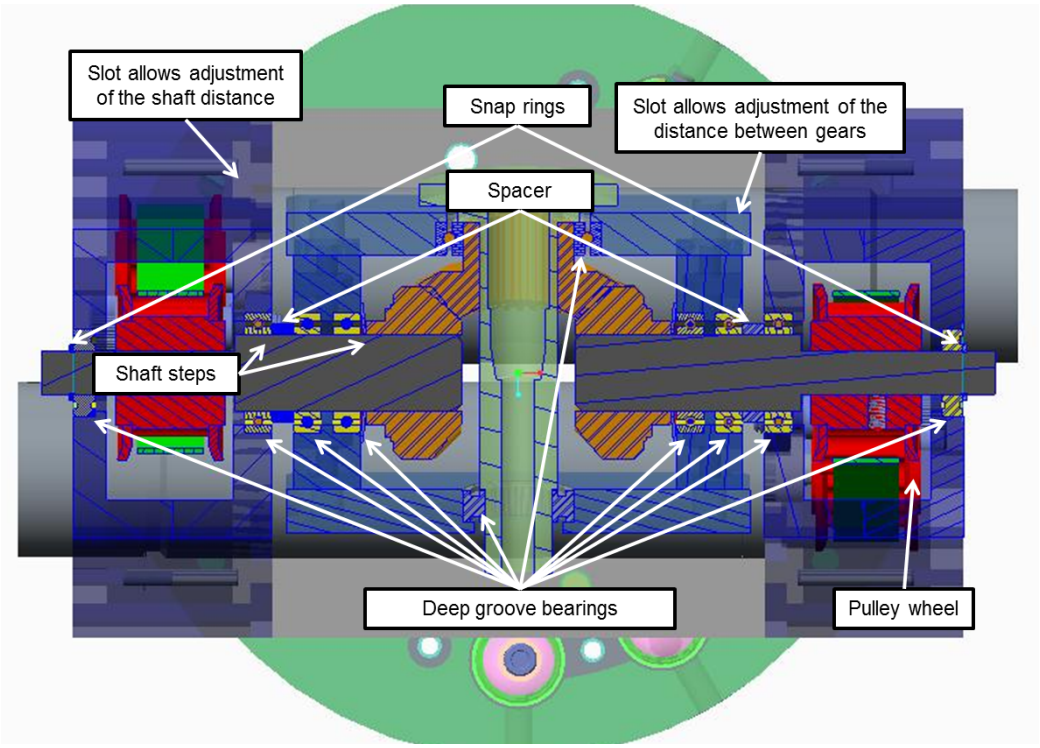

Figure 3.5: Cross-section view shows the shaft design.

3.1.3 Intra-ocular Dexterous Robot

The Intra-ocular Dexterous Robot provides intra-ocular dexterity. This robot is able to carry out different ophthalmic tasks based on different stems. In Fig. 3.6(a), the IODR robot was mounted on top of the parallel robot and the stem was inserted into a customized eye model. If we choose the stem as shown in Fig. 3.6(b), the IODR becomes the stenting deployment robot and allows deploying micro stents into blood vessels. If we choose the stem as shown in Fig. 3.6(c), the IODR controls a gripper. All the stems use set screws to connect to the linear slider's driving arm thus making it easy to be replaced. In the stent deployment robot, three DoF are independently controlled: the guide wire ⑥, the stent pushing tube ⑤ and the angle-adjustment tube ④. While the angle adjustment tube provides intraocular dexterity enabling controlled angle of approach to the retina, the guide-wire is used to guide deployment of the stent in blood vessels and the stent pushing tube is used to deploy the pre-loaded stent into the blood vessel. In the IODR gripper, only two DoF are controlled: the angle-adjustment tube ④ and push/pull on the customized gripper ⑨ to achieve opening and closing.

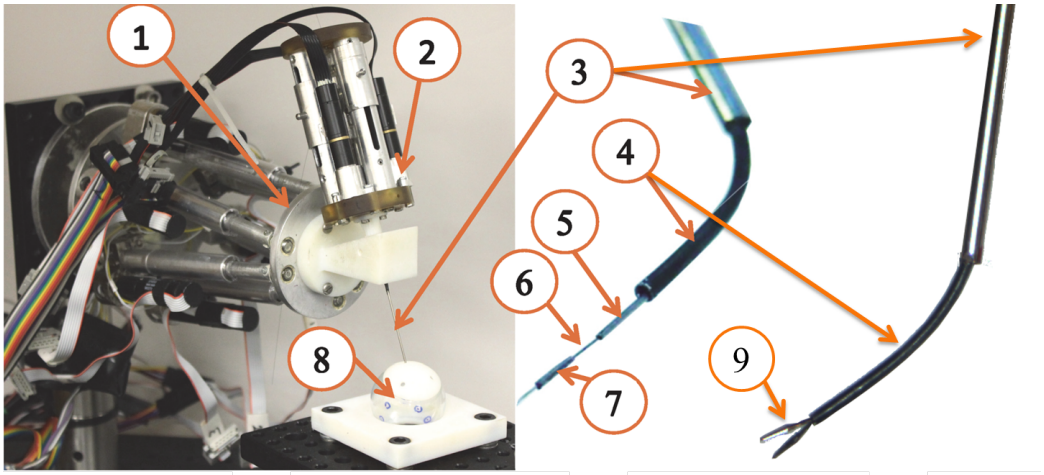

Figure 3.6: IODR. ① Parallel robot moving platform; ② stenting robot; ③ robot stem; ④ angle adjustment tube; ⑤ stent pushing tube; ⑥ guide wire; ⑦ stent; ⑧ eye model; ⑨ ophthalmic gripper

The IODR utilizes a similar design presented as the linear actuator for the parallel robot. The idle gear design transmits high torque and high resolution from the motor to the linear leg. The arm that drives each individual stem has a close running fit on the straight tube and the arm has a height of 30mm to avoid accuracy decrease resulted from the wobbling. The 182g cylindrical actuation unit is 84mm long and has a diameter of 42mm. Additional design specifications are shown in Table 3.2. The IODR connects to the parallel robot using a quick-changeable tool with a collet in front.

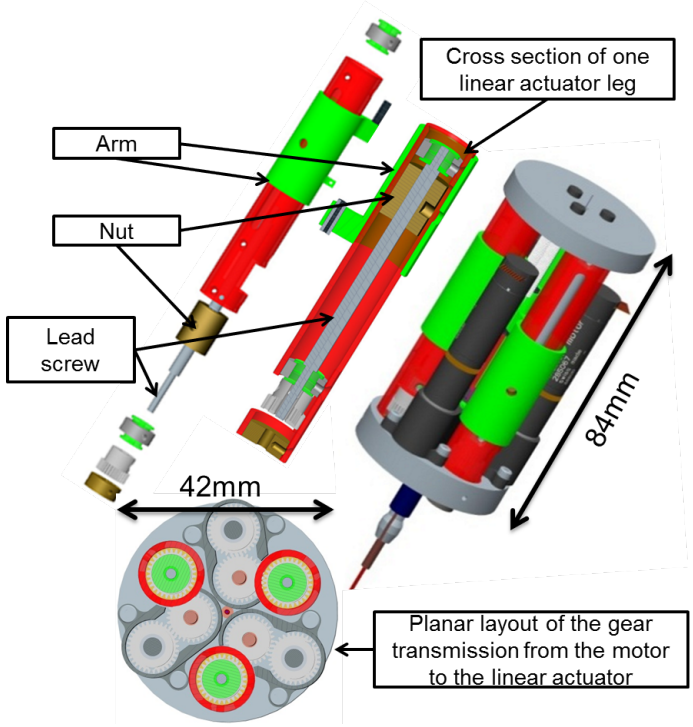

Figure 3.7: IODR actuator design

Table 3.2: Stenting deployment robot design parameters

Max motor shaft speed	**Gear ratio**	**Max leg linear speed**
10.4 rps	1	6.34 mm/sec
Max continuous torque	**Resolution**	**Stroke**
30 Nmm	1.5x10-4 mm/count	$\pm 10 \sim 15mm$

3.2 B-mode OCT Probe

3.2.1 Design Parameters

The detailed structure of the miniature 0.51 mm-diameter intraocular OCT probe was described in [162]. Briefly, this probe has a cylindrical body that is 90 to 100 mm long with a handpiece 12.7 mm in diameter and disposable 25-gauge extra-thin-wall probe tip (outer diameter = 0.51 mm, wall thickness = 70 μm, and length = 34 mm beyond the end of the handpiece). An electromagnetic linkage is embedded within the handpiece, to drive the 125 μm single-mode fiber optic actuator within the 25-gauge probe tip. The fiber can easily scan laterally up to 30Hz. The fiber scanning frequency was matched to the acquisition rate of an available commercial very high resolution (VHR) spectral-domain optical coherence tomography (SDOCT) system (870 nm, Bioptigen, Inc. Morrisville, NC) which permitted real-time viewing with highest resolution B-scan generation at 5Hz with 2000 A-scan lines per image. A sealed 0.35 mm diameter, 0.5 mm thick, $<$ 1/4 pitch, 0.95 numerical aperture GRIN lens (Go!Foton, Somerset, NJ) within the probe protected the fiber scanner and focused the scanning beam at the working distance 3 to 4 mm away from the probe. The axial resolution was $4-6\mu m$ and the lateral resolution was $25-35\mu m$ centrally and $32-45\mu m$ at the scanning edge periphery [162].

3.2.2 Exploring the Tilting Angle of the Probe

Because external OCT systems produce marked peripheral distortions with wide angle lenses [234, 235], knowledge of the maximal tilt angle is important. The eye has an oblate spheroid shape and the intraocular reach of all intraocular instruments are minimally constrained with a flexible pars plana sclerotomy. In addition, the usual placement of two flexible sclerotomy entry ports and performance of indentation of the peripheral retina will minimize tilt relative to the retinal surface. However, a region of the retina may be imaged at an angle using this probe. We tested the OCT probe in conditions whereby the probe's

imaging axis was at an angle θ from the image surface normal as the probe was tilted as shown in Fig. 3.8(a). The probe's tilting axis was perpendicular to the probe's scanning plane. Figures 3.8(b) and 3.8(c) show the OCT images of a cellophane tape roll with different θ angles when scanning longitudinally. The probe achieved the best scanning quality when the probe was -10° to the surface plane. The OCT image quality deteriorates as the probe tilted in both positive and negative directions. Beyond 30°, the image quality is no longer usable for guiding the surgery. Figures 3.8(b) and 3.8(c), show that the imaging surface is not flat. This distortion stems from the intrinsic lens and scanning parameters of the probe. A real-time algorithm to calibrate these intrinsic parameters in order to correct image distortion is presented in Chapter 4.

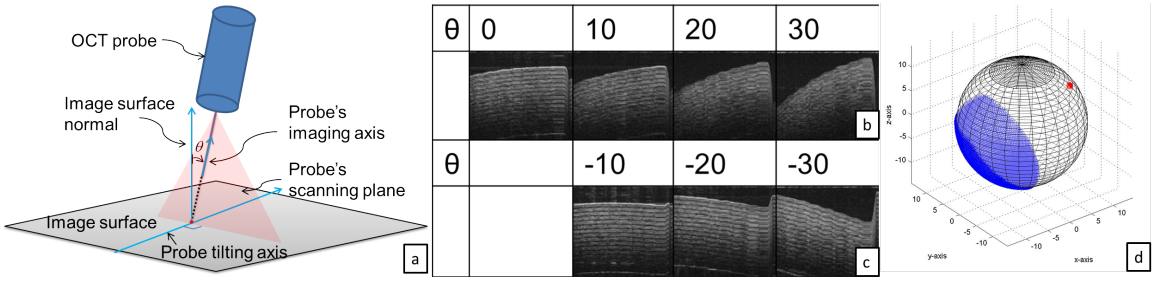

Figure 3.8: Diagram and images of a cellophane tape roll for different OCT tilts. (a) Diagram of a positive angle θ tilt from the normal direction. (b) Images produced when tilting longitudinally to the OCT scanning beam in (+) angle θ direction according to the right hand rule about the probe tilting axis. (c) Images produced when tilting in (-) θ direction according to the right hand rule about the probe tilting axis. (d) Resulting probe scanning workspace inside the eye.

3.2.3 Combined Forward-imaging B-scan OCT Probe and Forceps Design

A miniature B-scan OCT probe uniquely combined with an ophthalmic surgical forceps was designed with the probe positioned within the forceps rather than a forceps positioned within or adjacent to the OCT probe (Fig. 3.9(a) and 3.9(b)). To produce the coupled forceps, the front portion of the 25-gauge stainless steel tube (SST) was cut to form a forceps with 3.5 mm long tips, and positioned so that the OCT beam scan intersected both tips. The forceps tips were fabricated to be aligned with the cross-sectional center of the

probe, and located 3.5 mm distal to the OCT tip to be at the best focal point position. The forceps tips were mechanically aligned to match the scanning beam. A 23-gauge extra-thin wall SST was used to slide up and down the outside of the 25-gauge tube to cause opening and closure of the gripper manually (Fig. 3.9(a)). A manual gripper actuator was concentrically assembled around the OCT probe handpiece and attached to the 23-gauge tube to open/close the forceps (Fig. 3.9(b)). This actuator was designed and fabricated from a 0.005" thick stainless steel sheet. The length of the handles was approximately 42 mm with an actuation distance of approximately 1.5 mm. The distal handles were attached to the OCT handpiece with a hoop design. The proximal handles were attached to a plastic ring which was connected to the 23-gauge extra-thin wall SST on the forceps to actuate gripper closure. The OCT forceps may be used as either a hand-held instrument or integrated within a robotic system. One frame of the OCT image appearance of the forceps tips is illustrated in Fig. 3.9(c).

3.2.4 OCT Image Segmentation

The image segmentation technique used in this study includes speckle filtering, color map transformation (gray to black and white image) and canny edge detection. Figure 3.10 shows the result of segmenting the top surface of the retina. This image segmentation result will later be used on sending control feedback for assistive telemanipulation.

Speckle arises as a natural consequence of the limited spatial-frequency bandwidth of the interference signals measured in the OCT [236]. It is the reason why raw OCT images look noisy. However, speckle has a dual role as a source of noise and as a carrier of information about tissue microstructure. For OCT image segmentation, it is very important to remove the speckles from the image and at the same keep the original image information. To evaluate the functionality of different speckle filtering methods, several metrics include mean Squared Error, Minkowski Metric, Signal-to-noise ratio (SNR), Contrast-to-noise ratio (CNR), Universal image quality index, structural similarity index were developed

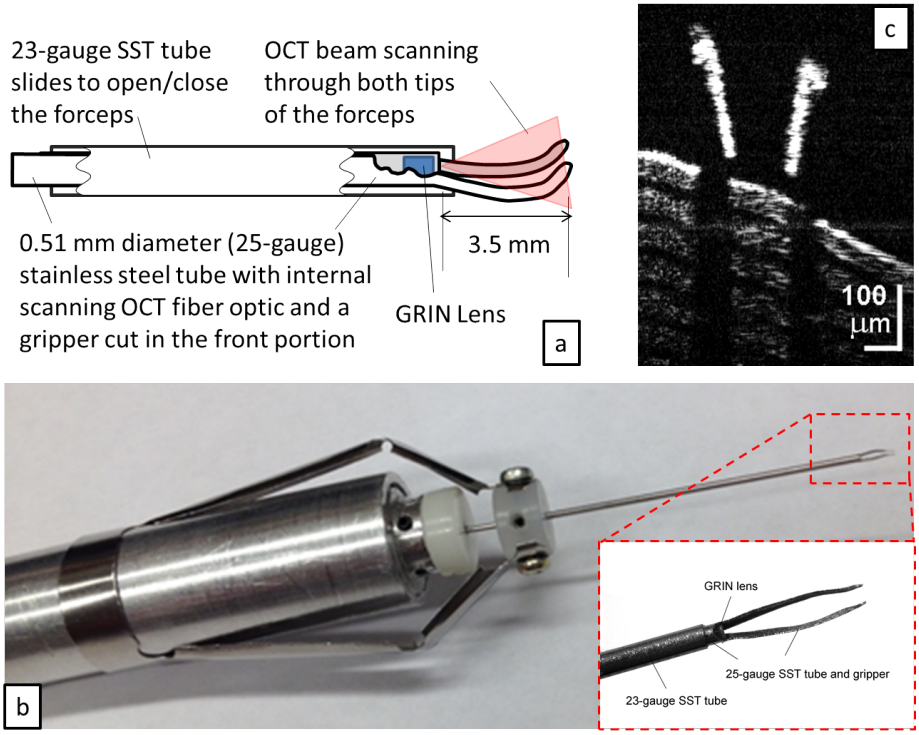

Figure 3.9: OCT-forceps probe design with OCT images of the probe's tips. (a) Drawing of the OCT-forceps probe design with an internal 0.51 mm diameter (25-gauge) stainless steel tube (SST) with embedded scanning OCT fiber optic and a gripper cut in the front portion. An external 23-gauge SST slides to open/close the forceps. The OCT beam scans through both tips of the forceps. (b) An external manual hand piece actuator causes the external 23-gauge SST tube to slide which opens/closes the forceps. (c) The unprocessed OCT image appearance of the forceps' tips is illustrated with real-time OCT imaging of the forceps' tips closing and opening demonstrated.

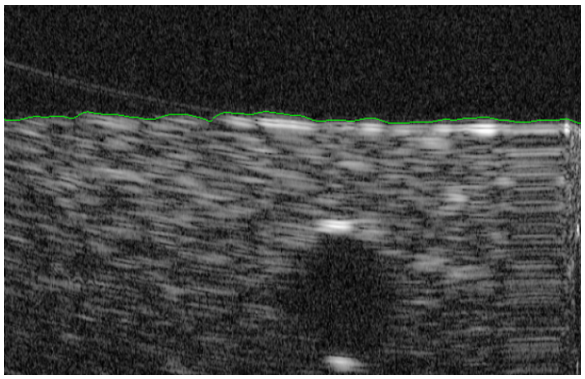

Figure 3.10: Image segmentation after dewarping, speckle filtering and edge detection

by different groups. As we need real-time image processing, short filtering time is also very important for ensuring minimal control latency. Spatial speckle filtering consists of moving a window kernel across an image and applying algorithms to adaptively compute the center pixel based upon the adjacent pixels. Within the kernel box, different algorithms are performed to smooth the image and remove ”edges” and ”valleys”. The most common, simple and fast speckle filtering methods are the mean filter and the median filter. The mean filter replaces the center pixel value of any kernel box with the mean value in the kernel box. Instead, the median filter replaces the value with the median value of the neighbourhood. Both methods are fast in calculation, however the mean filter does not remove the speckle but averages it into data and loses detail and resolution. Median filter shows better capability in filtering the image and does not blur the edges of the regions larger than the size of the window used. Thus the median filter is used in this segmentation code.

Canny edge detector is a very commonly implemented algorithm to detect edges in the image. It finds the intensity gradient map of the image to help determining the potential edges. Then the detection is finalized by suppressing all the edges that are weak and not connected based on the threshold. This edge detector is available in both Matlab and OpenCV. However, we developed a custom edge detector specifically for detecting the top surface of the retina.

Other image segmentation techniques that have been explored include hough transform to help detect straight lines and active contour to help find point clouds. The active contour method [237] may be used in the future to help find the point clouds of the tool and the blood vessel.

3.3 OCT-robot Integration

Figure 3.11 shows the conceptual setup and defines the key frames facilitating the definition of the problems addressed. Two frames are attached to the probe. Frame $\{s\}$ defines

the OCT scan plane such that $\mathbf{x}_s$ and $\mathbf{z}_s$ define the lateral and depth directions of the OCT image. The origin of this frame is located arbitrarily at the tip of the OCT probe and $\mathbf{y}_s$ completes this frame as a right-handed frame. Frame {p} is the OCT probe frame. It is defined with respect to a mechanical reference physically determined by the design of the probe housing. For example, a locating pin and the OCT stem are used to determine the $\mathbf{x}_p$ axis while the OCT stem is used to determine the $\mathbf{z}_p$ axis as shown in Figure 3.11. Axis $\mathbf{z}_p$ and axis $\mathbf{z}_s$ are parallel to each other. And angle γ designates the orientation of OCT scanning plane from the known pin direction, which is an important intrinsic parameter that needs to be calibrated.

In addition to these frames, we also define frames of the surgical robot as shown. Frame {b} is the base frame of the slave robot. Frame {m} is the frame of the moving platform of the robot. Frame {n} is the end effector frame. More detailed robot frames are defined in [228].

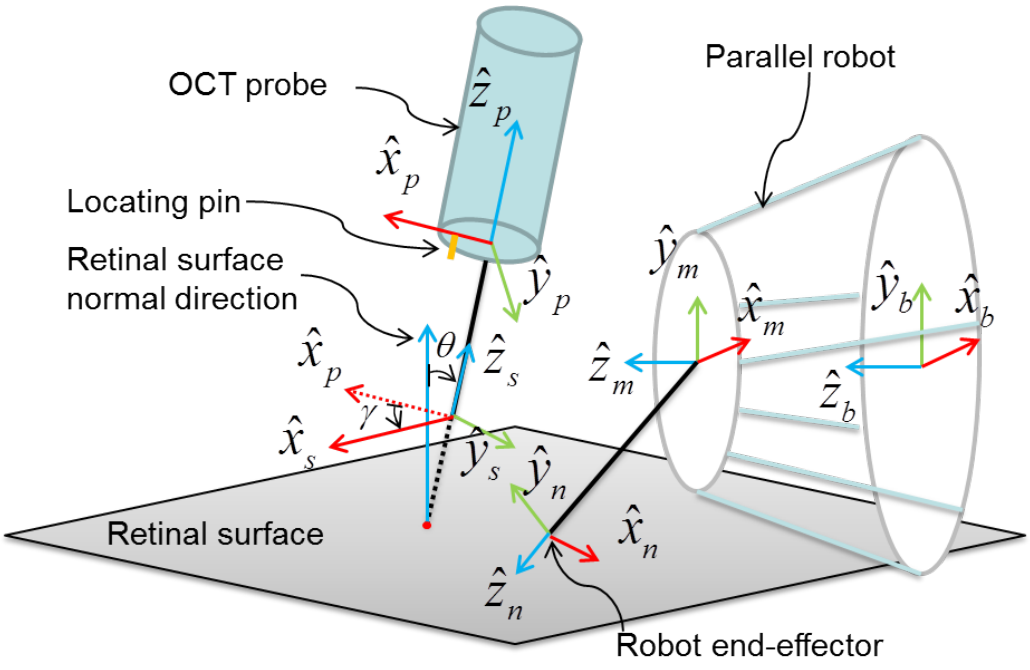

Figure 3.11: Conceptual setup and frames definition

3.3.1 Dual Rate OCT Visual Servoing Control

Our OCT-guided visual servoing control architecture is shown in Figure 3.12. This control architecture consists of four blocks. The name "dual rate" comes from the different real-time control rates in block C and D. Here are descriptions of each block:

1. Block A: Real-time OCT image acquisition from the scanning probe. The probe has an intrinsic scanning frequency of 5Hz.

2. Block B: Grab the real-time OCT image and process the image based on different control algorithms' needs. This is a C++ & Qt & OpenCV combined program that can run at 20Hz.

3. Block C: Based on the image processing results, the robot new reference configuration $\mathbf{x}_{ref}$ is calculated at 15Hz. The reason for choosing this frequency is that the real-time OCT image is acquired at 5Hz. So this block's frequency should be equal to or slightly over 5Hz. High frequency will result in transforming the high frequency noise from the OCT image to the control system and low frequency will result in slow and inaccurate control. ${}^{b}\mathbf{A}_{OCT}()$ is the affine transformation function from OCT image frame to robot base frame $\{\mathrm{b}\}$, $\mathbf{e}_p$ is the position error vector to the target in pixels from the OCT image and c is the pixel to mm scale of the OCT image at the local point.

4. Block D: With the reference robot configuration, the robot is controlled to move after high-level trajectory planning, inverse kinematics and low-level PID controller. This is running at 1kHz in real-time. Detailed description was presented in [228].

3.3.2 Evaluation of Visual Servoing Precision and Latency

To evaluate the robustness of the visual servoing architecture in Fig. 3.12, an experiment was designed to measure the latency and accuracy of visual servoing with the B-scan

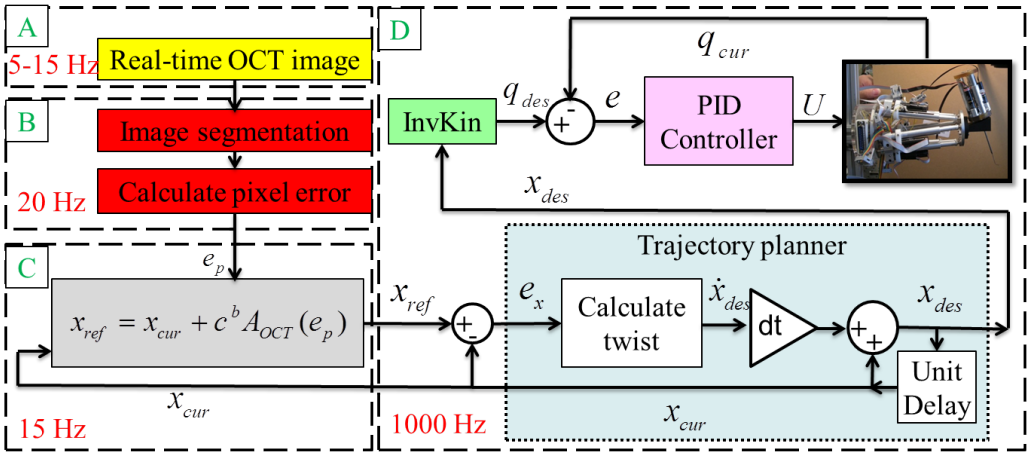

Figure 3.12: OCT-guided Visual Servoing Control Architecture: A) Real-time B-mode OCT image acquired from Custom-made miniature OCT probe (scanning frequency 5Hz); B) Segment the image and calculate the error in pixels (Segmentation frequency 20Hz); C) Calculate reference position (10 Hz) ; D) Trajectory planner and lower level PID controller (Target computer running in 1000Hz)

OCT probe integrated in the control loop. The setup is shown Fig. 3.13(a). A linear slide carried a piece of infra-red reflection paper and was programmed to move vertically in a sinusoidal manner. The parallel robot carried the OCT probe above the infra-red (IR) reflective paper. The visual servoing law was written to control the robot to keep a constant height above the IR reflective paper based on the measurement of the real-time OCT image. The latency and accuracy test will record and compare the input motion of the linear actuator and the output motion of the parallel robot and compare the motion to draw conclusion on the robustness of the visual servoing control law.

Figure 3.13 shows the results of the cyclic motion tracking experiments. In Figure 3.13(b) the reference position of the linear actuator holding the IR paper was changed in a step-wise manner therefore resulting in a sharp response of the linear actuator (shown in blue trace). The motion of the linear actuator was governed by a PID controller and a fifth-order polynomial trajectory planner with a desired motion time of 5 sec. The figure shows in red trace the motion of the parallel robot holding the OCT probe while attempting to maintain a fixed distance between the OCT probe tip and the OCT target. The latency of

response of the OCT motion (parallel robot) relative to the motion of the IR paper (linear actuator) is approximately $0.41s$. The steady state error to a step input had a mean value of 0.011mm and standard deviation of 0.01mm. The maximal error of tracking was 0.078mm.

We similarly repeated the experiment using a sinusoidal trajectory planner for the linear actuator holding the OCT target. Figures 3.13(c,d)) show the results of these experiments for different amplitudes of motion (0.3mm and 0.7mm). In both figures, the frequency of the sinusoidal motion was specified at 0.17Hz. The latency error for both experiments was $0.6s$. For the sinusoid input having 0.3mm amplitude the mean error in amplitude was 0.024mm and its standard deviation was 0.014mm. When the amplitude of the IR paper was increased to 0.7mm, the mean error in amplitude was 0.045mm and the standard deviation was 0.021mm.

These experiments demonstrate the efficacy and limitations of the control and OCT feedback method depicted in Fig. 3.12. The critical factor limiting the latency performance of our system is the rate of OCT image acquisition and processing. We are currently exploring an upgrade of our OCT engine and the actuator of the optic fiber inside the OCT probe with the aim of increasing the OCT acquisition frequency to at least 30 Hz. To further provide an evaluation of the expected performance of our system within the context of ophthalmic surgery, additional evaluation is provided in Chapter 6 while using automated path tracking along a surface with curvature similar to that of the human retina.

3.4 Control Electronics

For the general purpose of controlling the dual-arm system, we designed and assembled [1] the control electronics for driving 16 axes of motors. All the components are enclosed into a $8.75"H \times 19"W \times 22"D$ box. Necessary components for the electronic setup include 16 Line driver cables to eliminate long cables' defects, 16 Maxon LSC 30/2 amplifiers, 2 Contec CNT32-8M (PCI) encoder reading card, 2 Measurement Computing PCI-DDA

[1] Nima Sarli and Giuseppe Del Giudice from ARMA lab also contributed in the process.

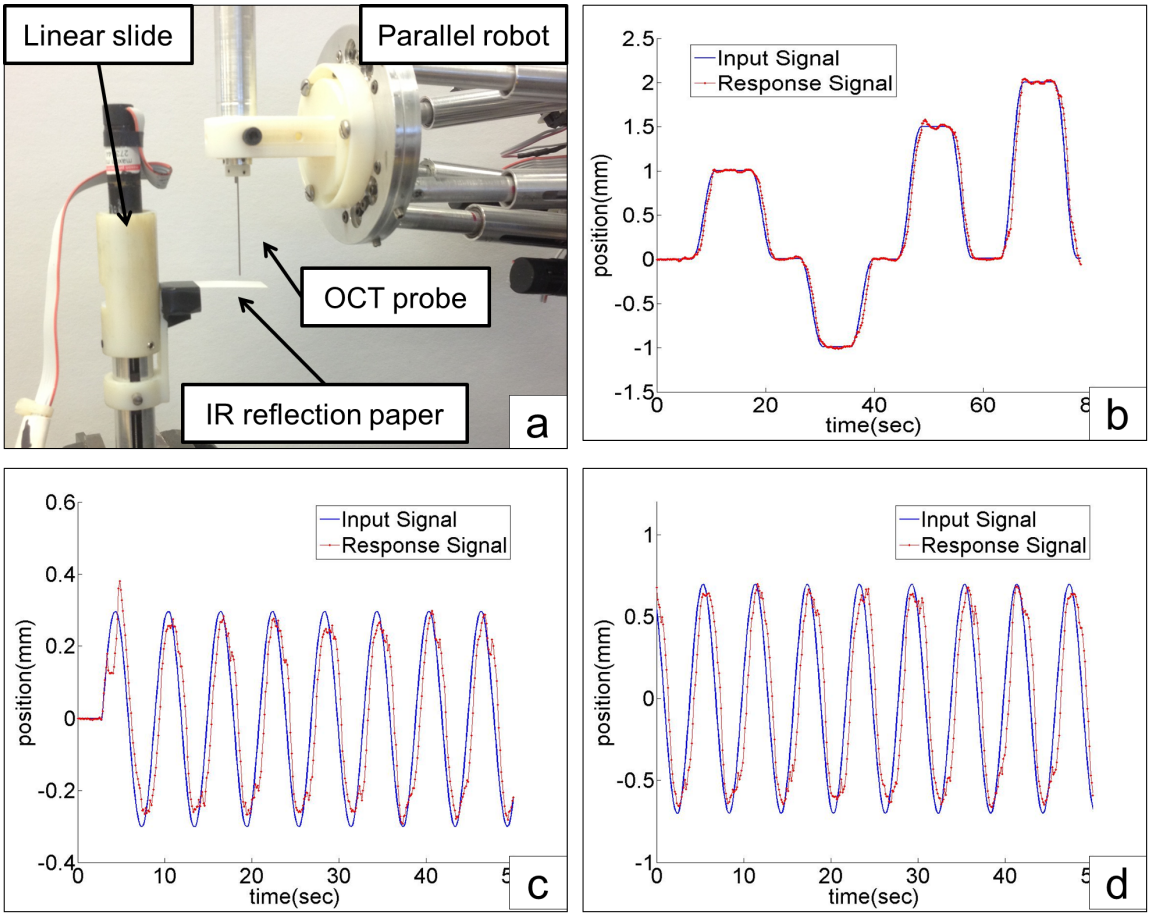

Figure 3.13: OCT guided visual servoing latency and accuracy experiment. (a) The setup consisted of a parallel robot carrying the OCT probe when viewing a moving IR reflection paper guided by a linear slide. (b) Slave robot responded to the step input from the linear slide. (c),(d) Slave robot responded to the sinusoid input from the linear slide with an amplitude of 0.3mm and 0.7mm respectively

08/12 data acquisition board and 16 encoder protection channels. Any maxon motors with or without differential encoder lines will become a 10pin connection after the line driver cable. Motor plus, motor minus, 5V and GND are connected to the Maxon LSC 30/2 amplifier accordingly. The set voltage plus/minus on the amplifier will be connected to the analog output on the measurement computing digital to analog board. The 6 channels of TTL encoder readings will go into the encoder protection circuit made by the line receiver chips and come out as only the channels without differential lines. These three differential lines of A, B and I will then be connected to the Contec encoder board for reading. Both the Measurement Computing and Contec cards are connected to the target computer that runs real time Matlab xpc code through PCI slots. A 24V power supply was embedded into the system to power all the amplifiers and the fan. A 5V regulator was designed to support the encoder protection circuit and the pull up resistors for the I/O channels. For grounding issues, both the digital and analog ground are connected together and linked to the ground of the 24V power supply.

Several PCB boards have been custom designed and manufactured including: a break-out board for all motors on robotic arms; a power distributor that takes 24V input and output both 24V and 5V; an encoder protection circuit PCB; break-out board for all Maxon amplifiers.

3.5 Conclusions

While many works addressed robot designs for robot assisted ophthalmic surgery, there are no robotic systems capable of both ocular manipulation and intraocular dexterity. Wei *et al.* [4] presented the idea of using actively controlled robot arms in ophthalmic surgery. In this chapter we presented our progress towards building such a telemanipulation system while focusing on describing our efforts to integrating a custom-made B-mode OCT probe for image guidance. This chapter includes the modification of our custom-made Stewart-Gough parallel robot, the design of a 2 DoF differential wrist, the design of 3 DoF IODR

providing intraocular dexterity, and a custom made B-mode OCT probe. The differential wrist provides roll and yaw motion on the straight part of the robot stem and IODR provides three independent DoF that each controls bending, pushing and grasping at the robot stem tip.

Optical coherence tomography imaging is valuable for identifying and diagnosing retinal disorders in the clinic. External microscope-mounted systems have demonstrated usefulness in examining retinal changes immediately following a surgical procedure in the operating room [137, 238, 142, 143, 144, 136]. However, it would be most valuable to image critical portions of the operation in real-time with OCT cross-sectional imaging. Microscope-mounted OCT systems have limitations in that normal metallic surgical instruments cast absolute shadows upon the underlying targeted tissues [137, 142, 143, 144] and investigators have reported difficulty in tracking the positions of moving surgical instruments within the eye [137, 142, 143]. A combined 23-gauge forward-imaging B-scan OCT-forceps was designed and developed for manual use or robotic-assisted integration for pre-clinical retinal surgery. Unlike other miniature forward-imaging probes, this probe has an internal scanning system so it can be held steady rather than moving the entire probe back-and forth to produce a two-dimensional B-scan image. The size of the OCT-forceps probe will permit passage through the current 23-gauge ports used in vitrectomy procedures. An advantage of an intraocular OCT probe is that it overcomes some of the problems associated with an external microscope-mounted OCT system. The probe bypasses the corneal and lenticular opacities that will degrade an OCT image. The intraocular probe can quickly be positioned and aimed at the areas of interest for imaging inspection. Co-planar integration of the forward-imaging B-scan probe with a surgical instrument permits constant tracking of the instrument tip without needing a tracking device embedded in the instrument. In addition, the instrument's position and approach to the tissue is provided with real-time feedback without requiring real-time layer segmentation or spatial compounding unless semi-automatic robotic control is desired. Finally, placing the OCT

imaging probe internal to the surgical tool improves the view of the desired target by reducing instrument shadowing.

The OCT and robot integration shows the result of using the OCT probe for visual servoing in Figure 3.12. A dual rate visual servoing control architecture has been implemented to increase the stability and robustness. Both step and sinusoidal input has been tested on the robot system.

The OCT-guided robotic system implemented from the combined work in this chapter contributes to the experimental evaluation in Chapter 5 and the assistive telemanipulation in Chapter 6. Especially, the dual rate visual servoing control is applied to the OCT-microscope combined 3D virtual fixture to help guide assistive telemanipulation in Chapter 6.

Chapter 4

Calibration

In Chapter 2 and Chapter 3, we presented the kinematic modeling and design integration of the proposed robotic system. To improve the performance, this chapter focuses on calibration of this robotic system. In the first section, we present algorithms for kinematic calibration of the customized parallel robot. The parallel robot calibration uses recursive least squares to solve for the mechanical uncertainties in the proposed robot and help improve the task space accuracy. The calibration also includes a method for calibrating the location of the incision points in the eye ball and the geometric dimension of the anatomy. This step is essential for active robot-guided retinal surgery since the robot manipulation is based on an estimated model of the eye. This calibration is a prerequisite process for model-based constrained telemanipulation developed in Chapter 6. This chapter also discusses the calibration related to our customized B-mode OCT probe. An OCT-robot integration has been presented in Chapter 3 and also shown in Fig. 1.7. Due to the unconformity in manufacturing and the intrinsic parameters of the scanning actuation unit in the B-mode OCT probe, the B-mode OCT image usually has a distortion. Calibrating the OCT probe distortion will improve the robustness of visual servoing algorithm from a perspective of safety. The OCT image information is represented in OCT image frame, which is located in the scanning plane of the OCT beam (Figure 3.11). A manual calibration algorithm is presented in this chapter to help find the registration between the locating pin on the probe body and the scanning plane. An approaching algorithm is proposed for defining the OCT scanning plane in robot frame with the total least square solution. However the actual experiment was not included in the scope of this dissertation. The parallel robot calibration is presented in [228]. Until the completion of this dissertation, OCT image distortion calibration and OCT scanning plane registration contribute partly to an accepted journal paper

[239] and rapid hollow calibration is contributing to a working paper submission.

4.1 Parallel Robot Calibration

4.1.1 Parallel Robot Calibration Algorithm

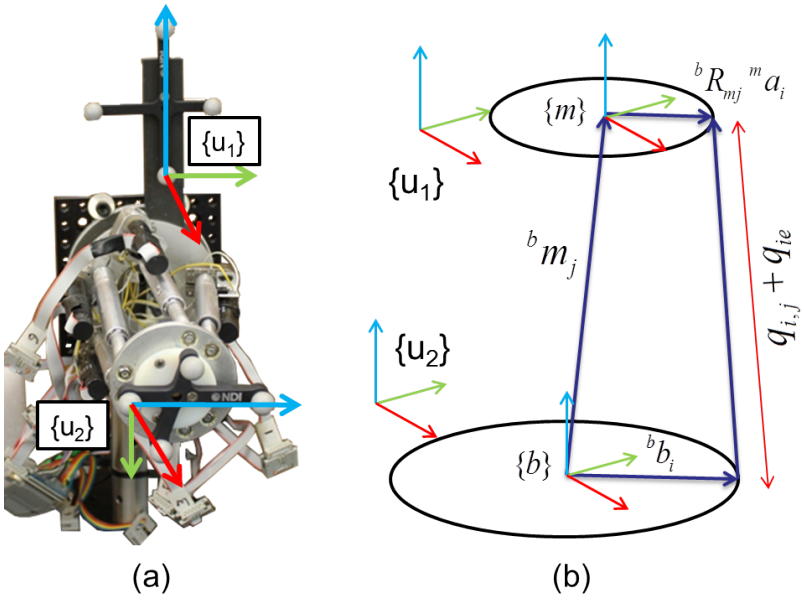

Figure 4.1: (a)Parallel robot calibration setup, (b)calibration kinematic diagram

We calibrated the parallel robot to minimize task space errors. These errors stem from uncertainty in the robot's leg lengths at home position and in the vertical positions of the robot's spherical joints, which were press fit in the base and moving platforms. We thus calibrated eighteen parameters (six leg lengths at home position and twelve vertical offsets of the spherical joints). Figure 4.1-a depicts the experimental setup with marker frames $\{u_1\}$ and $\{u_2\}$, which were attached at exact known positions with respect to frames $\{b\}$ and $\{m\}$, respectively. These frames were tracked using a Polaris Vicra tracker (0.25 mm RMS accuracy). The robot was moved to 150 randomized configurations within a work space of $\pm 15mm$ and $\pm 20^\circ$ of translation along and rotation about each axis. The robot was stopped at each configuration to allow static acquisition of its pose.

We henceforth use subscript $i = 1 \ldots 6$ to designate the i^{th} robot leg and $j = 1 \ldots n$ to refer to a calibration pose. We also define q_{h_i} as the assumed length of the i^{th} robot leg at the robot's home position, $\Delta q_{enc_{i,j}}$ as the encoder measured extension of the i^{th} leg relative to its home position when the robot is at its j^{th} calibration pose. In addition, we define $\mathbf{q}_{i,j}$ as the vector pointing from the spherical joint at the base platform to its corresponding bearing at the moving platform. Referring to Fig. 4.1-b, $\mathbf{q}_{i,j}$ is given by:

$$\mathbf{q}_{i,j} = {}^{b}\mathbf{m}_j + {}^{b}\mathbf{R}_{\mathbf{m}_j}\,{}^{m}\mathbf{a}_i - {}^{b}\mathbf{b}_i \in \mathbf{R}^{[3\times 1]} \tag{4.1}$$

Furthermore, the spherical bearing locations given in the moving/base platform frames are respectively designated by ${}^{m}\mathbf{a}_i = [*, *, a_i]^T$ and ${}^{b}\mathbf{b}_i = [*, *, b_i]^T$ where $*$ are known constants. So a_i and b_i designate the unknown errors in the vertical positions of the robot's spherical bearings.

We define $f_{i,j}$ as the i^{th} leg's loop closure error at the j^{th} robot pose, Eq. (4.2), where q_{e_i} designates the unknown error in the homing length of the i^{th} leg. The vector of loop closure errors at the j^{th} pose is defined as $\mathbf{f}_j$ and given in Eq. (4.3).

$$f_{i,j} \triangleq \sqrt{\mathbf{q}_{i,j}{}^{T}\mathbf{q}_{i,j}} - (q_{h_i} + \Delta q_{enc_{i,j}} + q_{e_i}) \in \mathbf{R}^{[1\times 1]} \tag{4.2}$$

for the j^{th} pose we define the vector $\mathbf{f}_j \in \mathbf{R}^{[6\times 1]}$ as:

$$\mathbf{f}_j \triangleq [f_{1,j}, \ldots, f_{6,j}]^T \tag{4.3}$$

Defining the vector of calibration parameters for i^{th} leg as $\mathbf{x}_i \triangleq [a_i, b_i, q_{e_i}]^T$, and the overall calibration parameters for the robot as $\mathbf{x} \triangleq [\mathbf{x}_1^T, \ldots, \mathbf{x}_6^T]^T \in \mathbf{R}^{[18\times 1]}$ one can cast the calibra-

tion problem into this minimization problem:

$$\begin{aligned} &\mathbf{x} = argmin(M(\mathbf{x})), \quad M(\mathbf{x}) \triangleq \frac{1}{2}\mathbf{F}(\mathbf{x})^T\mathbf{F}(\mathbf{x}) \\ &where \quad \mathbf{F}(\mathbf{x}) = [\mathbf{f}_1^T, \mathbf{f}_2^T, \ldots, \mathbf{f}_n^T]^T \in \mathbb{R}^{[6n\times 1]} \end{aligned} \tag{4.4}$$

We carried out a calibration experiment with $n = 150$ calibration poses. Solving Eq. (4.4) using iterative nonlinear least squares results in the following calibration vector (written in mm):

$$\begin{aligned} \mathbf{x} = [&-0.97, -0.66, -0.72, -0.86, -0.33, -0.56, 0.34, 0.31, \\ &0.46, -0.22, 0.32, 0.62, -0.38, 0.43, 0.27, 0.52, 0.55, 0.38]^T \end{aligned} \tag{4.5}$$

Here we derive the Jacobians used for solving the iterative nonlinear least squares problem. To use Newton's method for nonlinear least squares minimization, a Jacobian that relates M to $\mathbf{x}$ is derived from Eq.(4.4):

$$\mathbf{J}_M = \nabla_x M(\mathbf{x}) = \mathbf{F}(\mathbf{x})^T\mathbf{J}_F \in \mathbf{R}^{[1\times 18]} \tag{4.6}$$

where $\mathbf{J}_F$ is the Jacobian of $\mathbf{F}(\mathbf{x})$ with respect to $\mathbf{x}$. By differentiating Eq. (4.2), Jacobians of $f_{i,j}$ with respect to components of $\mathbf{x}_i$ are given by Eq.(4.7)-(4.9) where, $\mathbf{J}_1$ is the third column of ${}^b\mathbf{R}_{\mathbf{m}_j}$.

$$J_{ai,j} = \nabla_{a_i} f_{i,j} = \frac{{\mathbf{q}_{i,j}}^T\mathbf{J}_1}{\sqrt{{\mathbf{q}_{i,j}}^T\mathbf{q}_{i,j}}} \in \mathbf{R}^{[1\times 1]} \tag{4.7}$$

$$J_{bi,j} = \nabla_{b_i} f_{i,j} = \frac{{\mathbf{q}_{i,j}}^T[0,0,-1]^T}{\sqrt{{\mathbf{q}_{i,j}}^T\mathbf{q}_{i,j}}} \in \mathbf{R}^{[1\times 1]} \tag{4.8}$$

$$J_{q_{ei},j} = \nabla_{q_{ei}} f_{i,j} = -1 \in \mathbf{R}^{[1\times 1]} \tag{4.9}$$

Hence we obtain for i^{th} leg at j^{th} robot configuration:

$$\mathbf{J}_{i,j} = \nabla_{x_i} f_{i,j} = \begin{bmatrix} J_{ai,j} & J_{bi,j} & J_{q_{ei},j} \end{bmatrix} \in \mathbf{R}^{[1\times 3]} \tag{4.10}$$

For all 6 legs at the j^{th} configuration:

$$\mathbf{J}_j = \nabla_x \mathbf{f}_j = diag([\mathbf{J}_{1,j}, \ldots, \mathbf{J}_{6,j}]) \in \mathbf{R}^{[6\times 18]} \tag{4.11}$$

and the Jacobian for all 6 legs at all n calibration poses is:

$$\mathbf{J}_F = [\mathbf{J}_1^T, \ldots, \mathbf{J}_n^T]^T \in \mathbf{R}^{[6n\times 18]} \tag{4.12}$$

Thus the iterative Newton update for the calibration vector is given by Eq. (4.13) where $\mathbf{W} \in \mathbf{R}^{[18\times 18]}$ is a positive definite diagonal weight matrix.

$$\Delta\mathbf{x} = \mathbf{W}^{-1}\mathbf{J}_M{}^T(\mathbf{J}_M\mathbf{W}^{-1}\mathbf{J}_M{}^T)^{-1}(-M(\mathbf{x})) \tag{4.13}$$

4.1.2 Calibration Result

Before performing the parallel robot calibration, a simulation was coded to test the calibration algorithm. In simulation, the robot was initialized by perturbing the real calibration parameters and 300 poses were generated for calibration within the work space of $\pm 20mm$ in translation and $\pm 15^\circ$ in rotation in all directions. The calibration iteration was set to be 100 steps and the convergence ratio was set at $\alpha = 0.2$.

The calibration algorithm guides the perturbed parameter to its real value and converges the overall cost function to zero as shown in Figure 4.2(a). The calibration parameters also converge to the initial value before perturbing as shown in Figure 4.2(b). Figure 4.2(c) and (d) show the error on each leg throughout all calibration poses before and after calibration. We choose the error on each leg to plot because it holds the same meaning as the error in configurational space. Smaller joint space error means less task space end-effector error. From Figure 4.2(c) and (d), the leg error converge to almost zero after calibration. The whole calibration took 10 to 20 iterations to converge.

We also generate 300 poses for calibration on the real robot setup. The calibration

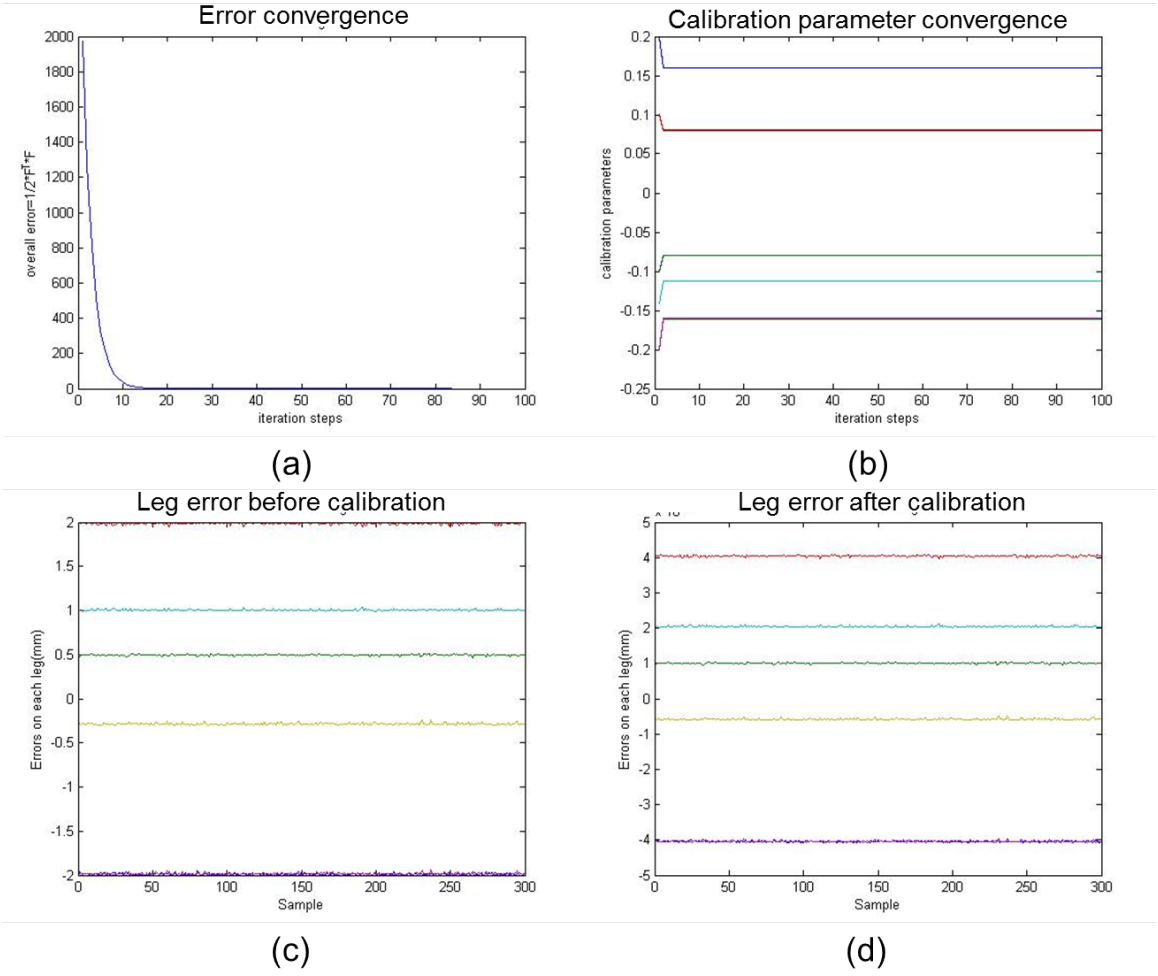

Figure 4.2: Parallel robot calibration simulation: (a) The convergence on the cost function; (b) The convergence on the calibration parameters; (c) and (d) Joint space leg error before and after calibration.

results are shown in Figure 4.3. The cost function shows a residual error in Figure 4.3(a) since there are residual error in joint space after the calibration as shown in Figure 4.3(c) and (d). From Figure 4.3(c) and (d), one could see the calibration brought the mean value of leg error back to zero without being able to reduce the standard deviation of the error. This is a result of solving the nonlinear problem using the recursive nonlinear least squares and also because our measurements had uncertainty of $\pm 0.25mm$ RMS.

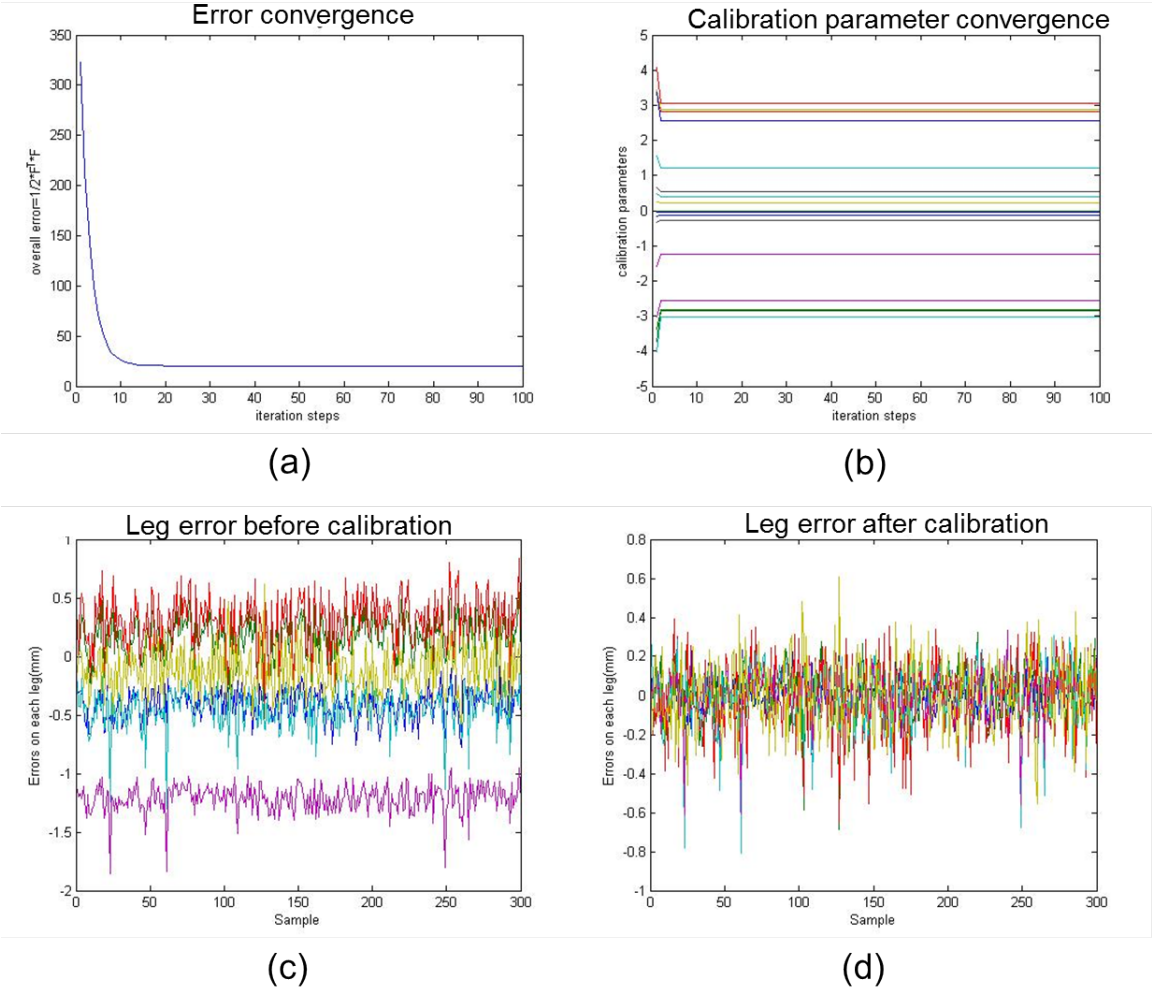

Figure 4.3: Parallel robot calibration on real robot: (a) The convergence on the cost function; (b) The convergence on the calibration parameters; (c) and (d) Joint space leg error before and after calibration.

4.2 Rapid Auto-calibration of Anatomy in Dual-arm Micro-vascular Surgery

Ophthalmic surgery requires sclera conformance with the constraints of the incision points. Traditionally, manually held surgical tools are operated similar to laparoscopic surgery with reversed intra-ocular motion. Previous works focus on regulating the robot intra-ocular movement by imposing remote center of motion (RCM) constraint which was enabled by mechanically fixed RCM point, force feedback or software-imposed RCM motion. Software-imposed RCM motion offers superior performance on allowing ocular motion. However on the other hand, it also requires robot calibration and relatively accurate knowledge of RCM point and eye dimension. This section presents a novel online calibration algorithm using small angular motion of eyeball from magnetic tracker as observation to quickly update these information both pre-operatively and intra-operatively.

A common thought of solving this problem is to use force sensor to detect the contact force between robot stem and sclera point. Using one commercially available force sensor on the robot and outside of the eyeball could help develop a force-based virtual fixture that regulates the intra-ocular motion. However, if the robotic stem makes contact with retina surface, the virtual fixture degrades since the force sensor could not isolate the force on two contact points. He, *et al.* [240] proposed a dual force sensing instrument based on fiber bragg grating (FBG) with the ability of sensing the force on both tool tip and the interaction force between the stem and the sclera. However, this instrument was paired with a mechanically imposed RCM robot (the Steady Hand Robot [106]) and in the ocular manipulation, the force sensing would not be able to provide a virtual fixture for constrained motion.

Angeles proposed the method of calculating the screw parameters of rigid body motion given three non-colinear points with finitely-separated positions [241] and infinitesimally-separated positions (linear velocity)[242]. We could potentially adopt this method by rotating the eyeball in multiple directions and find the screw axes of each rotation. The closest point to all the screw axes are the eyeball center of motion. However, Angeles's method did

not provide a way to calibrate the sclera incision points' position. In addition we needed a method that does not rely on large motion of the eyeball for safety. Angeles's method was also very sensitive to resolution and noise on position measurement. Hence we developed an efficient online calibration algorithm based on the assumption of a calibrated robotic system and the measurement of eyeball angular velocity. This algorithm would first calibrate the relative position of sclera incision point to the world frame and then calibrated the eyeball center of motion and radius. Simulation with and without noise in measurement were presented and calibration on phantom model was also carried out. We would also compare this algorithm to Angeles's method in finding the eyeball center of motion with the same sensing technology.

4.2.1 Method, Assumptions and Setup

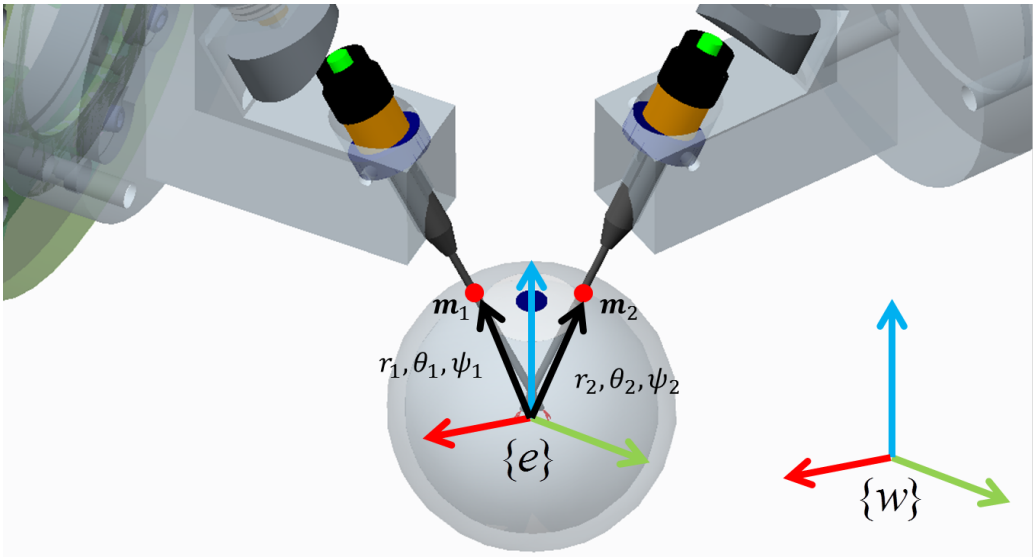

Figure 4.4: Mockup setup for rapid calibration algorithm nomenclature.

In this experiment, we keep only the 6 DOF Stewart-Gough platform for each robotic arm and attach a rigid stick to each arm to mimic an ophthalmic tool stem (Fig. 4.4). The stem inserted into the eyeball (or phantom model) through an ophthalmic trocar from the sclera incision point. The two sclera incision points were made according to the suggestion

from our ophthalmic collaborator. The eyeball in average was 25mm in diameter, and the iris was approximately 12mm in diameter. Both sclera incision points were cut 3mm from the edge of the iris and held an approximate angle separation of 120 degrees.

The calibration was based on three assumptions: both robot arms were calibrated with the attached tools; both robots were registered in the same known world coordinate $\{\mathrm{w}\}$ and all the corresponding frames including the eyeball frame $\{\mathrm{e}\}$ and the observer frame $\{\mathrm{ob}\}$ could be defined in this world coordinate; the eyeball was rigid enough to hold shape and small violation of sclera constraint would not tear the eyeball. The first assumption allowed us to define the incision points position on the robotic stem thus reducing the dimension of unknowns during part of the calibration process. And the calibration of this customized parallel robot has been presented in [228]. The second assumption required knowledge of the rigid attachment of both parallel robots to the base and the registration between the measurement tool and the base frame. During ophthalmic surgery, the surgeon needs to complete vitrectomy pre-operatively to remove the jelly-like substance filled inside the eye and then during the surgery, an irrigation tube injects liquid into the eyeball to maintain the inner pressure. Thus, the eyeball could hold a certain ocular shape during operation. On the other hand, the initial guess on calibration parameters would violate the sclera constraint. However, the eyeball is flexible, thus it could tolerate certain amount of tool tilting

The calibration required returning updated nine calibration parameters depicted in Figure 4.4.

1. The eyeball center of rotation (${}^{w}\mathbf{e} \in \mathbf{R}^{[3\times 1]}$). Here we only assumed the location of the origin of frame $\{\mathrm{e}\}$ as three unknowns and neglected the orientation part of frame $\{\mathrm{e}\}$ because we could assume, when we first inserted the robot stem into the eyeball, that the instantaneous eyeball frame $\{\mathrm{e}\}$ was parallel to the world frame $\{\mathrm{w}\}$, thus we had the ground truth to control the orientation of the eyeball.

2. The two radii from the origin of $\{\mathrm{e}\}$ to the two incision points ($r_i \in \mathbf{R}^{[1\times 1]}$ and $i = 1, 2$). Here we assume two different radii because the eyeball is only close to a sphere

shape.

3. Two incision points polar and azimuthal angles ($\theta_i \in \mathbf{R}^{[1\times1]}$ and $\psi_i \in \mathbf{R}^{[1\times1]}$ respectively, $i = 1,2$). These angles were defined in the eyeball frame $\{\mathrm{e}\}$.

Our algorithm relied on observing the eyeball motion according to the planned control input under an initial guess of the calibration parameters and converged to the true value of the calibration parameters. The algorithm used eyeball angular velocity ($\boldsymbol{\omega}_{eye}$) as the measurement. To be able to observe the eyeball angular velocity, we installed magnetic trackers coils (Ascension MEDSAFE 0.5mm) on the trocar. The algorithm contained two parts. The first part was called RCM point calibration in Section 4.2.2. In this part, we first inserted both robotic stems and made initial guess of incision points along the stem axis. Since the robot was already calibrated, the calibration parameter in this section was a one dimensional position information along the stem for each arm. The result of this section would return the scleral incision points position in the world frame. However we still could not determine any of the nine calibration parameters. So based on the known sclera incision points' position, we could perform a rapid hollow organ calibration in Section 4.2.3. In this section, by observing the reacting angular velocity of the eyeball and comparing it to the input commanded angular velocity, we could converge two rotation axes and found the eyeball center of rotation ${}^{w}\mathbf{e}$. Then with the known incision points in the world frame, the other calibration parameters could be calculated. Here we define several notations that remain constant through out this section. Without further notation, all the variables were defined in the world coordinate system $\{\mathrm{w}\}$ and thus we would neglect these superscripts. The subscript g means "guessed", u means "updated" and r means "real", which represent the initial calibration parameter, updated calibration parameter during recursive calculation and the true calibration parameter, respectively. The subscript i stands for the i^{th} robot stem and $i = 1,2$.

In Figure 4.5, a customized spherical joint was designed to mimic the eyeball motion. The inner ring was 25mm in diameter with two scleral incision holes of 1mm in diameter

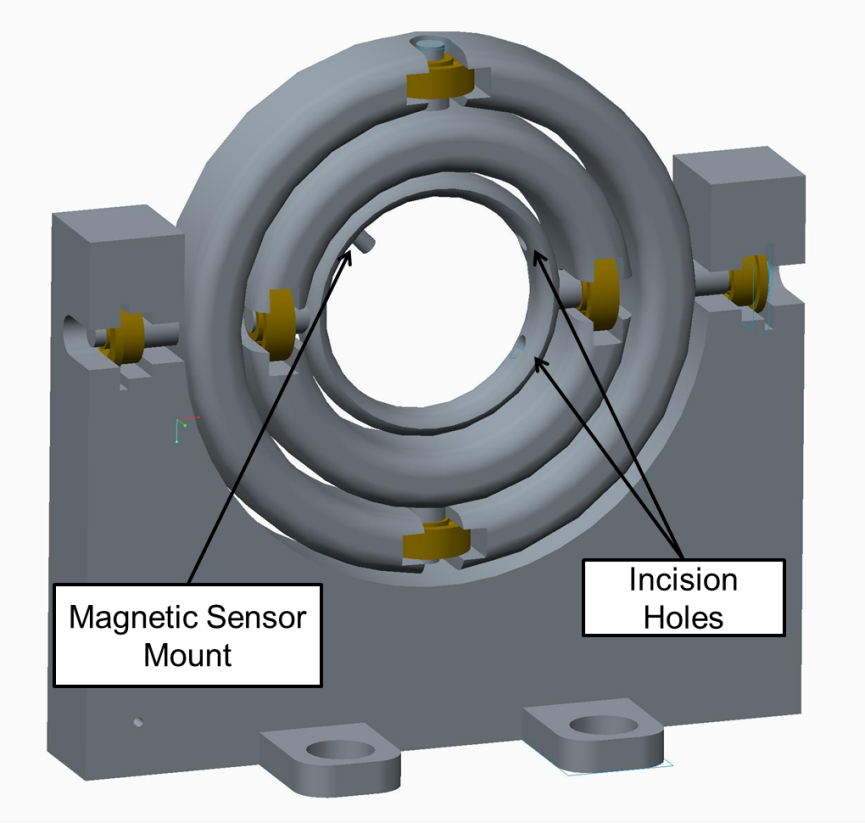

Figure 4.5: Customized spherical joint for mimicking the eyeball motion

and a mounting hole for a magnetic sensor. The setup of incision holes and magnetic sensor were slightly different from the real setup on the eyeball. The incision points were separated with 180° and the magnetic sensor was mounted at the anterior section of the eyeball, which was not ideal in real setup. However these minor changes on the artificial setup would not influence the evaluation of our calibration algorithm. In Figure 5.2(a), we inserted two robotic stems into the sclera holes and mounted two magnetic sensors. One magnetic sensor was mounted on the inner ring of the spherical joint and the other one on the base of the spherical joint. The magnetic sensor tracking has a much better resolution in orientation (0.5° or 0.0087 radians) than translation (1.4mm). The relative movement between the two magnetic sensors would provide the measurement for our calibration. Since the magnetic sensor was very fragile, we did not fix the position of the magnetic sensor. Thus the magnetic sensor could possibly translate along and rotate about its axial direction. In our proposed algorithm, we rely on the $\hat{\mathbf{z}}$ direction of the sensor to calculate the instantaneous angular velocity of the eyeball model.

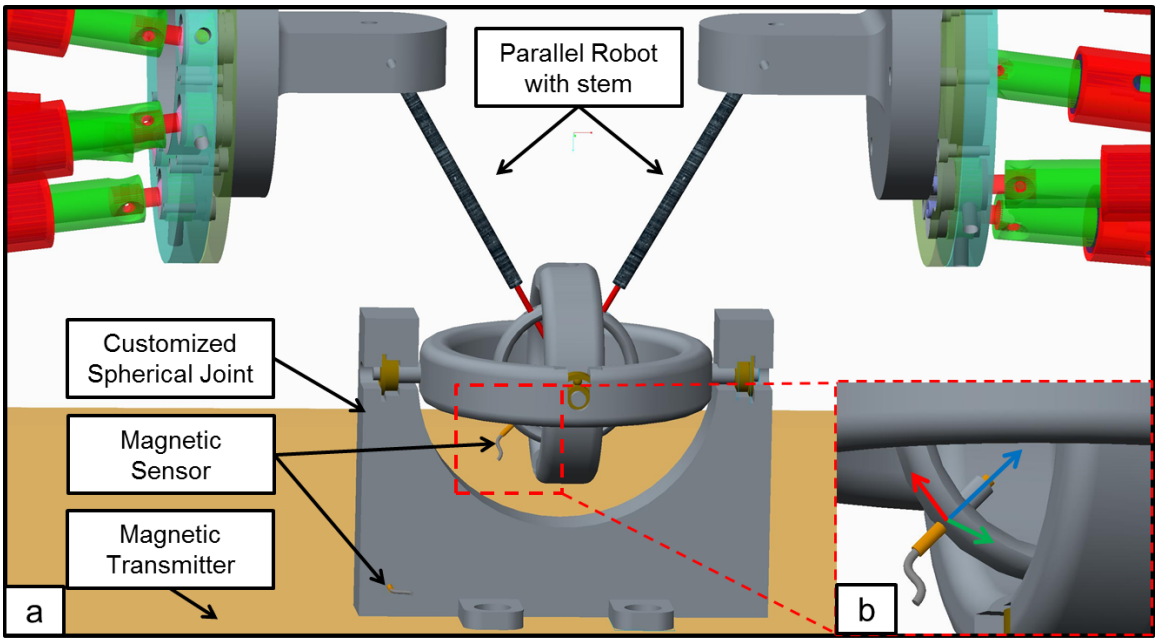

Figure 4.6: Experimental setup.

4.2.2 RCM Point Calibration

When the two robotic stems were first inserted into the eyeball, the only known information to the robot was that the incision points must sit on the robot stem axes. Thus, we only need to calibrate one unknown to acquire the sclera incision point's position in the world frame. During RCM point calibration, we hold one robot stem steady and calibrate the other stem's incision point by moving it under an initialized software programmed RCM control. This RCM control has been presented previously as constrained intra-ocular motion in [228]. If the guessed incision point's position is not accurate, when we move the second stick under the RCM constraint in a small motion, the eye ball will react in a slight angular velocity around the stable stick.

4.2.2.1 Calibration Algorithm for the Location of Incision Points

The RCM calibration algorithm nomenclature is defined as Fig.4.7. In this setup, we had two robot sticks $\overrightarrow{\mathbf{q}_i\mathbf{n}_i}$ that could manipulate the eyeball, where $\mathbf{q}_i$ and $\mathbf{n}_i$ were the start and end point of the stem. Each $\overrightarrow{\mathbf{q}_i\mathbf{n}_i}$ intersects the eyeball at the incision point $\mathbf{m}_{ir}$ on the eye ball. Here for instance, we calibrate the second arm's incision point $\mathbf{m}_{2r}$ by holding the first arm steady and moving the second arm under RCM control. There was a third trocar on the eyeball (green dot in Fig.4.7) for measuring the angular velocity of the eye ball. The known parameters in the calibration are $\mathbf{q}_i$, $\mathbf{n}_i$, the initial guess of the distance from the incision point $\mathbf{m}_{2g}$ to $\mathbf{q}_i$ on stick 2 and the angular velocity measured from the third trocar $\boldsymbol{\omega}_{eye}$.

Since the first stem is held steady, the incision point $\mathbf{m}_{1r}$ does not move, so any eyeball angular velocity must be along the axis $\overrightarrow{\mathbf{em}_{1r}}$. As shown in Fig.4.7, in the case of the guessed RCM point $\mathbf{m}_{2g}$ is inside the eye ball, if we move the second stick around $\mathbf{m}_{2g}$ in an angular velocity $\boldsymbol{\omega}_{RCM}$ along the z-axis of the world/eye coordinate (they were parallel by definition), a resulting eye angular velocity $\boldsymbol{\omega}_{eye}$ would point in the direction shown in Fig.4.7. On the other hand, if we have the guessed RCM point outside the eye ball, it would

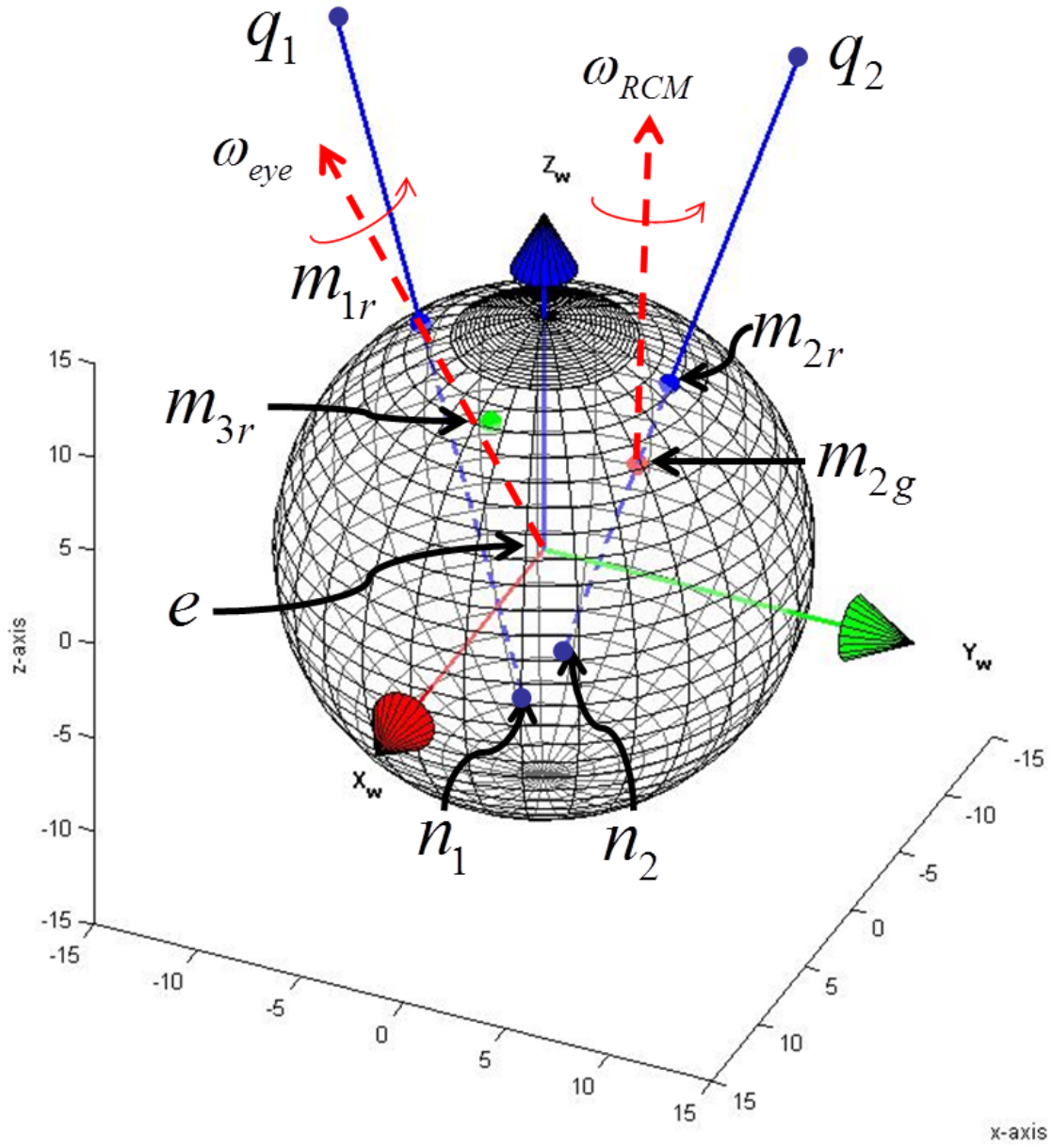

Figure 4.7: RCM calibration setup.

result in an eye angular velocity in the opposite direction. This meant we could utilize the dot product between $\boldsymbol{\omega}_{eye}$ and $\boldsymbol{\omega}_{RCM}$ to determine the direction of converging $\mathbf{m}_{2g}$ onto $\mathbf{m}_{2r}$. We defined the one dimension calibration parameter η_i to be the ratio between $\left\|\mathbf{m}_i - \mathbf{q}_i\right\|$ and $\left\|\mathbf{n}_i - \mathbf{q}_i\right\|$. Thus for the second stem, the ratio η_2 based on the guessed calibration distance is:

$$\eta_{2g} \triangleq \frac{\left\|\mathbf{m}_{2g} - \mathbf{q}_2\right\|}{\left\|\mathbf{n}_2 - \mathbf{q}_2\right\|} \tag{4.14}$$

Similarly, the ratio η_2 based on the calibration measurements is:

$$\eta_{2r} = \frac{\left\|\mathbf{m}_{2r} - \mathbf{q}_2\right\|}{\left\|\mathbf{n}_2 - \mathbf{q}_2\right\|} \tag{4.15}$$

The control law updates η_{2g} to converge to η_{2r} with the convergence criteria as the measured angular velocity $\boldsymbol{\omega}_{eye}$ converging to zero. The sign of the dot product between $\boldsymbol{\omega}_{eye}$ and $\boldsymbol{\omega}_{RCM}$ gave the converging direction and k is defined as a ratio that controls the convergence rate.

$$\eta_{2u} = \eta_{2g} - k\left\|\boldsymbol{\omega}_{eye}\right\| sgn(\boldsymbol{\omega}_{eye}^T \boldsymbol{\omega}_{RCM}) \tag{4.16}$$

The updated calibration parameter η_{2u} would converge to η_{2r} when the measured angular velocity $\boldsymbol{\omega}_{eye}$ converged to zero. Since there is noise from magnetic tracker measurement, we simulate this algorithm with noise level analysis.

4.2.2.2 Simulation and Sensitivity to Noise Analysis

The RCM calibration simulation presents the result of the calibration algorithm by perturbing the incision point with a distance ($\mathbf{m}_{2g}$) from the actual incision point ($\mathbf{m}_{2r}$). We built a model (Fig. 4.7) with real parameters for the simulation to run and gave the robot initial guessed parameters with 5% to 10% disturbance. Figure 4.8 showed the conver-

gence on the calibration parameters (η). Figure 4.8(a) were results without noise in the measurement, which showed perfect convergence. We chose the noise for the simulation as a random noise between $\pm 0.5 deg/s$ on the tracker attached to the trocar. The convergence criteria was based on relative convergence. The convergence criteria is shown in Eq. (4.17), where ratio δ is the parameter change between two iteration steps divided by the overall parameter change. Figure 4.8(b) also showed a bounded convergence with the noise.

$$\delta = \left| \frac{\eta_{cur} - \eta_{prev}}{\eta_{cur} - \eta_g} \right| \tag{4.17}$$

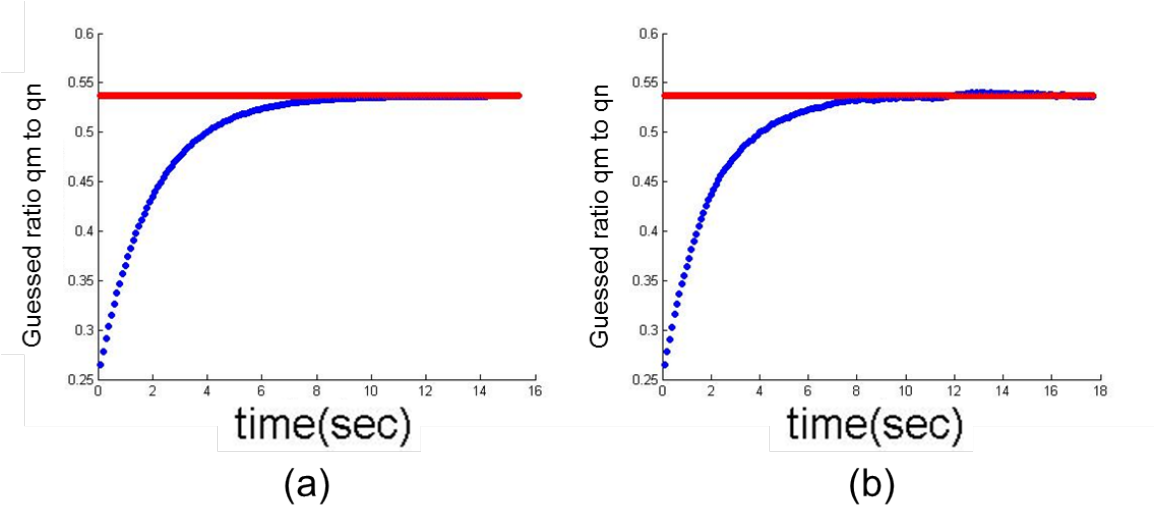

Figure 4.8: RCM calibration simulation result of (a) without (b) with noise.

4.2.2.3 Influence of Increased Noise Level to Simulation

The random noise level differs from the tracking system. Thus, we test the proposed algorithm with respect to increased noise level. This also tells us, with a certain type of sensor and a given resolution, how we can sample the measurement data to achieve a converged calibration result. With the increment of the noise level from $\pm 0.5 deg/s$ to $\pm 4.0 deg/s$, we find out that the simulation goes more and more unstable, which means the chance of failed convergence increases. To be able to achieve stabile simulation result,

we have to increase the relative convergence ratio δ (Eq. (4.17)), which will also increase the converged error between guessed and real calibration parameter. Figure 4.9 shows the distance error from converged to real RCM location with four different noise level. With the noise level above $\pm 4.0 deg/s$, it is hard to adjust δ to achieve a stable convergence and also a relatively small convergence error. $\pm 4.0 deg/s$ noise level also means, with the given magnetic tracker of $0.5 deg$ resolution in orientation, one can sample the measurement at most at 8Hz.

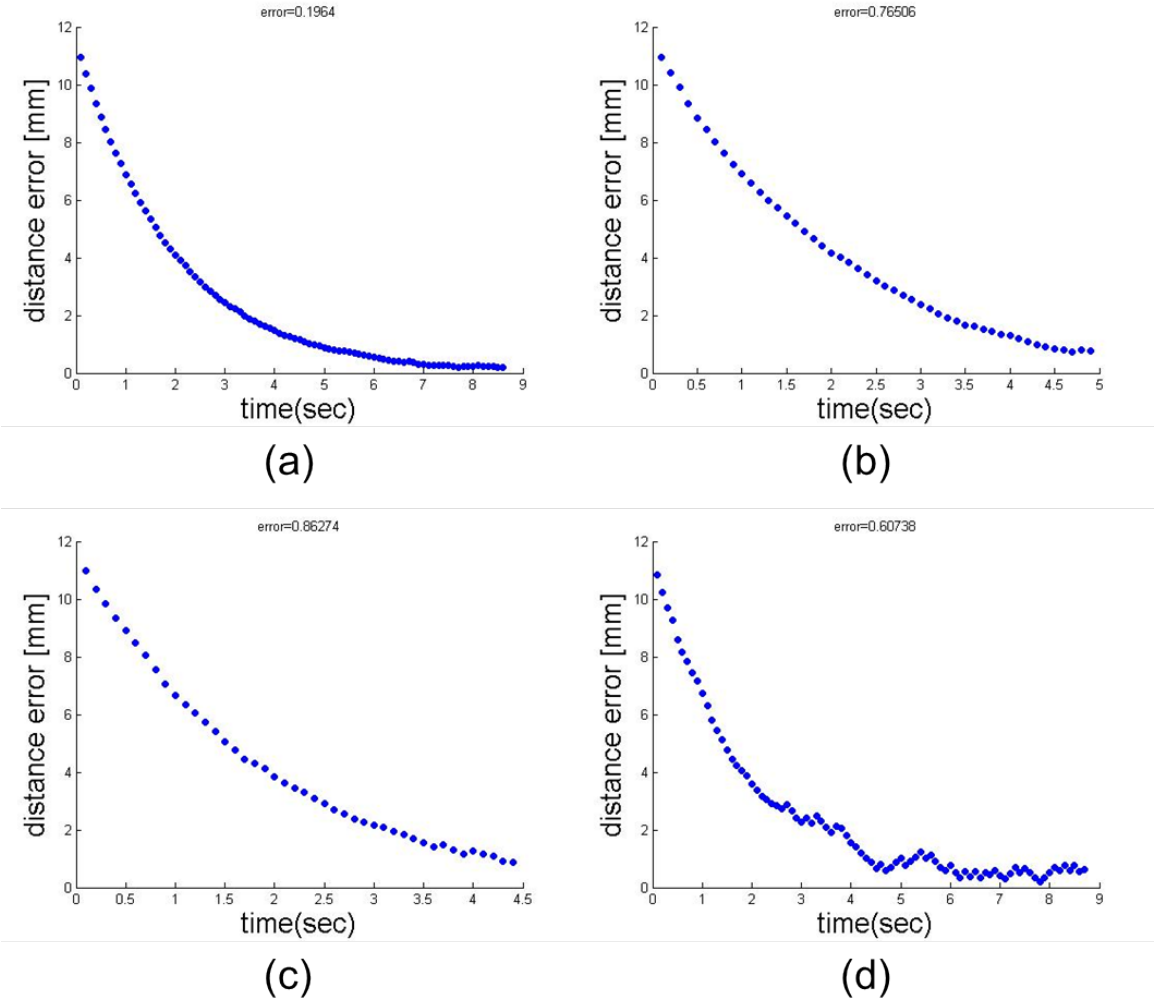

Figure 4.9: Convergence on the calibration parameter η with different noise level set. (a) $\pm 0.5 deg/s$ random noise with $\delta = 0.1\%$ (Eq. (4.17)); (b) $\pm 1.5 deg/s$ random noise with $\delta = 0.3\%$; (a) $\pm 2.5 deg/s$ random noise with $\delta = 0.6\%$; (a) $\pm 4.0 deg/s$ random noise with $\delta = 0.7\%$.

4.2.3 Rapid Hollow Organ Calibration

With the RCM point calibration (Section 4.2.2), we acquired the location of the sclera incision point in the world frame ($\mathbf{m}_{ir}$, $i = 1,2$). In this case, we could already perform safe intraocular manipulation. However, we still need to calibrate the eye parameters to perform ocular manipulation. The rapid hollow organ calibration would calibrate the initial guess of the hollow organ dimensions including the center of the eyeball, the radius at the incision points and the incision points' polar and azimuthal angles. The calibration was based on the existing results from RCM calibration. The idea was similar to calibrating the RCM point in world frame, with the difference on controlling the robot under ocular manipulation instead of intra-ocular manipulation. Similarly, we held one robot stem steady and controlled the other stem to rotate eyeball around the steady stem. From the previous section, we knew that any ocular motion generated with be along the axis pointing from the eyeball center to the incision point on the steady arm. Thus from the measured angular velocity we could locate the eyeball center on this axis. On the other hand, we switched the role of the steady and moving arm and locked the eyeball center on the other axis. Thus we could find the eyeball center of rotation by intersecting two axes. With known center of rotation and incision points defined both in world frame, we could calculate the radius, polar and azimuthal angles. The calibration nomenclature is shown in Figure 4.10, with similar notation defined previously. The only difference is that $\mathbf{m}_{ir}$ are known parameters as obtained from the previous section. Also, we would compare the simulation results to the ones using Angeles's method [241].

4.2.3.1 Proposed Algorithm

Similarly, we defined the initial guessed eye center as $\mathbf{e}_g$ and the real center as $\mathbf{e}_r$. The polar angles, azimuthal angles and radius were θ_i, ψ_i, and r_i, respectively. The cartesian to sphere coordinate system transformation would build the relationship between cartesian points $\mathbf{e}$, $\mathbf{m}_{ir}$ and θ_i, ψ_i, and r_i. Also, we made the assumption that when we first inserted

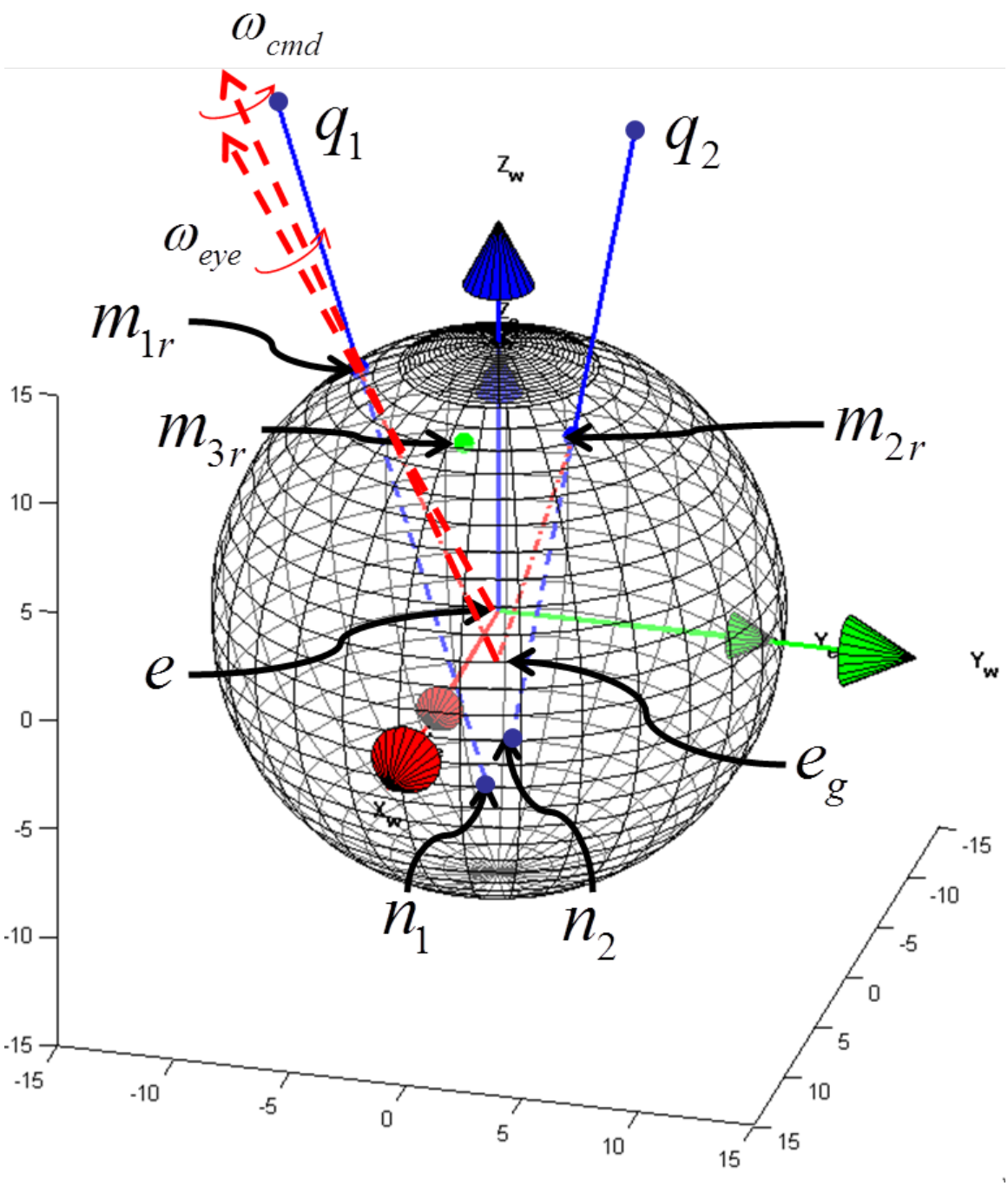

Figure 4.10: Rapid hollow organ calibration setup.

the robot stems, we defined the eye frame to be parallel to the world frame. This assumption was important that, once the robot stem starts to move, we lose the accurate measurement of the eye frame orientation. However, if we return both robot stems back to their initial configuration (”home”), the eye frame would be again parallel to the world frame. The sphere coordinate transformation were shown as the following and this equation was the same format for both guessed parameter and the real parameter.

$$ {}^{w}\overrightarrow{\mathbf{em}_{ir}} = {}^{e}\overrightarrow{\mathbf{em}_{ir}} = [r_i \sin\theta_i \cos\psi_i, r_i \sin\theta_i \sin\psi_i, r_i \cos\theta_i] \tag{4.18} $$

The estimated parameters are θ_{1g}, ψ_{1g}, r_{1g}, θ_{2g}, ψ_{2g}, and r_{2g} and the real parameters are θ_{1r}, ψ_{1r}, r_{1r}, θ_{2r}, ψ_{2r}, and r_{2r}. Here we first hold the first stick steady and tilt the second stick around the first stick. Since we know $\mathbf{m}_{1r}$ and $\mathbf{e}_g$, we generate an angular velocity along this axis to rotate the eyeball. The commanded angular velocity is designated by $\boldsymbol{\omega}_{cmd}$, with a known scalar k_g. k_g is the scaling factor between vector ${}^{w}\overrightarrow{\mathbf{e}_g\mathbf{m}_{1r}}$ and $\boldsymbol{\omega}_{cmd}$. The commanded angular velocity is a function of k_g, θ_{1g}, ψ_{1g}, and r_{1g}. However k_g and r_{1g} are always multiplied together, thus $\boldsymbol{\omega}_{cmd}$ is a function of three variables.

$$ \begin{aligned} \boldsymbol{\omega}_{cmd} &= k_g {}^{w}\overrightarrow{\mathbf{e}_g\mathbf{m}_{1r}} \\ &= k_g[r_{1g} \sin\theta_{1g} \cos\psi_{1g}, r_{1g} \sin\theta_{1g} \sin\psi_{1g}, r_{1g} \cos\theta_{1g}] \\ &= f(k_g r_{1g}, \theta_{1g}, \psi_{1g}) \end{aligned} \tag{4.19} $$

Similarly, because of the geometric constraint, the measured angular velocity $\boldsymbol{\omega}_{eye}$ also could be define in $f()$ function with the same format. And k_r was an unknown scalar.

$$ \begin{aligned} \boldsymbol{\omega}_{eye} &= k_r {}^{w}\overrightarrow{\mathbf{e}_r\mathbf{m}_{1r}} \\ &= k_r[r_{1r} \sin\theta_{1r} \cos\psi_{1r}, r_{1r} \sin\theta_{1r} \sin\psi_{1r}, r_{1r} \cos\theta_{1r}] \\ &= f(k_r r_{1r}, \theta_{1r}, \psi_{1r}) \end{aligned} \tag{4.20} $$

Hence, the function $f()$ contained three variables kr, θ and ψ. The Jacobian of this function was given by differentiating it with respect to each individual variable.

$$\mathbf{J} = \begin{bmatrix} kr\cos(\theta)\cos(\psi) & -kr\sin(\theta)\sin(\psi) & \sin(\theta)\cos(\psi) \\ kr\cos(\theta)\sin(\psi) & kr\sin(\theta)\cos(\psi) & \sin(\theta)\sin(\psi) \\ -kr\sin(\theta) & 0 & \cos(\theta) \end{bmatrix} \tag{4.21}$$

And the total differential of $f()$ is given by:

$$\delta\boldsymbol{\omega} = \mathbf{J} \begin{bmatrix} \delta\theta \\ \delta\psi \\ \delta(kr) \end{bmatrix} \tag{4.22}$$

Here $\delta\boldsymbol{\omega} = \boldsymbol{\omega}_{eye} - \boldsymbol{\omega}_{cmd}$ was the difference between commanded and measured angular velocity. So the solution to the updated calibration parameters could be given through recursive least squares:

$$\begin{bmatrix} \delta\theta \\ \delta\psi \\ \delta(kr) \end{bmatrix} = \mathbf{J}^{-1}\delta\boldsymbol{\omega} \tag{4.23}$$

$$\begin{bmatrix} \theta_{1u} \\ \psi_{1u} \\ kr_{1u} \end{bmatrix} = \begin{bmatrix} \theta_{1g} \\ \psi_{1g} \\ kr_{1g} \end{bmatrix} + \alpha \begin{bmatrix} \delta\theta \\ \delta\psi \\ \delta(kr) \end{bmatrix} \tag{4.24}$$

where α controls the step size. Hence, we get the converged θ_{1r} and ψ_{1r}. The radius r_{1r} was not calibrated from this first step because it was multiplied with a scalar k. The physical meaning of this was that rotating the eyeball around only the first stem would only help us locate the eyeball center on the axis passing through $\mathbf{m}_{1r}$ and along the direction specified by θ_{1r} and ψ_{1r}. And where exactly along this axis could not be calibrated, which was determined by r_{1r}. This also meant we could update our initial guess of eye center $\mathbf{e}_g$

to be on this axis with the distance r_{1g} from $\mathbf{m}_{1r}$. We then repeat the same operation by holding the the second arm steady and controlling the first stem to rotate the eyeball around the axis pointing from the updated $\mathbf{e}_g$ to $\mathbf{m}_{2r}$. Before this operation, both robot stems are returned to "home" configuration to make sure frame $\{\mathrm{e}\}$ aligned with frame $\{\mathrm{w}\}$. After repeating the calibration algorithm, we solve for θ_{2r} and ψ_{2r}.

Again, we returned all the robot stems back to "home" to bring frame $\{\mathrm{e}\}$ parallel to frame $\{\mathrm{w}\}$. We obtain the following equations with the spherical coordinate transformation on real parameters.

$$
\begin{aligned}
&{}^{e}\overrightarrow{\mathbf{e}_r\mathbf{m}_{ir}} = [r_i \sin\theta_i \cos\psi_i, r_i \sin\theta_i \sin\psi_i, r_i \cos\theta_i] \\
&{}^{e}\overrightarrow{\mathbf{e}_r\mathbf{m}_{ir}} = {}^{w}\overrightarrow{\mathbf{em}_{ir}} = \mathbf{m}_{ir} - \mathbf{e}_r \\
&\mathbf{m}_{ir} - \mathbf{e}_r = [r_{ir} \sin\theta_{ir} \cos\psi_{ir}, r_{ir} \sin\theta_{ir} \sin\psi_{ir}, r_{ir} \cos\theta_{ir}]
\end{aligned}
\tag{4.25}
$$

The radius r_{ir} and eyeball position ${}^{w}\mathbf{e}_r$ could be calculated from solving Eq. (4.25).

4.2.3.2 Simulation Study

We carried out the rapid calibration simulation by perturbing the calibration parameters such as eye center, the θ and ψ angles of each incision point. The simulation was similar to the ones in RCM point calibration. Without the noise, the simulation converged as shown in Fig. 4.11 with (a) to (d) representing θ_1, ψ_1, θ_2 and ψ_2 respectively. When a random noise was introduced in the simulation ($\pm 0.5 deg/s$), the simulation result is shown in Fig. 4.12 with a bounded convergence on all angles. Figure 4.13 shows the convergence of distance error between the calibrated center and the real center of the eyeball with respect to time. The first convergence occurs when rotating the eyeball around the fixed first stem, which corresponds to the convergence of θ_1 and ψ_1. And the second convergence corresponds to the convergence of θ_2 and ψ_2. This simulation was repeated ten times with the same setting of noise level. The converged distance error on eyeball center had a mean value of 0.1065mm and standard deviation of 0.0553mm.

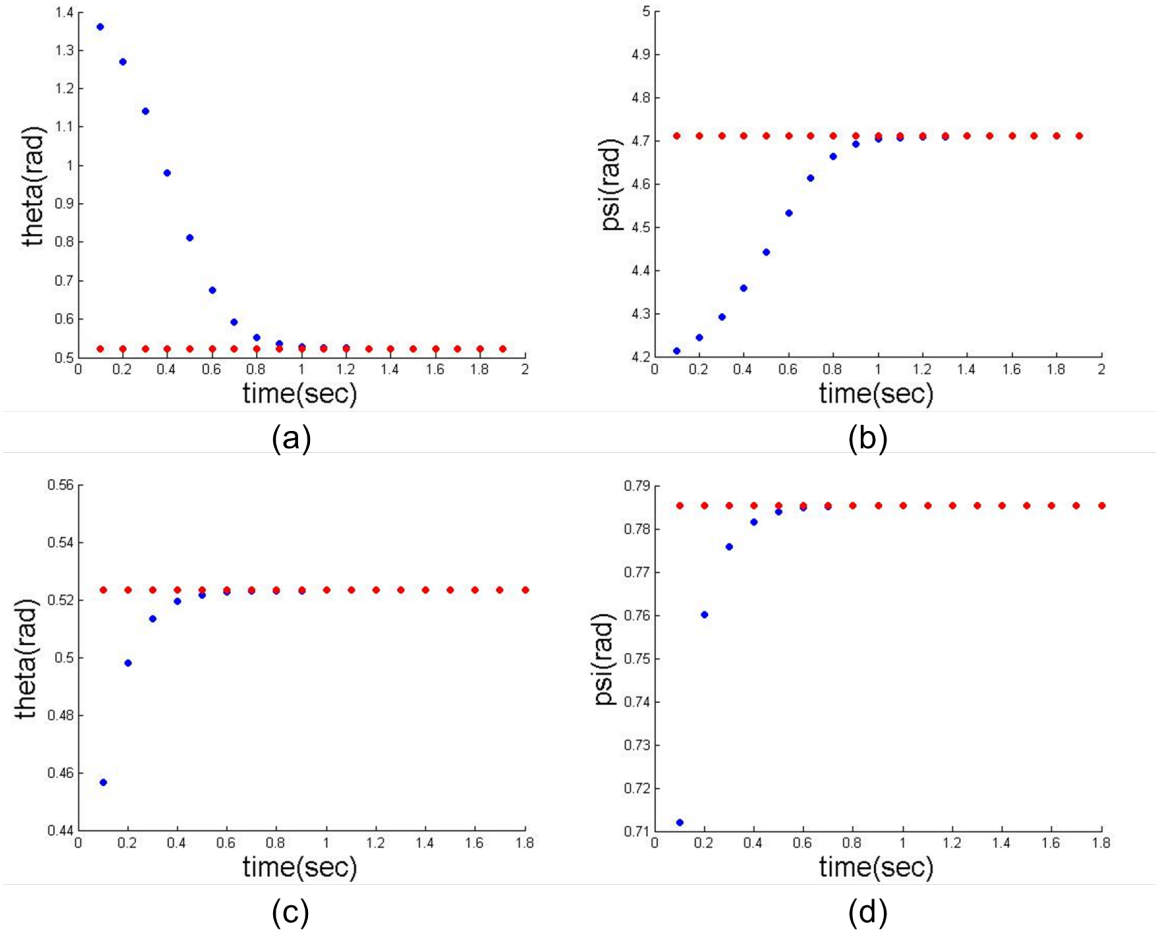

Figure 4.11: Simulation result of the rapid hollow organ calibration without noise.

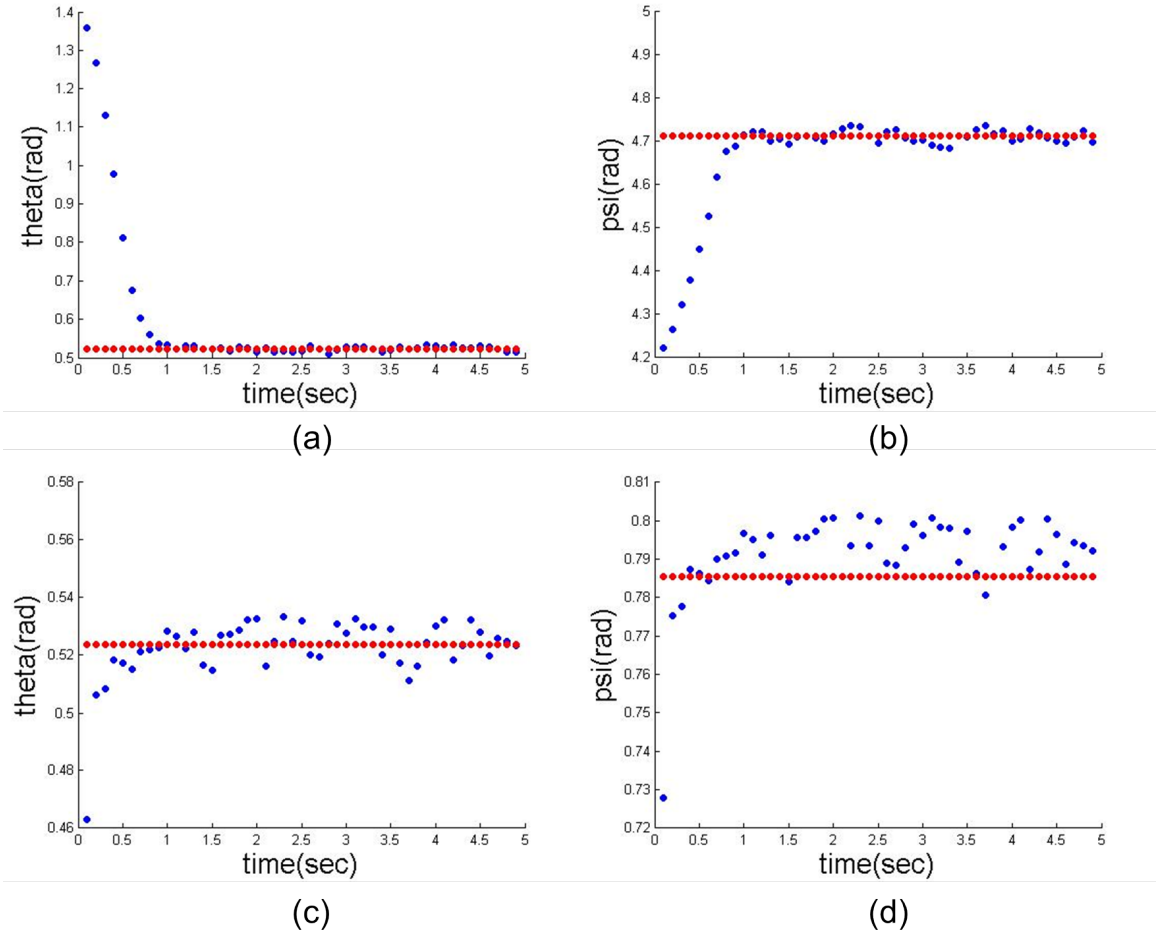

Figure 4.12: Simulation result of rapid hollow organ calibration with noise.

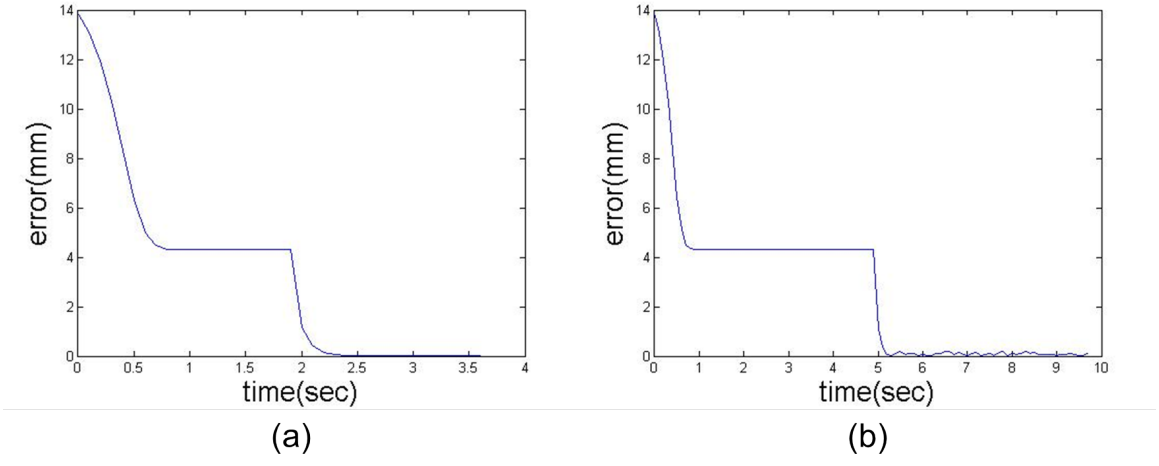

Figure 4.13: Convergence on the distance between the guessed and the real eyeball center.

We also compared the results of our method with the method relying on estimating the screw axis for finitely separated motions. The measurement was provided by the translational part of the magnetic tracker and the resolution was $1.4mm$. If the simulation was given perfect measurement, the Angeles's method could locate the center of rotation perfectly. With a disturbance to the position measurement with random noise between $\pm 1.4mm$, the simulation showed that Angeles's method failed to calibrate the center of rotation with a big error on converged eyeball center. Angeles's method was not only sensitive to noise from measurement, but also not suitable for our specific case since magnetic tracker had bad performance on translational measurement.

4.3 OCT Image Calibration

The goal of the OCT image calibration is to find the dewarping function that converts the warped OCT image frame $\{$u,v$\}$ to unwarped world frame $\{$x,y$\}$. The result of OCT image calibration will give us lateral and depth dewarping function $x = S_x(u,v)$ and $y = S_y(u,v)$ which calculate the real position (x,y) in world frame for any given pixel point (u,v) in the OCT image frame. Applying these two dewarping function on any real-time OCT image will give us an uniformly scaled OCT image. It will also improve the robustness of visual servoing algorithm from a perspective of safety and we can increase the maximum tool tip velocity to a safe value that does not exceed the measure distance in mm from the image. Other useful results from this application include: 1) we can measure the size of blood vessels, cross section area during surgery, which can provide the guideline of which tool we should use for specific surgery; 2) Ratio of diameter to wall thickness of vein can be measured from the uniform image so as to indicate the vein health. Thin plate splines (TPS) method has been used for ultrasound image dewarping and a detailed review about related work has been summarized in Chapter 1. To the best of our knowledge, this is the first work to adapt TPS to OCT calibration.

4.3.1 Calibration Grid and Calibration Algorithm

In this section, we are aiming to dewarp the distortion of any given B-mode OCT probe with unknown intrinsic parameters. This means the only measurement we have is the B-scan OCT image itself. To calibrate our customized B-scan OCT probe, we created the calibration pattern with known dimension in the world frame {x,y} and compare it to the corresponding dimension in OCT image frame {u,v} to create a mapping between two frames. The calibration algorithm is based on thin-plate spline interpolation and will be discussed in detail in 4.3.2. The experimental setup for calibration pattern creation is shown in Fig. 4.14(a). The B-scan OCT is used to view an EM grid (Fig. 4.15(c)) at different height. The EM grid has the center of each line separated by $127\mu m$ and is viewed by the scanning probe with the grid's line direction perpendicular to the probe's scanning direction. The scanning pattern will be moved from up to down in a separation of $100\mu m$ with respect to the scanning probe to create a full calibration pattern in both lateral and depth direction.

Figure 4.15(d) shows the actual experimental setup for acquiring the calibration pattern. The OCT probe was held by a rotary stage (Newport ®, M-481-A, Rotation Stage, 360°*Coarse*, 5° Fine, Micrometer, Metric) and the whole assembly was fixed onto micrometer XYZ stage (Newport Corp.). The rotary stage allows us to adjust the scanning direction to be perpendicular to the gird lines. The X and Y adjustment on the XYZ stage allows us to adjust the focus point of the probe to see as many grid points as we could. Once everything was adjusted well, we lock the rotary stage and the XY direction. We then move the probe from low to high with a separation of $100\mu m$ (relatively, the grid was moving from up to down with respect to the OCT probe) to create a full pattern.

Figure 4.15 shows the OCT image of the EM grid at $400\mu m$ from the top. The material of the EM grid is copper. When the OCT probe is used to view metal material like the grid lines, only the highest point of each line will have the reflection and this reflect will create a bright scattered line in lateral direction as shown in Fig. 4.15. The horizontal lines in this

figure resulted from the strong reflection of the copper surface. 17 different OCT images of the EM grid were taken, which gave us a full range of the OCT probe's depth penetration of 1.6mm. As the probe moves further from the grid plate, more grid points start to show up because the scanning range increases. Post image segmentation on these figures will help us find the center of these white dots and create a full pattern on OCT image frame {u,v}. Figure 4.14(b) shows all the grid points at different height in one image. The 17 images were processed after median filter and gray-to-black-white filter. The center of each grid point was plotted in red dots and points from the same height was connected with a read line. There are a total number of 119 points on this image.

Figure 4.16(a) shows all the grid points in the OCT image frame {u,v} with a 640 by 480 drawing canvas. Fig. 4.16(b) shows the corresponding points in blue dots with a 640 by 480 drawing canvas. Each blue dot on the same line is separated by 63.5 pixels and between different height the distance is 50 pixels. This ratio corresponds with the actual dimension in the calibration pattern of $127\mu m$ separation in lateral direction and $100\mu m$ separation in depth direction. Each point in OCT image frame is written as $P_i = (u_i, v_i)$ and each point in the world frame is $Q_i = (x_i, y_i)$. A mapping function that transfers all the control points P_i to Q_i will be the dewarping function for this particular OCT probe. This function will have two parts as following:

$$x = S_x(u, v) \tag{4.26}$$

$$y = S_y(u, v) \tag{4.27}$$

4.3.2 OCT Image Dewarping Based on Thin-plate Spline Interpolation

To find the dewarping function that transfers OCT image point P_i to its corresponding point Q_i in world frame, we choose to use the thin-plate spline interpolation method. Since the grid's absolute position is unknown, we need to choose an origin point to expand the

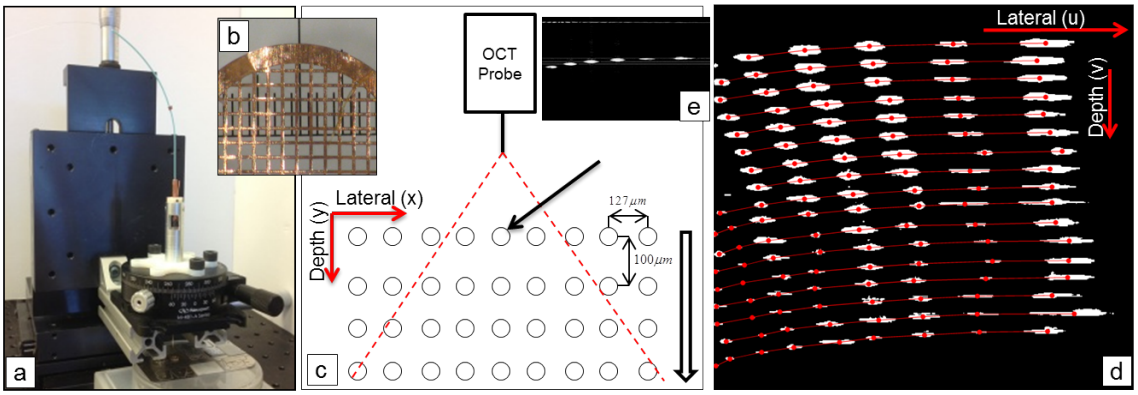

Figure 4.14: Conceptual setup for OCT image calibration with the calibration pattern. (a) Calibration pattern creation, the EM grid has a known dimension and is moved from up to down in a known step. (b) OCT image of all the calibration patterns at different height in one image. The image was processed with a median filter and a gray to black-white filter. Red dots represents the center of each white point cloud. The red line denotes that the points are at the same height in world frame $\{x,y\}$. (c) The EM grid under the micro scope. (d) Experimental setup for the calibration pattern creation with XYZ stage and rotary stage.

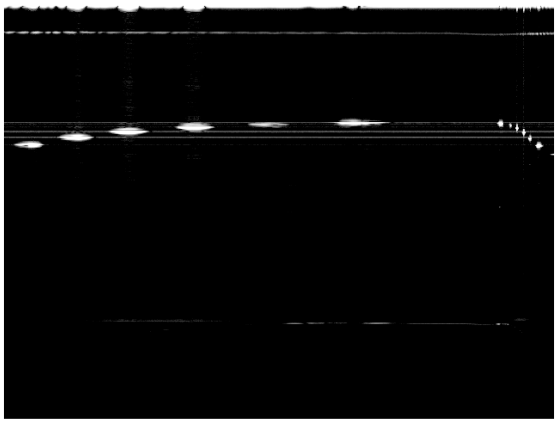

Figure 4.15: OCT picture of the EM grid at a certain height.

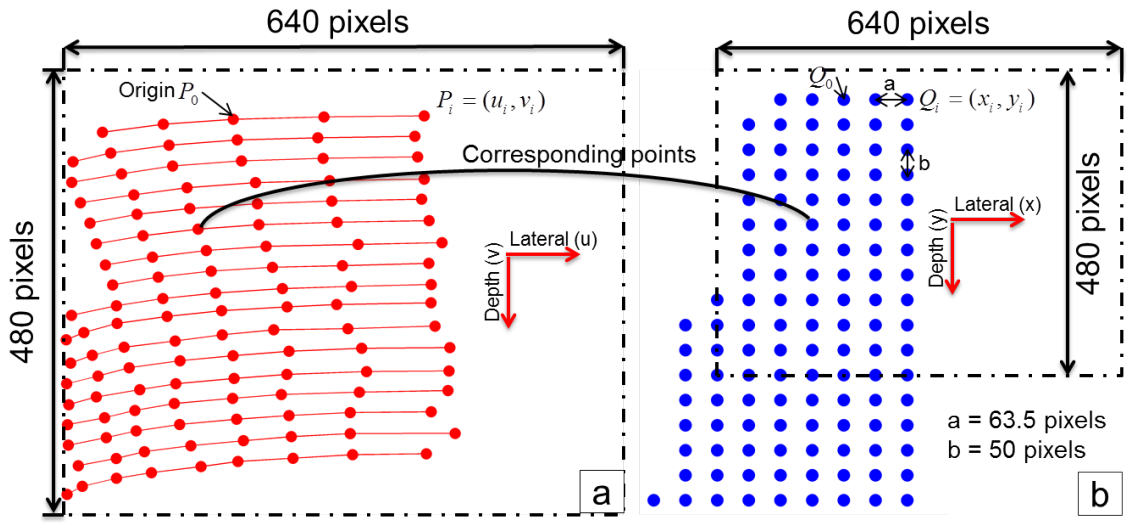

Figure 4.16: Grid pattern in both OCT image frame and world frame with a total number of 119 sample points. (a) Grid points in the OCT image frame. Each line is separated by 100 μm and each point on the line is separated by 127 μm (b) Grid points in the world frame.

grid pattern and register the grid points in two frames together. The center point of the first line is chosen as the origin $P_0 = (u_0, v_0)$ as shown in Fig. 4.16(a). So the grid points' position $Q_i = (x_i, y_i)$ in world frame is given by adding the separation of 63.5 pixels in lateral direction and 50 pixels in depth direction onto the origin position $Q_0 = P_0$.

Hence we created a set of $n = 119$ control points for thin-plate spline interpolation. Here we take the mapping function in lateral direction $x = S_x(u, v)$ as an example. From the control points, we know in ideal situation $x_i = S_x(u_i, v_i)$. Thin-plate spline interpolation gives us the function S_x in the form like this:

$$S_x(u,v) = a_1 + a_2 u + a_3 v + \sum_{i=1}^{n} w_i T(|P_i - (u,v)|) \tag{4.28}$$

$P_i\,(i = 1 \cdots n)$ are the control points from the OCT image frame. $a_1 + a_2 u + a_3 v$ defines a flat plane that best matches all control points. The last term corresponds to the bending forces provided by all the control points. This part of the function is determined by a coefficient w_i for each control point and a function $T(r) = r^2 log(r^2)$. $|P_i - (u,v)|$ is the distance from any point in the OCT image frame to the i^{th} control point. The remaining unknowns in

this function are the coefficients w_i and $a_1 \sim a_3$. Hence we define the coefficient matrix $C = [w_1 \cdots w_n, a_1, a_2, a_3] \in \mathbf{R}^{[1\times(n+3)]}$. From [243], we know that the coefficient matrix C is calculated as following:

$$C^T = L^{-1}Y, \in \mathbf{R}^{[(n+3)\times 1]} \tag{4.29}$$

$Y = [x_1, x_2, \cdots, x_n, 0, 0, 0]^T, \in \mathbf{R}^{[(n+3)\times 1]}$ are the control points' height, which are the corresponding control points' lateral position in the world frame.

$P \triangleq \begin{bmatrix} 1 & x_1 & y_1 \\ 1 & x_2 & y_2 \\ \cdots & & \\ 1 & x_n & y_n \end{bmatrix}, \in \mathbf{R}^{[n\times 3]}$ are the control points' position in the OCT image frame.

Let's define $r_{i,j} \triangleq |P_i - P_j|$ as the distance between i^{th} and j^{th} control points.

Matrix $K \triangleq \begin{bmatrix} U(r_{11}) & U(r_{12}) & \cdots \\ U(r_{21}) & U(r_{22}) & \cdots \\ \cdots & \cdots & U(r_{nn}) \end{bmatrix}, \in \mathbf{R}^{[n\times n]}$. The matrix L in Eq. 4.29 is given by:

$$L = \begin{bmatrix} K & P \\ P^T & 0 \end{bmatrix}, \in \mathbf{R}^{[(n+3)\times(n+3)]} \tag{4.30}$$

From Eq. 4.29 to 4.30, we could calculate the coefficient $C = [w_1 \cdots w_n, a_1, a_2, a_3] \in \mathbf{R}^{[1\times(n+3)]}$ and acquire the function $x = S_x(u,v)$. Similarly, we also acquired the function for depth direction $y = S_y(u,v)$. All the control points and the resulting thin-plate spline interpolation plane are plotted in Fig. 4.17.

To verify the accuracy of this fitting plane, we applied the dewarping function onto the grid points in OCT image frame (red star points in Fig. 4.18(a)) and got the resulting points in world frame (blue circle points in Fig. 4.18(a)). By comparing these blue circle points in Fig. 4.18(a) to the blue points in Fig. 4.16(b), we could find the error of each point by calculating the distance of the corresponding points. The error shows a mean value of 2.6107e-10 pixels and standard deviation of 1.5846e-10 pixels. We also applied

the dewarping function onto the OCT image shown in Fig. 4.15 and the result is shown in Fig. 4.18(b). We could see that all the grid points were moved back onto the same level and had the same separation distance from each other. Since the material is copper, the original picture in Fig. 4.15 views the grid points as scattered lines in lateral direction, the resulting figure shows the grid points in a huge dot. Also because of the reflection, we have the bent lines in the dewarped image. We also applied this dewarping function onto an OCT image of the infra-red reflection paper. The result is shown in Fig. 4.19.

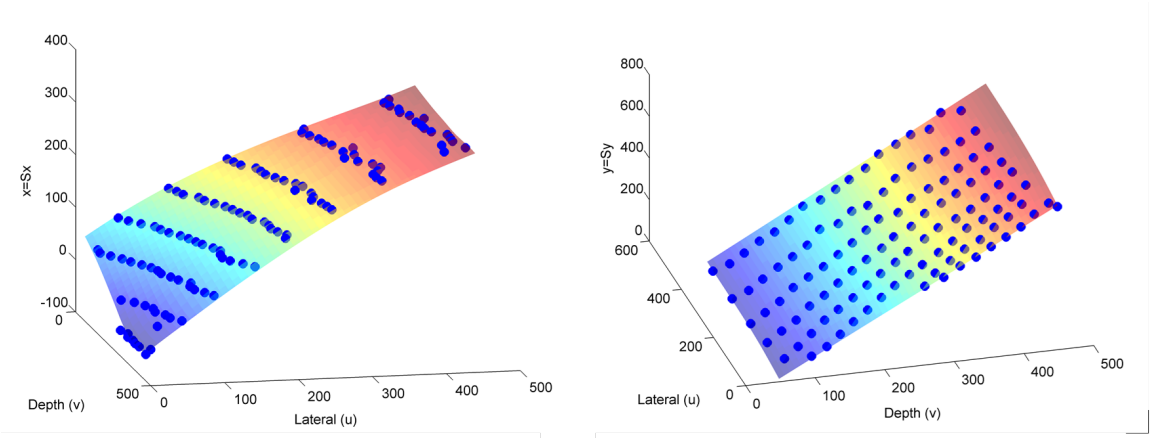

Figure 4.17: Thin-plate Spline Interpolation result. (a) S_x. (b) S_y

4.4 OCT Probe to Robot Registration

4.4.1 Calibration of Scanning Plane in OCT Base Frame

4.4.1.1 Calibration Algorithm

Figure 4.21(a) shows a conceptual representation of the calibration phantom and calibration setup. The calibration phantom consists of three copper wires embedded in a planar matrix with accurately manufactured groves with a known opening angle 2α. The calibration setup is shown in Fig. 4.21(b). The red lines are the embedded copper wires with angle α fabricated to 7.5°. The green line represents the scanning direction of the OCT

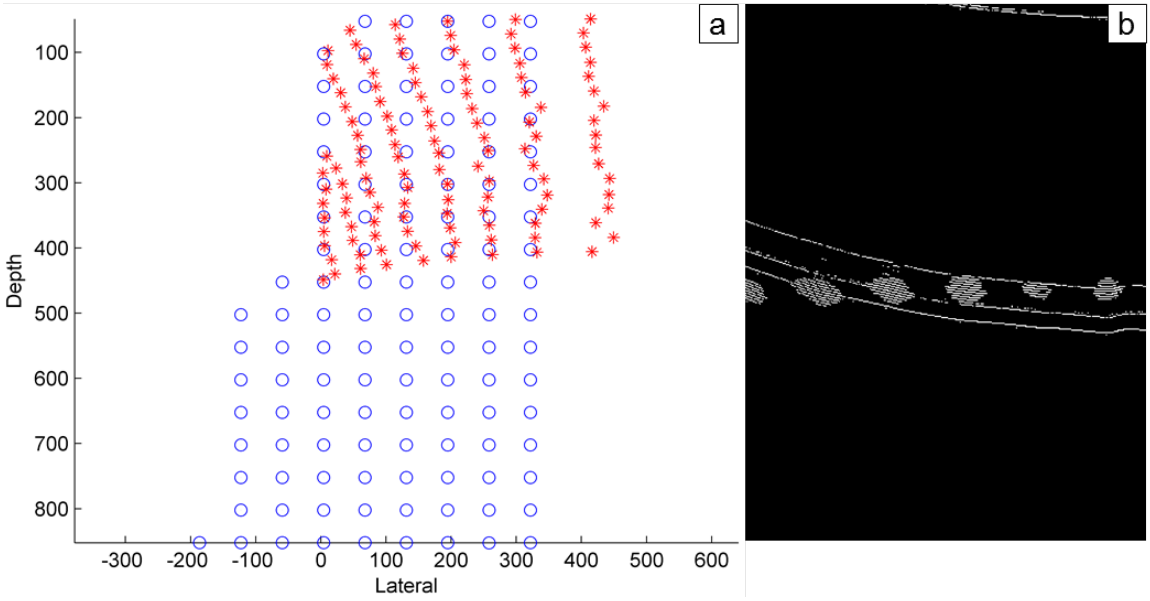

Figure 4.18: Dewarping result using the thin-plate spline interpolation. (a) Apply the transform function onto the grid points in red star and acquire the distorted points in blue circle. (b) Apply the dewarping function onto Fig. 4.15.

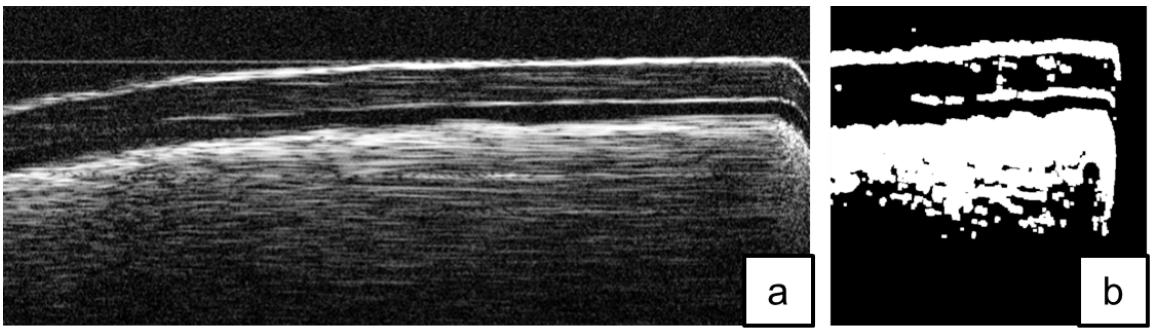

Figure 4.19: OCT image of the infra-red reflection paper before and after dewarping.

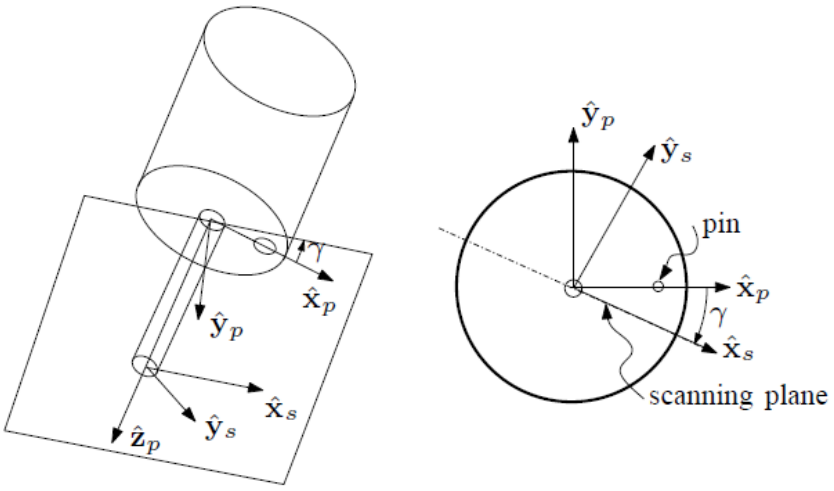

Figure 4.20: Top view of the probe showing the scanning plane and the probe frame

probe. The scanning line makes three intersection point with the copper wires as black dots in the figure and it was separated to be two different segments y_1 and y_2. The basic concept behind the calibration procedure is that the angle of the OCT scanning plane with respect to each tube determines length of y_1 and y_2 in Fig. 4.21(b). If the OCT probe has a perfectly calibrated lateral and depth scales from the OCT Image Calibration, then y_1 and y_2 should have the same length when the scanning plane is perpendicular to the tube. With this approach we assume that the lateral scaling as a function of the image coordinates has been characterized as described in OCT Image Calibration. The OCT probe scanning plane is determined by the intrinsic parameters of the OCT probe, which in turn are dependent on specific fabrication parameters. Figure 4.20 illustrates the OCT probe and its scanning plane. This plane is determined by intrinsic and specific fabrication parameters. Knowing the accurate angle (γ) of the scanning plane defines the transformation between frames $\{\mathrm{s}\}$ and $\{\mathrm{p}\}$.

Angle θ in Fig. 4.20 designates the probe tilting from the normal direction, which is the angle between retina surface normal direction and the axis $\mathbf{z}_s$. It is not crucial to find the accurate θ value since in 4.4.2, θ is an automatic result. However, changing angle θ

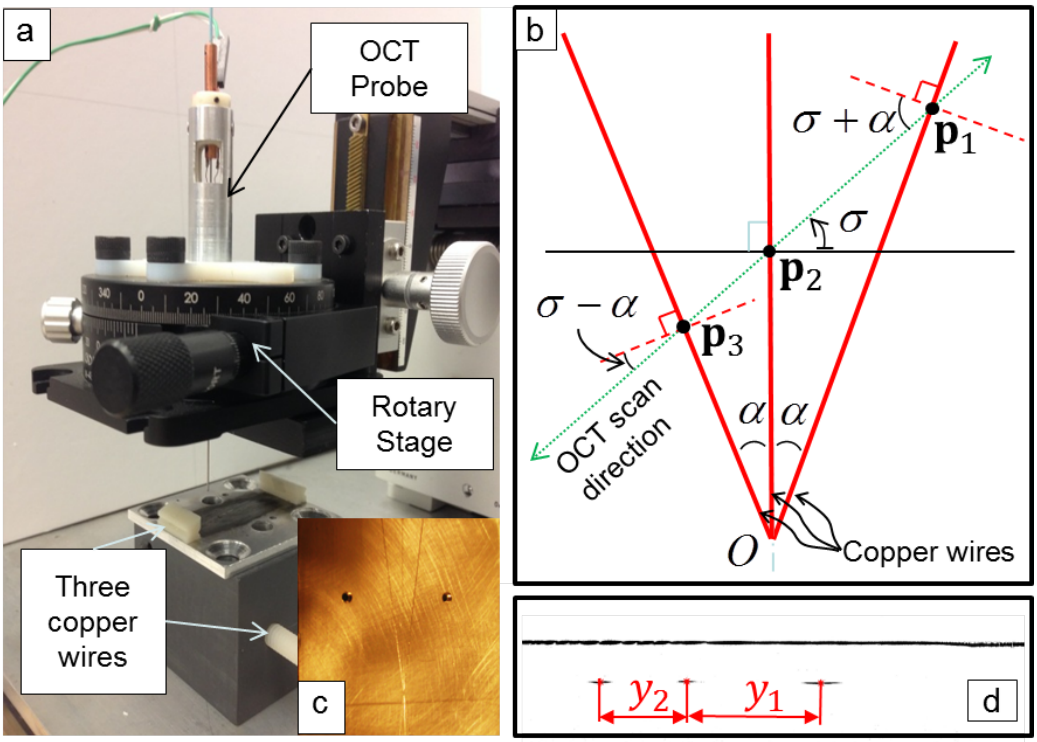

Figure 4.21: (a) OCT probe manual calibration setup; (b) Manual Calibration schematic.

will result in different image qualities. We tested the OCT probe image quality with respect to the angle θ in [229]. The result shows that when θ exceeds 30° from the object normal direction, the image will become blurred.

The scanning plane calibration schematic is shown in Fig. 4.21(b). Three red solid lines are copper wires separated by 2α angle. The green solid line is the probe scanning direction, which is the intersection line of the scanning plane and the object surface plane. The black solid line is perpendicular to the bisector line and represents the optimal scanning direction. Angle σ is the tilting angle of scanning direction from the optimal direction. On the dewarped OCT image, the three copper wires will have the separation y_1 and y_2. We define the manual calibration success metric as $f = y_1/y_2$, where f is the ratio between the two distances. $f = 1$ designate a successful calibration. σ and α are two variables in this calibration.

The experiment to calibrate the OCT probe's scanning plane was carried out as the setup

in Fig. 4.21. The OCT probe was fixed onto a rotary stage to allow us to change the angle σ. The whole assembly was mounted on an XYZ stage. We had a rough estimation of the scanning plane's direction and continuously rotated the OCT probe from $\sigma = -45°$ to $\sigma = 45°$. The OCT image of the three copper wires is shown as Fig. 4.22(a). The position of the points were distorted and we shall apply the dewarping function S_x from the OCT Image Calibration to dewarp the image. After dewarping, we calculated $f = y_1/y_2$ based on the undistorted data and plotted out $f = y_1/y_2$ with respect to time in Fig. 4.22(b). The noise in this figure is a result from the noise in the OCT stream. When the scanning plane is perpendicular to the bisector line of the 2α angle, we will have $f = 1$ from the figure. This ratio will be displayed in real-time with the OCT image while performing the calibration.

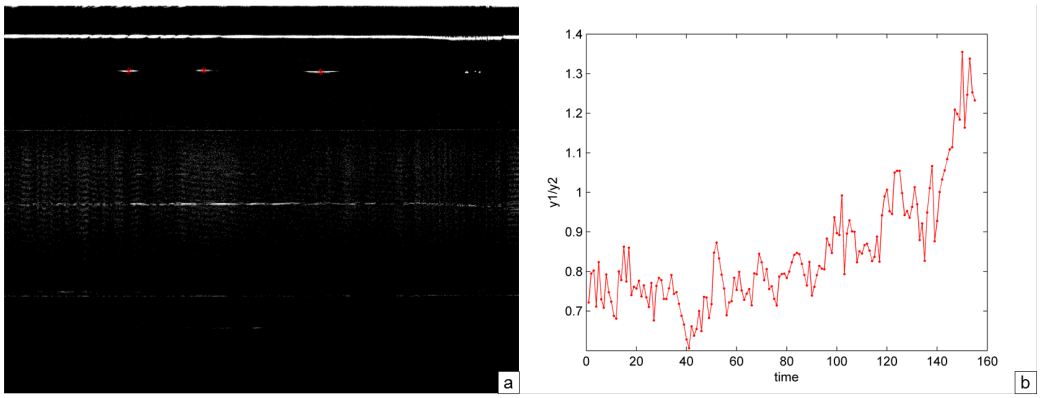

Figure 4.22: (a) OCT image of the three copper wires with the red star as the center of each point; (b) Success metric $f = y_1/y_2$ change while rotating the OCT probe from $\sigma = -45°$ to $\sigma = 45°$ with the rough estimation of the scanning direction.

4.4.1.2 Calibration Error Analysis

Error analysis is to find out the sensitivity of success metric f to the changes of the variables σ and α so that we can decide the robustness of this calibration.

$$\begin{cases} y_1 = \frac{|OP_2|\sin\alpha}{cos(\sigma+\alpha)} \\ y_2 = \frac{|OP_2|\sin\alpha}{cos(\sigma-\alpha)} \end{cases} \tag{4.31}$$

From Eq. (4.31), the success metric can be derived to this form:

$$f = \frac{cos(\sigma - \alpha)}{cos(\sigma + \alpha)} \tag{4.32}$$

The full differential of success metric is:

$$\begin{aligned} df &= \frac{\partial f}{\partial \sigma} d\sigma + \frac{\partial f}{\partial \alpha} d\alpha \\ &= \frac{-sin(\sigma - \alpha)cos(\sigma + \alpha) + sin(\sigma + \alpha)cos(\sigma - \alpha)}{cos^2(\sigma + \alpha)} d\sigma \\ &+ \frac{sin(\sigma - \alpha)cos(\sigma + \alpha) - sin(\sigma + \alpha)cos(\sigma - \alpha)}{cos^2(\sigma + \alpha)} d\alpha \\ &= \frac{sin(2\alpha)}{cos^2(\sigma + \alpha)} d\sigma + \frac{-sin(2\alpha)}{cos^2(\sigma + \alpha)} d\alpha \end{aligned} \tag{4.33}$$

When the scanning direction is close to the optimal direction, $\sigma \approx 0$, so (4.33) becomes:

$$\begin{aligned} df &= \frac{sin(2\alpha)}{cos^2(\alpha)} d\sigma + \frac{-sin(2\alpha)}{cos^2(\alpha)} d\alpha \\ &= 2tan(\alpha) d\sigma - 2tan(\alpha) d\alpha \end{aligned} \tag{4.34}$$

Assuming a fixed value for angle $\alpha = 7.5^\circ$ ($d\alpha = 0$), the resulting full differential will be:

$$df = 0.2633 * d\sigma \tag{4.35}$$

$d\sigma$ means the resulting accuracy we want to achieve with this experimental setup. With probe resolution of $2\mu m$, the possible measurement we will be able to achieve is the probe resolution divided by the glass tube nominal diameter, which is $df = 2/200 = 0.01$. So the $d\sigma = 2.17^\circ$ is measurement accuracy we will have.

4.4.2 Defining the OCT Scanning Plane in Robot Frame

4.4.2.1 Approaching Algorithm

Manual Calibration will only help us roughly find out the scanning plane direction, while to acquire a more reliable scanning plane in robot frame, we developed the following algorithm to help registering the scanning plane to robot base platform frame $\{b\}$. The OCT probe is held stable in the air. The parallel robot with a needle registered to its moving platform is used to approach the scanning plane. When from the OCT image we first see a white dot, which represents the needle tip, we move the robot back and approach again. Do this step for 3 to 4 times until we get the smallest white dot. Then record the needle tip position with respect to the robot base platform frame. Then we move the robot to another place to find the next point. The point clouds we acquire will help us define the scanning plane in robot frame by using the total least squares.

4.4.2.2 Total Least Squares

With the point clouds we acquired from the approaching algorithm, we define the scanning plane in robot base platform frame $\{b\}$ by using the Total Least Squares. Define the scanning plane equation as

$$Ax + By + Cz + D = 0 \tag{4.36}$$

and for possible plane normalization we can define $A^2 + B^2 + C^2 = 1$. The point clouds are ${}^b\boldsymbol{p}_i = (x_i, y_i)$ with $i = [1 \cdots n]$. So the distance of point i to the plane is written as

$$d_i = \frac{Ax_i + By_i + Cz_i + D}{\sqrt{A^2 + B^2 + C^2}} \tag{4.37}$$

The objective error function will be defined as:

$$J = \sum_{i=1}^{n} {d_i}^2 = \frac{1}{A^2 + B^2 + C^2} \sum_{i=1}^{n} (Ax_i + By_i + Cz_i + D)^2 \tag{4.38}$$

To simplify the equation above, we define centroid

$$\begin{cases} \bar{x} = \frac{1}{n}\sum_{i=1}^{n} x_i \\ \bar{y} = \frac{1}{n}\sum_{i=1}^{n} y_i \\ \bar{z} = \frac{1}{n}\sum_{i=1}^{n} z_i \end{cases} \tag{4.39}$$

So the demeaned points are written as:

$$\begin{cases} \tilde{x}_i = x_i - \bar{x} \\ \tilde{y}_i = y_i - \bar{y} \\ \tilde{z}_i = z_i - \bar{z} \end{cases} \tag{4.40}$$

Define $\tilde{D} = D + A\bar{x} + B\bar{y} + C\bar{z}$. Eq. 4.38 is rewritten as:

$$\begin{aligned} J &= \frac{1}{A^2+B^2+C^2}\sum_{i=1}^{n}(A\tilde{x}_i + B\tilde{y}_i + C\tilde{z}_i + \tilde{D})^2 \\ &= \frac{1}{A^2+B^2+C^2}[\sum_{i=1}^{n}(A\tilde{x}_i + B\tilde{y}_i + C\tilde{z}_i)^2 + \sum_{i=1}^{n}\tilde{D}^2 \\ &+ 2A\tilde{D}\sum_{i=1}^{n}\tilde{x}_i + 2B\tilde{D}\sum_{i=1}^{n}\tilde{y}_i + 2C\tilde{D}\sum_{i=1}^{n}\tilde{z}_i] \\ &= \frac{1}{A^2+B^2+C^2}\left[\sum_{i=1}^{n}(A\tilde{x}_i + B\tilde{y}_i + C\tilde{z}_i)^2 + \sum_{i=1}^{n}\tilde{D}^2\right] \end{aligned} \tag{4.41}$$

From Eq.4.41, we can easily decide that two requirements need to be matched to minimize J. First, $\tilde{D} = 0$, which means the plane always passes through center of mass. Under this new condition, the optimization problem is simplified to be:

$$J = min\left[\frac{1}{A^2+B^2+C^2}\sum_{i=1}^{n}(A\tilde{x}_i + B\tilde{y}_i + C\tilde{z}_i)^2\right] \tag{4.42}$$

Define optimization parameter $\boldsymbol{\Xi} = [A,B,C]^T \in \mathbf{R}^{3\times 1}$ and the measurement $\boldsymbol{H} = \begin{bmatrix} \tilde{x}_1 & \tilde{y}_1 & \tilde{z}_1 \\ \vdots & \vdots & \vdots \\ \tilde{x}_n & \tilde{y}_n & \tilde{z}_n \end{bmatrix} \in$

$\mathbf{R}^{n\times 3}$. So Eq.4.42 can be written as:

$$J = min\left(\frac{\Xi^T \mathbf{H}^T \mathbf{H} \Xi^T}{\Xi^T \Xi}\right) \tag{4.43}$$

Hence the optimal solution is the singular vector corresponding to the minimal singular value of $\mathbf{H}^T\mathbf{H}$.

4.5 Conclusions

The integration and deployment of a dual arm system as the one depicted in Fig. 1.7 requires calibration of geometric and optic/imaging distortion. The calibration result should provide an accurate robotic system with well registered tools that could help improving the performance of task priority redundancy resolution proposed in Chapter 2 and assistive telemanipulation study proposed in Chapter 6.

4.5.1 Parallel Robot Calibration

This chapter has presented our algorithm for calibrating the parallel robots. Calibration parameters has been chosen based on the mechanical design uncertainties including the z direction offsets of the spherical bearing position and the linear leg homing error. We carried out calibration on both real parameters and simulation parameters. The simulation parameter shows a perfect convergence. However the kinematic noise index and observability index should be discussed in the future work following the work by Nahvi and Hollerbach in [244]. The calibration on real robot did not show a good result of calibration convergence. This experiment was carried out on our first generation of parallel robots without the modification on mechanical assembly errors. In the modified design of parallel robot, we could avoid the uncertainties on the z direction offsets of the spherical bearing position on both moving and base platform thus reducing the calibration parameters to only the linear leg homing error. This will help reducing the nonlinearity of the

system and new experiments will be performed.

4.5.2 Rapid Hollow Suspended Organ Calibration

The robot calibration also includes the rapid hollow suspended organ calibration. The calibration algorithm was divided into two parts: RCM calibration and rapid organ calibration. Both parts require knowing eyeball angular velocity which will be measured from the magnetic tracker attached to the trocar. Simulations are performed on both calibration algorithms with and without noise on the perfect simulation measurement. Without the noise, simulation shows perfect convergence on the calibration parameters. With the noise, the calibration brings the calibration parameter to a bounded convergence close the real value. An experimental setup with a customized spherical joint as eye ball was designed with magnetic sensor used as the measuring tool for angular velocity. More discussions on the robustness of the calibration algorithm with respect to the increased noise level are still being explored. With a full simulation study and discussion about the feasibility of the calibration algorithm on real setup, this work will be submitted to a journal paper.

4.5.3 OCT Probe Distortion Correction

We detailed rudimentary calibration of the OCT probe by including how to build the calibration pattern and how to perform the calibration experiments. A thin plate spline fitting algorithm is used to dewarp the OCT image. Results show that the calibration removed the distortion and corrected the image scale. Discussion about the computational cost for this algorithm also was discussed and dewarping the OCT image in real time is not realistic. Instead, for the purpose of guiding the robotic control, we shall perform image segmentation first and acquire important information such as tool position, blood vessel position and retina surface in the image frame. Then OCT image calibration will be performed only on these selected points thus reducing the computational cost.

4.5.4 OCT Scanning Plane Registration

In the last section of this chapter, we proposed two methods of defining the OCT probe scanning plane in OCT probe attached frame (defined by the locating pin) and robot base frame, respectively. An experimental evaluation was carried out for the first method by scanning a customized calibration pattern. However the experimental evaluation for the second method was not included in this dissertation work. This could potentially lead to a new area of robotic and OCT integration study that registers the OCT probe to the robotic tools. A common approach of this research topic is ”hand-eye” calibration which has already been adapted to similar imaging technology such as ultrasound. More detailed discussion of this future work could be seen in Chapter 7.

Chapter 5

Evaluation of Microsurgical Tasks with OCT-guidance and/or Robot-assistance

Ophthalmic retinal surgery is carried out under a microscope visualization. The visualization is achieved by dilating the patient's iris and by tilting the eyeball sideways to allow visualization of peripheral regions of the retina. One of the challenges facing surgeons is the ability to gauge depth via narrow baseline stereo visualization. The challenge often requires surgeons to use visual cues such as the tool shadow to discern distance from the retina. In addition, certain anatomy such as the internal limiting membrane or the epiretinal membrane are thin and transparent to the naked eyes. Surgeons have resorted to visualization aids through the use of triamcinolone powder to help visualize the first instant when the gripper disturbs the membrane. This chapter addresses one fundamental question: what is the relative importance of robotic assistance with and without depth feedback using OCT visualization? To answer this question we design a study that tests different combinations of robotic assistance and OCT feedback and compare surgeon performance with and without robot or OCT visualization aids. The following chapter was published in [229]. It is organized as the following. First we present a seven DoF modular robot arm designed for this evaluation task. Then we propose the experimental design and layout. Finally we present the data analysis and discuss about experimental result and draw conclusions.

5.1 Robotic Setup and Operation

The combined B-scan OCT-guided robot for ophthalmic microsurgery was first presented in [228]. Figure 5.1(a) shows an early embodiment of a seven DoF modular robot arm composed from a custom-designed six DoF Stewart-Gough parallel robot and a cam-actuated surgical gripper. The parallel robot is driven by a seven DoF haptic master device

(Force Dimension Omega 7 ®, Nyon, Switzerland). This device tracks and transmits the surgeon's hand movements along with the variable opening and closing angle of the 7^{th} DoF controlling the gripper's desired grasping motion. To use the robotic system, the surgeon sat in front of the robot and held the master device and activated a foot pedal to engage and maintain telemanipulation. A scale of 0.02 was used for converting translational hand movements to commanded robot-assisted forceps movements. In the current study, rotational movements of the forceps along its center axis were not scaled.

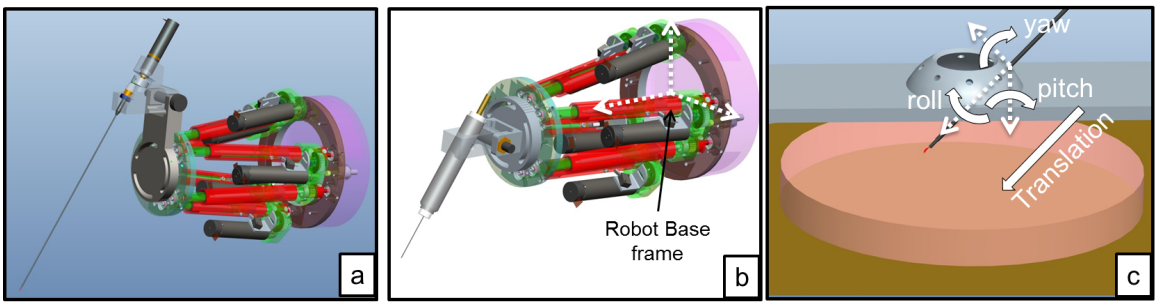

Figure 5.1: Robotic design and layout. (a) A 7 DoF robot was used in this experiment with 6 DoF parallel robot and 1 DoF gripper. (b) The 6 DoF parallel robot also controlled the OCT-forceps probe. (c) Demonstration of the remote center of motion (RCM) located at the sclerotomy in the phantom model eye.

To ensure that the instrument's motions respected the limitations of operating through a sclerotomy, a remote center of motion (RCM) constraint was integrated into the telemanipulation framework [4, 228]. Initially, the surgeon telemanipulated the pre-registered gripper tip mounted on the robotic arm to digitize the RCM point in the robot base frame. The location of the RCM point was saved in the high-level control algorithm. After digitizing the sclerotomy, the surgeon guided the robot to insert the gripper through the sclerotomy. During this phase, the telemanipulation was carefully performed without imposing RCM constraints. After the robot-assisted gripper was inside the eye model, the RCM constraints were enabled. The assisted telemanipulation automatically maintained the scleral constraints while allowing the surgical instrument to move with four DoF (pitch/yaw and translate/roll along the longitudinal axis of the tool) (Fig. 5.1(c)).

5.2 Experimental Design

The two tasks designed for evaluating the performance of manual manipulation and robot-assisted telemanipulation were: 1) controlled approach and touch of the forceps' tips to a surface, and 2) peeling of a surface membrane. In the first task, the surgeon was asked to bring the surgical forceps towards the surface of a gelatin model (20 g Knox Gelatine powder (Kraft Foods Global, Inc., Northfield, IL)), and 60 g Coffee-mate (Nestle USA, Glendale, CA) in 250 ml hot water) or the surface of a goat *ex vivo* retina. The goal was to touch the gripper tip to the surface with minimal penetration into the phantom or retinal tissue. Although the OCT probe was capable of imaging retina through vitreous in an intact cadaver goat eye as shown in Fig. 5.3(a)-(c), we chose the *ex vivo* model to enable side-view recording of the instrument touching the surface. For the membrane peeling task, the surgeon lifted a uniform phantom membrane which was created using New-Skin Liquid Bandage (Medtech Products, Inc., Irvington, NY) placed on the gelatin surface based upon the protocol of Iyer, *et al.* [231]. The thickness of this phantom membrane was approximately 10 μm. This phantom membrane was thinner than an epiretinal membrane averaging about 61 μm [87]. However, it was greater than the average internal limiting membrane thickness of 2.5 μm. Formation of artificial membranes upon cadaver goat retina was not uniform as seen in Fig. 5.3(d)-(f), with variability ranging from a thin coating Fig. 5.3(d), to non-adherence due to retinal surface moisture Fig. 5.3(e), to contraction of the retina surface Fig. 5.3(f). Therefore, this model was not used to compare the techniques since nonuniform membrane formation was a confounding variable.

5.2.1 Experimental Layout and Experimental Conditions

Figure 5.2 shows the experimental setup for both manual manipulation and robot-assisted telemanipulation. The phantom retinal platform consisted of a plastic-molded sclerotomy and the gelatin surface (Fig. 5.1 (c)). A side-viewing microscope (Omano E-

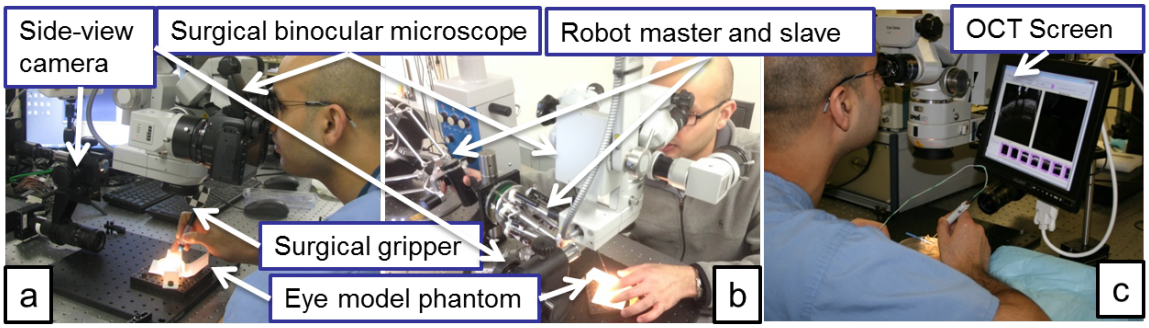

Figure 5.2: Experimental layout for manual and robot-assisted tasks. (a) For manual manipulation, the surgeon held an ophthalmic forceps or B-scan OCT-forceps and manipulated the forceps through a mockup sclerotomy constraint above the gelatin retinal phantom. (b) For robotic manipulation, the surgeon held the robot master device and controlled the slave robot to manipulate a customized ophthalmic forceps. (c) Layout with a small side-view OCT screen to improve visualization of real-time OCT feedback.

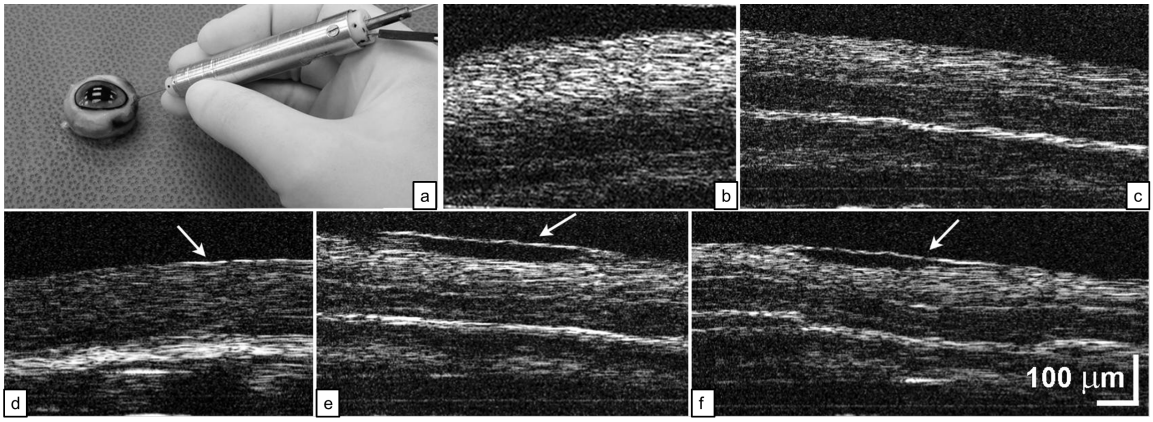

Figure 5.3: (a-c) The OCT probe with approximately 2mm scan length is capable of imaging retina through vitreous in an intact cadaver goat eye. (d-f) *Ex vivo* goat retina was used to enable application of artificial membranes. Nonuniform (d) tight adherence, (e) loose adherence, or (f) retinal contraction developed. Scale bars indicate the length of the images.

ZVU/V-15 Digital Microscope, Japan) with attached camera (Dragonfly 2 ®, Point Grey Research Inc., Richmond, Canada) recorded an external video of the gripper tip's motion. These images were not visible to the surgeon, and were used for post-processing analysis of the forceps' motions.

When performing the manual tasks (Fig. 5.2(a)), the surgeon held either a standard Grieshaber Revolution DSP MaxGrip intraocular forceps (Alcon, Fort Worth, TX) or the 23-gauge combined B-scan OCT-forceps. During the robot-assisted modes (Fig. 5.2(b)), the surgeon held the master device and activated a foot pedal to enable the robotic telemanipulation coupling. When real-time OCT feedback was introduced into the experimental conditions, the surgeon worked with two visual inputs: 1) the surgical binocular microscope and 2) a large distant real-time OCT video screen. Repeated redirection of the eyes from the binocular microscope to visualize the OCT images can significantly diminish hand stability. Therefore, to reduce the impact of this distraction, a small 7" screen (SMART USB Monitor, Model: DS-70U, DoubleSight Displays, Costa Mesa, CA), which displayed the real-time OCT images, was positioned adjacent to the binocular microscope (Fig. 5.2(c)). Less ocular movement was required to view this small screen for real-time OCT feedback.

Table 5.1 lists the experimental conditions with the approaching task evaluated with both the gelatin model and goat *ex vivo* retinas, and the membrane peeling task evaluated with the gelatin model. Membrane peeling with the *ex vivo* retinas was not performed due to difficulty in replicating identical membranes on this tissue (Fig. 5.3(d)-(f)). The gelatin phantom approach experimental conditions were: (A) manual surgical forceps, (B) robot-assisted forceps, (C) manual B-scan OCT-forceps, (D) robot-assisted B-scan OCT-forceps, and (E) manual B-scan OCT-forceps with OCT-image side screen. The *ex vivo* retinal surface approach experimental conditions were:(F) manual surgical forceps, (G) robot-assisted forceps, (H) manual B-scan OCT-forceps, (I) robot-assisted B-scan OCT-forceps, and (J) manual B-scan OCT-forceps with OCT-image side screen. The phantom membrane peeling conditions were: (K) manual surgical forceps, (L) robot-assisted forceps, and (M) manual

B-scan OCT-forceps with OCT-image side screen. The effect of the small adjacent monitor regarding OCT feedback was determined by comparing conditions (E) to (C) and (J) to (H).

Table 5.1: Experimental models and conditions used.

Task	Exp. #	Model	Manual	Robot-assisted	OCT Feedback	OCT Side Screen
Approach	A	Gelatin	✓			
	B	Gelatin		✓		
	C	Gelatin	✓		✓	
	D	Gelatin		✓	✓	
	E	Gelatin	✓		✓	✓
Approach	F	Goat retina	✓			
	G	Goat retina		✓		
	H	Goat retina	✓		✓	
	I	Goat retina		✓	✓	
	J	Goat retina	✓		✓	✓
Peeling	K	Gelatin	✓			
	L	Gelatin		✓		
	M	Gelatin	✓		✓	✓

5.3 Experimental Results

5.3.1 Experimental Data Analysis

Matlab image toolbox (Matlab ®, MathWorks, Natick, MA) was used to process the videos from the side-viewing camera. Figures 5.4(a)-(e) show one frame corresponding to experiments(A) to (E), respectively (Table 5.2). Each video was segmented when the forceps reached its lowest point. Typically, the gripper tip was slightly embedded into the gelatin, but the plane of the gelatin could not be determined. However, the video contained the forceps' reflection from the gelatin's surface. Since the distance that the gripper tip was embedded could not be measured directly, a template for both the forceps' image and the reflected forceps' image was prepared to estimate the location of both. In Fig. 5.4(a)-(e), the red line was the segmented outline of the gripper with the red dot indicating the lowest point of the gripper and the blue line was the outline of the reflected gripper with the blue dot indicating the highest point of the reflection. We registered the blue and red outlines

manually onto each picture. Half of the distance between the red and blue dots was used to estimate the gripper excursion depth in pixels into the gelatin substrate. The distance was then converted to microns by using the actual gripper length of 812 μm and its pixel length in each image to calculate the image scaling factor (γ(microns/pixel)) for each trial. Results are listed in Table 5.2 and described in section 4.2.

Figures 5.4(f)-(j) show one retinal touch attempt for each of the respective experimental conditions (F) to (J). The gripper shape was segmented in red outline and the blue line indicated the blood vessel surface's location before the gripper touched it. Since there was no clear reflection from the goat retina, the blood vessel was the reference in calculating the excursion depth beyond the retinal surface. This distance was likewise calculated in microns from the forceps' tip (red dot) to the corresponding pre-touch blood vessel surface (blue dot). The experimental results are listed in Table 5.3 and described in detail in section 4.2. Representative side-viewing videos are presented for the (A) manual forceps touching gelatin, (B) robot-assisted forceps touching gelatin, (H) manual OCT-forceps touching retina, and (I) robot-assisted OCT-forceps touching retina.

Additional segmentations of the externally viewed motion of the gripper tips during one cycle of approach and retraction from the gelatin with manual surgical forceps (Fig. 5.4(k) and with robot-assisted forceps (Fig. 5.4(l) were performed. These videos were automatically segmented using the template-matching method. The red points represented instrument approach while the blue points represented instrumental retraction. Qualitatively, greater lateral movements occurred with the manual forceps rather than with the robot-assisted forceps as expected. In addition, an example of real-time B-scan OCT imaging for four of the OCT-guided surface-touching conditions, including (C) manual B-scan OCT-forceps approaching gelatin retinal phantom (Fig. 5.5 (a), (D) robot-assisted B-scan OCT-forceps approaching gelatin retinal phantom (Fig. 5.5 (b), (H) manual B-scan OCT-forceps approaching a goat *ex vivo* retina (Fig. 5.5 (c), and (I) robot-assisted B-scan OCT-forceps approaching a goat *ex vivo* retina (Fig. 5.5 (d) are illustrated.

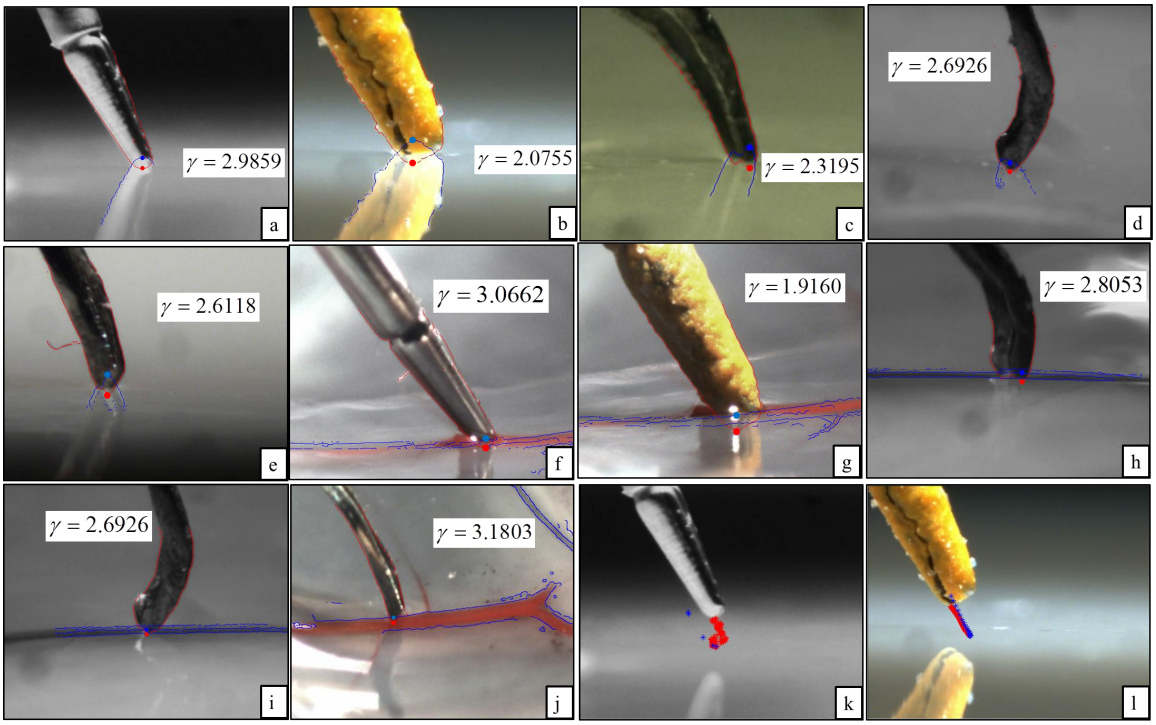

Figure 5.4: Side-view image segmentation examples of the lowest point in one approaching attempt for each experimental condition. The red outline determined the lowest point of the gripper and the blue outline located the highest point of the reflected gripper. (a) through (j) are correlated with experiments (A) through (J). Corresponding videos are presented for the (a) manual forceps touching gelatin, (b) robot-assisted forceps touching gelatin, (h) manual OCT-forceps touching retina, and (i) robot-assisted OCT-forceps touching retina. (k, l) Examples of approaching(red) and retraction(blue) paths of the forceps' tips motion with (k) manual control and (l) robot-assisted control with obvious reduction in lateral movement with robot-assisted control.

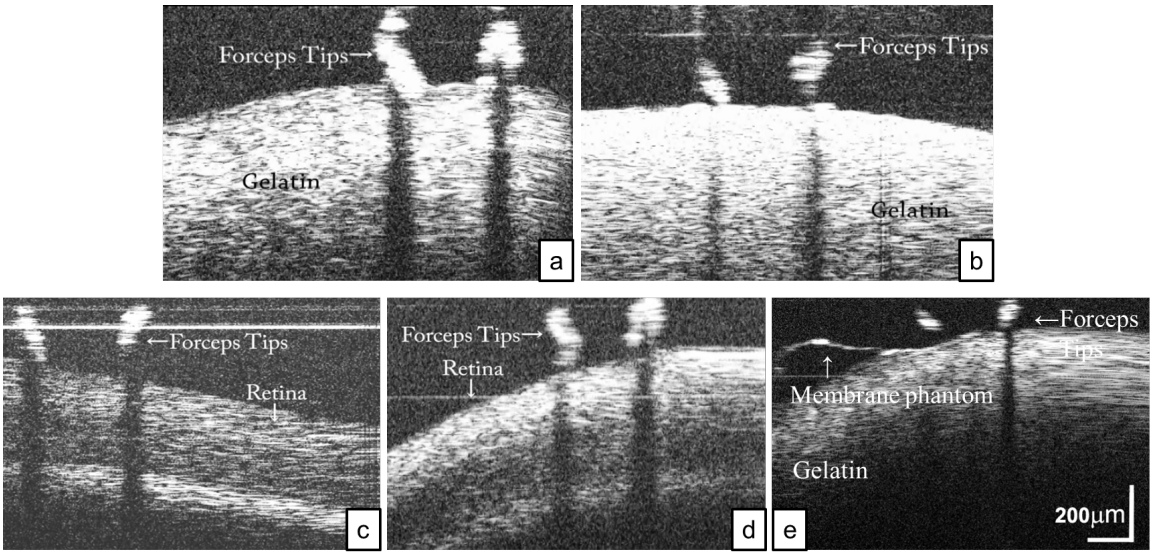

Figure 5.5: Real-time B-scan OCT imaging examples for the OCT-guided conditions. (a) Manual B-scan OCT-forceps approaching gelatin phantom. (b) Robot-assisted B-scan OCT-forceps approaching gelatin phantom. (c) Manual B-scan OCT-forceps approaching goat *ex vivo* retina. (d) Robot-assisted B-scan OCT-forceps approaching goat *ex vivo* retina. (e) Real-time B-scan OCT imaging of peeling membrane phantom from gelatin

Peeling of the membrane phantom was possible with all 3 conditions (K) through (M). The number of attempts required for a successful membrane removal were recorded. The results of these experiments are listed in Table 5.4 and described in detail in section 4.2. An example of successful peeling with each of the conditions: (K) manual surgical forceps (Fig. 5.6 (a)), (L) robot-assisted forceps (Fig. 5.6 (b)), and (M) manual B-scan OCT-forceps with OCT-image side screen (Fig. 5.6 (c)) is illustrated (Fig. 5.6). An example of real-time B-scan OCT imaging of peeling membrane phantoms from the gelatin surface is presented (Fig. 5.5(e) during condition (M) using the manual B-scan OCT-forceps with the OCT-image side screen.

5.3.2 Experimental Data Results

The results of approaching the gelatin phantom model are listed in Table 5.2. For total completion time, manual procedures were faster than robot-assisted procedures. This is because the speed of the robot was regulated to $1/50$ of the surgeon's hand speed for stability

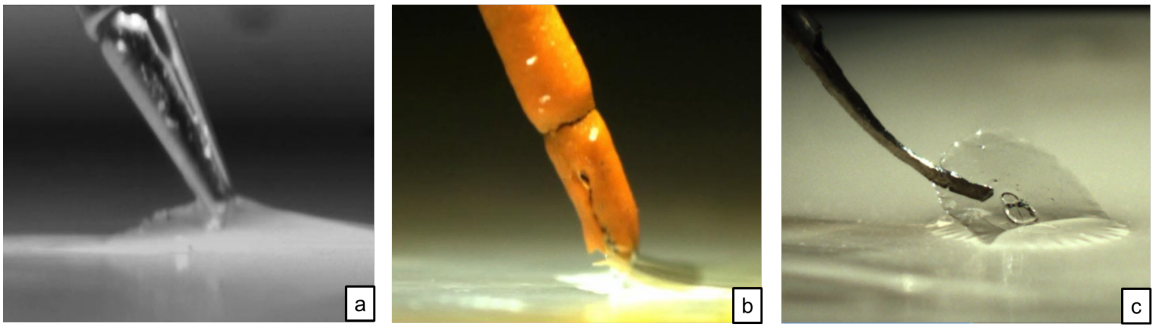

Figure 5.6: Sid-view images of successful membrane phantom peelings from the gelatin surface. (a) Condition (K) using the manual surgical forceps. (b) Condition (L) using the robot-assisted forceps. (c) Condition (M) using the manual B-scan OCT-forceps with OCT-image side screen.

purposes. The last column provides the average depth $\pm$ standard deviation (S.D.) of the depth of excursion into the gelatin substrate. All distances were converted into microns. The non-parametric Kruskal-Wallis One Way Analysis of Variance (ANOVA) on Ranks demonstrated a statistically significant difference ($p < 0.001$) among the 5 groups. The smallest depth of penetrance of 13 ± 8 μm by the Tukey test ($p < 0.05$) was obtained when the surgeon used the robot with OCT feedback (D) (Fig. 5.7(a)). The comparisons among the groups are illustrated in Fig. 5.7(a) with significantly different ($p < 0.05$) comparisons identified. Figure 5.7(a) shows that there was no significant difference between the data acquired in experiments (A) and (B). This means that without OCT feedback, robotic assistance does not improve manual ability in depth judgment beyond the limitation of the surgical binocular microscope. When OCT feedback was introduced, manually holding the OCT-integrated forceps with the OCT image projected on a distant standard monitor did not have any improvement on the ability of performing the task due to the requirement of shifting gaze from the microscope to the distant screen. A small adjacent side screen as shown in Fig. 5.2(c) allowed the surgeon to limit eye movements for the OCT feedback and significantly improved the depth perception compared to the distant screen task (C), although it was not quite statistically superior over the manual forceps alone (24 μm vs 28 μm, $p > 0.05$, Tukey test). Finally, the robot-assisted OCT integrated forceps (D) produced

the best results than any other experimental condition in touching the gelatin with minimal penetration into the substrate.

The results of approaching and touching the goat retina are listed in Table 5.3. Again, manual procedures were faster than robot-assisted procedures. The last column provides the average depth $\pm$ standard deviation (S.D.) of the depth of excursion into the retina. All distances were converted into microns. The non-parametric Kruskal-Wallis One Way Analysis of Variance (ANOVA) on Ranks demonstrated a statistically significant difference ($p < 0.001$) among the 5 groups. Comparisons among the groups are illustrated in Fig. 5.7(b) with significantly different ($p < 0.05$) values identified. The smallest depth of penetrance of 21 $\pm$ 11 μm again was obtained when integrated robot-assist and OCT feedback (I) was used (Fig. 5.7(b)), although it was not statistically different than the depth of 34 $\pm$ 17 μm produced by the manual integrated OCT-forceps with the small side view screen. Again, without OCT feedback, robotic assistance did not improve depth judgment significantly. OCT feedback reduced penetrance in the retinal touch task.

Demonstration that a first-generation prototype integrated OCT-forceps was capable of lifting a thin yet visible phantom membrane of Liquid Bandage upon gelatin was undertaken. Table 5.4 lists the membrane peeling results in experimental conditions manual (K), robot-assisted (L) and manual integrated OCT-forceps (M). The averages and standard deviations were plotted in Fig. 5.7(c). The nonparametric Kruskal-Wallis One Way Analysis of Variance (ANOVA) on Ranks ($p = 0.236$) indicated that the differences in the average values among the treatment groups were not statistically significantly different. The prototype integrated OCT-forceps was equally capable of peeling the membranes despite having smooth tips rather than commercial specialized tips with teeth. The total time for completing the task was also least with the integrated OCT-forceps (Table 5.4).

Besides the data documented in Tables 5.2-5.4 and Fig. 5.7, it was also observed that the robot-assisted manipulations were more stable than the manual manipulations. More lateral movement occurred with manual (Fig. 5.4(k)) than with robot-assisted (Fig. 5.4(l))

movements. Since the tasks designed in this study evaluated the accuracy in depth perception, the obvious stability advantage of the robot did not manifest itself in the results of this study.

Table 5.2: Results of approaching task on gelatin phantom model.
M. = Manual; R. = Robotic; O. = OCT feedback; S.S. = Small Screen; S.D. = Standard Deviation

Exp. #	**M.**	**R.**	**O.**	**M. + S.S.**	**# of Attempts**	**Total Completion time (s)**	**Average depth (S.D.) (μm)**
A	✓				40	449	28(9)
B		✓			40	470	31(6)
C	✓		✓		40	171	36(16)
D		✓	✓		40	522	13(8)
E	✓		✓	✓	40	142	23(13)

Table 5.3: Results of approaching task on *ex vivo* retina.
M. = Manual; R. = Robotic; O. = OCT feedback; S.S. = Small Screen; S.D. = Standard Deviation.

Exp. #	**M.**	**R.**	**O.**	**M. + S.S.**	**# of Attempts**	**Total Completion time (s)**	**Average depth (S.D.) (μm)**
F	✓				40	114	65(41)
G		✓			40	220	66(24)
H	✓		✓		40	162	50(27)
I		✓	✓		40	319	21(11)
J	✓		✓	✓	40	147	34(17)

Table 5.4: Results of membrane peeling task of liquid bandage on gelatin phantom.
M. = Manual; R. = Robotic; O. = OCT feedback; S.S. = Small Screen; S.D. = Standard Deviation.

Exp. #	**M.**	**R.**	**O.**	**M. + S.S.**	**# of Attempts**	**Total Completion time (s)**	**Fail to peel**	**Average (S.D.) attempts for successful peel**
K	✓				85	1603	0	2.1 (2.5)
L		✓			85	1534	3	1.5 (0.9)
M	✓		✓	✓	85	1422	0	1.8 (1.2)

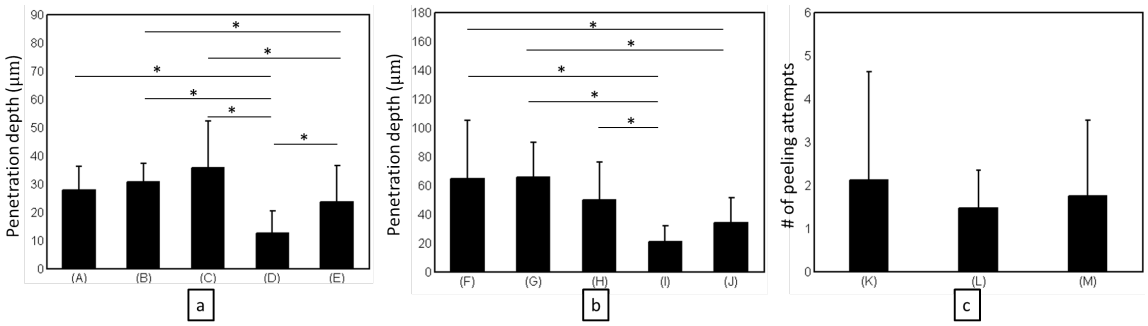

Figure 5.7: Averages and standard deviations of the data with significantly different groups marked with * ($p < 0.05$). The x-axis labels the experimental condition as described in Table 5.1. The y-axis indicates the means and standard deviations of the measurements. (a) The approaching task to the gelatin phantom model (A to E); (b) The approaching task to the *ex vivo* goat retina (F to J); (c) The membrane peeling task on the gelatin phantom model (K to M).

5.4 Conclusions

A series of experimental conditions to evaluate the potential benefits of using robotic assistance and OCT-feedback was performed. Two benchmarking tasks included touching a gelatin phantom surface and an *ex vivo* goat retinal surface while avoiding penetration into the substrates. They were performed under five different experimental conditions, which included manual and robot-assisted performance with and without 23-gauge forward-imaging B-scan OCT feedback to the user. Compared to previous robotic works [113], our study focused on evaluating control of depth penetration instead of the lateral steadiness superiority that is expected with robotic systems.

The results demonstrated that when operating through the sclerotomy constraints of the phantom eye model, the robot alone did not improve the surgeon's depth judgment in touching the gelatin phantom or the *ex vivo* goat retinal surface. When the OCT feedback was introduced, manually holding the OCT probe tool initially worsened performance, because the surgeon had to shift his vision between the surgical microscope binoculars and the distant large OCT image screen. Addition of a small side-view monitor next to the microscope binoculars for real-time OCT image display greatly improved the manual performance of

the approaching tasks which emphasized the need for improved monitors for intraoperative OCT viewing. Tao, *et al.* recently described projecting an OCT image through a surgical microscope ocular which may even further improve performance [138]. When the real-time feedback from the 23-gauge OCT-forceps was combined with robot-assist control, the surgeon's performance was dramatically improved compared to the other experimental conditions. This is consistent with prior robot-assisted studies which demonstrated improved microsurgical performance by significantly reducing hand tremors [106, 107, 113]. Similar reduction of lateral drift with the approach tasks was observed with the robot-assist forceps compared to the manual forceps as depicted in Fig. 5.4(k) and 5.4(l).

The membrane peeling task demonstrated that the first-generation integrated OCT-forceps prototype was equally capable of peeling membrane phantoms despite having smooth tips compared to the other forceps designed with special tips for grasping membrane edges. Additional system improvements will be to optimize the tips of the forceps for grasping thin membranes. In addition, an ideal future phantom model would contain a standardized thin membrane barely visible *en face* through the surgical microscope to better compare the capabilities of the system with and without both real-time OCT imaging and robotic assistance. Although a cadaver animal retina unfortunately has variable retinal thickness and nonuniform responses to artificial membrane placement to preclude quantitative comparisons of membrane peeling, it was useful for demonstrating initial preclinical feasibility. A vitrectomized living ocular model will be the next step in the preclinical evaluation of the intraocular OCT-forceps probe. Rotational movements of the forceps will be scaled in future experiments to increase mobility. Algorithms as developed by Huang and Kang [245] will minimize reference fixed pattern artifact and saturation artifacts. In addition, an OCT engine with faster real-time acquisition rate should improve the quality.

In conclusion, real-time intraocular B-scan OCT visualization of tissue microstructure and feedback of surgical maneuvers is a desired ophthalmic feature. Real-time manual OCT-forceps feedback with a small side monitor and real-time robot-assisted OCT-forceps

feedback improved depth perception accuracy. Future studies will examine whether more intricate sub-retinal and retinal vascular maneuvers can be performed with the intraocular robot-assisted OCT-forceps to permit the improvement of current vitreoretinal procedures as well as the development of new techniques. The work on this statistical study together with the proposed OCT integrated gripper in Chapter 3 has been published in [229].

Chapter 6

Assistive Telemanipulation

The integration of OCT image feedback to guide robots during telemanipulation control assistance is a new approach to combine the benefits of robotic precision and OCT perception of anatomical structures. While there have been studies dealing separately with robotics (e.g. [246, 105, 247, 106, 107, 108, 26]) or OCT guidance (e.g. [151, 152]), there is a sparsity of works presenting solutions enabling the combination of both technologies (e.g. [227, 228]). This chapter aims to address a gap in knowledge on robotic image guidance and assistive control using intraocular B-mode OCT imaging.

Simpler A-scan probes are being developed by several groups for ophthalmic surgery (e.g. [227, 158, 160]). However, A-scan OCT probes only provide one dimensional depth information when the probe is fixed. By scanning the entire probe, these A-scan probes could be used to provide 3D scans of the retinal structures [248]. This movement constraint precludes the ability to simultaneously image attached tools and underlying anatomy for the purpose of real-time image feed-back. Joos et al. presented in [249] a miniature intraocular B-mode miniature OCT probe that provided a real-time cross-sectional images of the retina and the tool. This probe offers a unique opportunity for robotic assistance since it provides high-resolution cross-sectional images of the retina for a fixed probe location.

Virtual fixtures (VF) [250] have been used by several groups for vision-guided micromanipulation and tremor filtering. Previous works [115, 114, 251] have demonstrated computer vision VF to improve the accuracy of ophthalmic interventions. However, the VF of these works was limited to assistive guidance in the directions lateral to the tool tip due to limited depth perception when using the microscope. In the depth direction, tremor filtering has been guided by A-mode OCT measurements as presented by Song, et al. [252, 253]. The work in this chapter is inspired by these previous investigations and aims to extend

them by offering a control framework for VF laws using computer vision for lateral motion adjustment and B-mode OCT information for depth sensing in order to develop 3D VF that enforce motion boundaries and at the same time guide the robotic tool to the targeted position. A VF law will be developed based on the feedback from these two imaging techniques.

This work extends previous works on microscope-based VF to include the B-scan OCT assistance. We carry out the first stride towards developing real-time visual servoing technology combining a microscope, an intraocular B-mode OCT and robotics. A microscope and OCT combined 3D VF control law enables assistive telemanipulation. Micro-injection on phantom blood vessel model demonstrates the proposed VF. The majority of the work presented in this chapter has led to the following journal paper [239].

6.1 Telemanipulation Integration Architecture

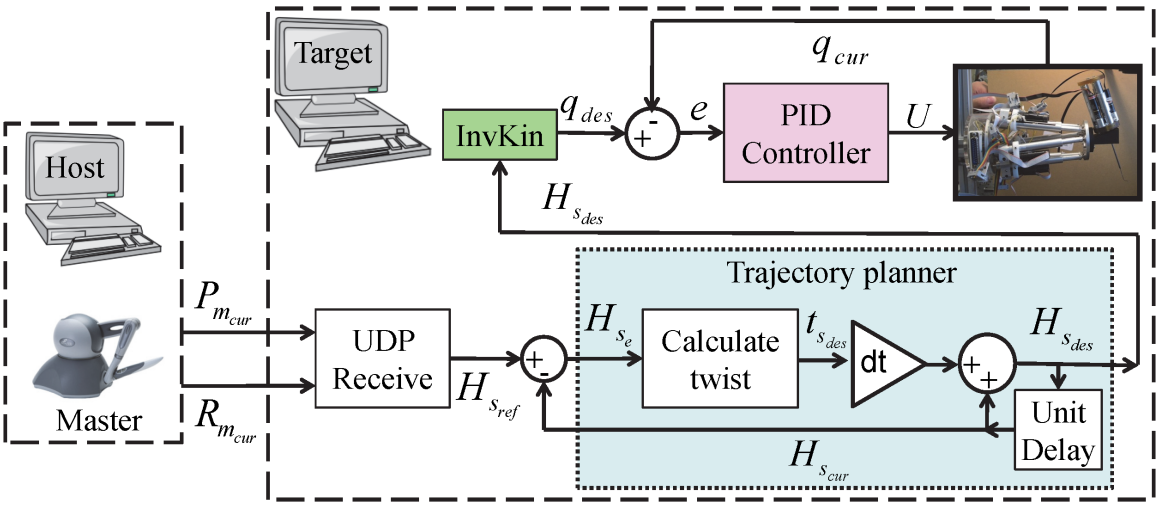

Figure 6.1: Telemanipulation integration architecture of eye parallel robot

Figure 6.1 shows the 1-arm telemanipulation integration architecture. The *Host* computer keeps querying the master device and communicates with the *Target* computer over a Local Area Network (LAN) via User Datagram Protocol (UDP). The reference pose (position and orientation) of the slave robot is input to a trajectory planner that interpo-

lates the instantaneous desired slave robot poses at 1kHz control loop frequency. Since this frequency is higher than the UDP communication rate (125 Hz) the trajectory planner smoothes the motion of the slave robot. Each interpolated pose is then fed into an inverse kinematics block that calculates the desired value of each joint and sets it as a reference to a joint-level PID controller.

To initiate telemanipulation, a foot switch is used to engage the master. At the first instant of foot switch press, the system acquires the homogenous transforms representing the master and slave robot initial configurations $\mathbf{H}_m^*$ and $\mathbf{H}_s^*$, respectively. Movement of the master stylus from $\mathbf{H}_m^*$ is used to calculate the unscaled motion reference to the slave robot:

$$\Delta\mathbf{R}_m = \mathbf{R}_m^{*\,T}\mathbf{R}_{m_{cur}}, \quad \Delta\mathbf{p}_m = \mathbf{p}_{m_{cur}} - \mathbf{p}_m^* \tag{6.1}$$

where subscript *cur* stands for *current* values. Position and rotation scaling is first implemented by transforming $\Delta\mathbf{R}_m$ into its exponential map representation $\Delta\mathbf{R}_m = e^{\gamma_m[\hat{\boldsymbol{\eta}}_m\times]}$ where γ_m and $\hat{\boldsymbol{\eta}}_m$ represent the rotation angle and rotation axis. Here $[\hat{\boldsymbol{\eta}}_m\times]$ is the cross product matrix of vector $\hat{\boldsymbol{\eta}}_m$. The reference configuration of the slave robot (subscript ref) is:

$$\mathbf{R}_{s_{ref}} = \mathbf{R}_s^* e^{k_r\gamma_m[\hat{\boldsymbol{\eta}}_m\times]}, \quad \mathbf{p}_{s_{ref}} = \mathbf{p}_s^* + k_t\Delta\mathbf{p}_m \tag{6.2}$$

where, k_r and k_t are rotation and translation scaling constants.

The path planner smoothes the slave motion by interpolating the desired slave poses using its current tracking error. The current slave pose, $\mathbf{H}_{s_{cur}}$, is fed back after a unit delay from trajectory planner output, $\mathbf{H}_{s_{des}}$, and it is used to calculate the slave tracking error (subscript e) $\mathbf{H}_{s_e}$.

$$\mathbf{p}_{s_e} = \mathbf{p}_{s_{ref}} - \mathbf{p}_{s_{cur}}, \quad \mathbf{R}_{s_e} = \mathbf{R}_{s_{ref}}\mathbf{R}_{s_{cur}}^T \tag{6.3}$$

The slave desired (subscript des) twist $\mathbf{t}_{s_{des}}$ is calculated using the slave tracking error:

$$\begin{aligned} \mathbf{v}_{s_{des}} &= \alpha_t v_{max} \frac{\mathbf{p}_{s_e}}{\|\mathbf{p}_{s_e}\|}, \quad \alpha_t \in [0,1] \\ \omega_{s_{des}} &= \frac{\alpha_r \omega_{max} \hat{\boldsymbol{\eta}}_{s_e}}{sin(\gamma_{s_e})}, \quad \alpha_r \in [0,1] \end{aligned} \tag{6.4}$$

where $\mathbf{R}_{s_e} = e^{\gamma_{s_e}[\hat{\boldsymbol{\eta}}_{s_e}\times]}$. Hence, the desired interpolated slave pose is:

$$\begin{aligned} \mathbf{p}_{s_{des}} &= \mathbf{p}_{s_{cur}} + \mathbf{v}_{s_{des}} \Delta t \\ \mathbf{R}^{\divideontimes}_{s_{des}} &= \mathbf{R}_{s_{cur}} + (\Omega_{s_{des}} \mathbf{R}_{s_{cur}}) \Delta t \end{aligned} \tag{6.5}$$

where Δt is the control loop timestep and $\Omega_{s_{des}} = [\boldsymbol{\omega}_{s_{des}}\times]$ is the desired skew symmetric spatial angular velocity such that $\dot{\mathbf{R}}_{s_{cur}} = \Omega_{s_{des}} \mathbf{R}_{s_{cur}}$. The matrix $\mathbf{R}^{\divideontimes}_{s_{des}}$ needs to be renormalized to maintain a proper rotation matrix. Renormalization is achieved in each iteration step using Gram Schmidt orthogonalization.

Given $\mathbf{p}_{s_{des}}$ and $\mathbf{R}_{s_{des}}$, we invoke the inverse kinematics of the parallel robot which has a simple closed form expression.

6.2 Microscope and OCT Guided 3D Virtual Fixtures

6.2.1 Robot Manipulator for Visual Guided Virtual Fixture

Figure 6.2, shows an overview of our robotic telemanipulation slave including a customized Stewart-Gough parallel platform, the tool connector, an injection tool with linear actuation unit, 20 μL syringe (Innovative Labor Systeme Microsyringes 20μL) and a custom bent glass micro-pipette (World Precision Instruments μ TIP TIP1-TW1-L), the B-scan OCT probe, and a phantom of agar gel with an embedded channel. The tool connector holds the actuation unit, the micro-syringe and an adjustable connecting part to the OCT probe. The adjustable connecting part allows aligning the position of the B-scan OCT probe to view the tip of the micro-pipette.

The rationale for the co-planar micro-pipette and OCT probe stems from the need to visualize the micro-pipette tip for real-time control. In [254], a gripper coaxially aligned with the OCT probe was presented and in [255] an injection pipette was placed adjacent to the OCT probe axis. To gain the best OCT image quality, the OCT probe is optimal perpendicular to the substrate. A straight glass micro-pipette was bent using heat to provide a bending of 30°. During injection into a channel, the micro-pipette should approach the phantom surface at an appropriate angle of approximately 30° between the micro-pipette tip and the local tangent of the surface [118].

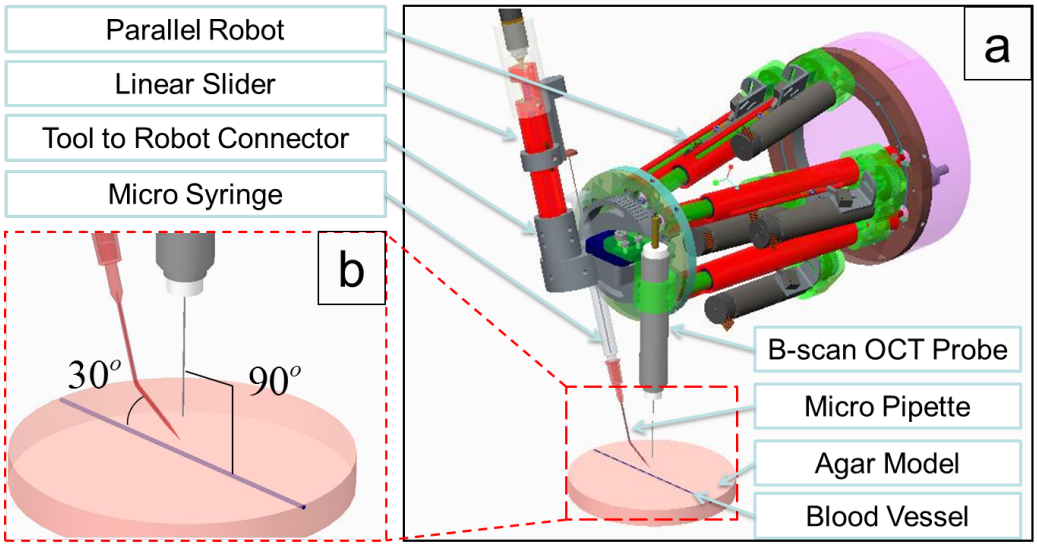

Figure 6.2: The robotic manipulator design included: a parallel robot, tool connector, micro-syringe, micro-pipette, micro-syringe actuator, a OCT probe and an agar model with the phantom blood vessel.

6.2.2 Real-time Image Segmentation

To develop the visual based VF law, online image segmentation of both the B-mode OCT stream and the microscope video (Fig. 6.3(a)) are necessary. For OCT image segmentation, a median filter was used to diminish noisy points and then segment the tool tip, the top layer of the retina and the blood vessel. Segmentation of the microscope images was carried out by marking the tip of a micro pipette with color as a fiducial point (Fig.

6.3(a)). The relative offset between the micro pipette tip and the center of the fiducial point is constant. Thus, color-based segmentation of the fiducial point provides the location of the micro pipette tip. For simplicity, the orientation of the micro pipette is kept at a constant orientation and the robot is translated in an open environment setup (Fig. 6.2). A Qt dialog was created to acquire the B-mode OCT stream and perform an OpenCV based color segmentation at 20 Hz. The segmented fiducial points are marked green in Fig. 6.3(c). The target (e.g. line or phantom blood vessel) in the microscope image vary in different experiments. We apply similar color segmentation to generate target point clouds. A median filter and threshold are applied on these point clouds to remove noise. The closest point on the target from the segmented tool tip is found using a local search algorithm. In Fig. 6.3, the distance from the tool tip to the closest point on the target is defined as d_{tip} and $\hat{\mathbf{n}}_{tip}$ defines the unit vector pointing from the tool tip to the closest point. The perpendicular direction of $\hat{\mathbf{n}}_{tip}$ designates the direction of the local tangent at the closest point. This Qt dialog also has the functionality of sending the real-time segmented image information to the slave robot using UDP package send command.

6.2.3 Microscope Based 2D Virtual Fixture

As a first step to vision-based VF, the registration of the microscope image frame to the robot frame must be carried out. In Fig. 6.3(c), frame $\{\mathrm{c}\}$ represents the microscope image frame and frame $\{\mathrm{b}\}$ designates the robot base frame. A planar agar model was used as a surrogate for representing an approximation of a very small patch of the retina. The planar agar model was aligned parallel to the x-z plane of the robot frame. Registration of the image frame to the robot frame was achieved by commanding the robot to move in its $\hat{\mathbf{x}}_b$ and $\hat{\mathbf{z}}_b$ direction and recording from the microscope the motion of the micro pipette tip to define $\hat{\mathbf{x}}_b$ and $\hat{\mathbf{z}}_b$ in frame $\{\mathrm{c}\}$ as shown in Fig. 6.3(c). Since the microscope does not view the retina model exactly from a perpendicular direction, the image is slightly distorted. Nevertheless, the resulting transformation ${}^{b}\mathbf{R}_{c}$ obtained using the method above is a good

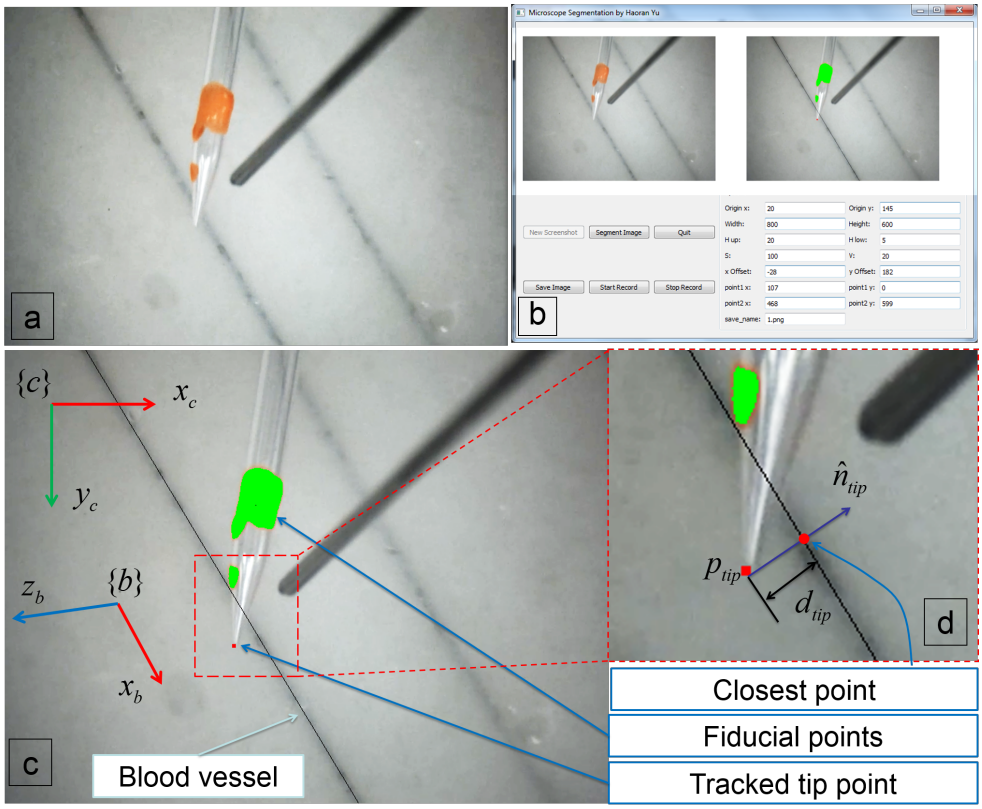

Figure 6.3: Microscope image segmentation: (a) the microscope stream was captured in real-time; (b) a program was written for tracking the micro-pipette tip and the blood vessel; (c),(d) the online segmentation showed tracking results of the micro-pipette tip, the closest point on the blood vessel from the tip and the local tangential direction along the blood vessel.

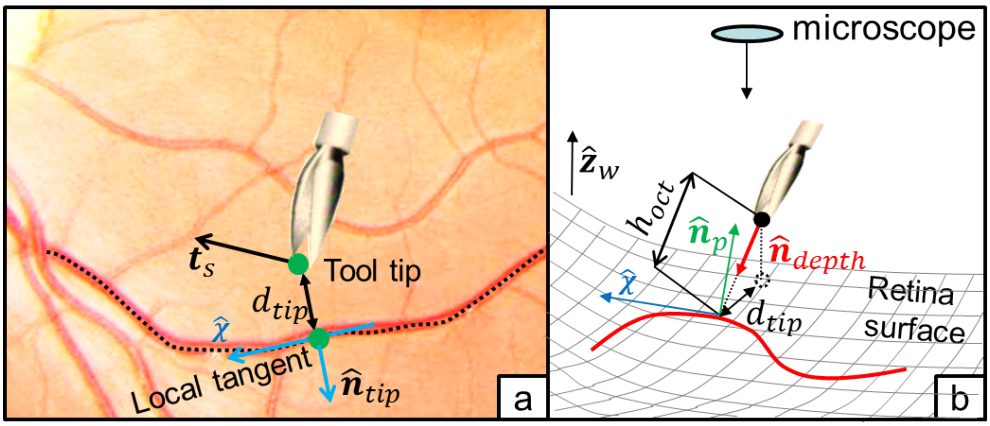

Figure 6.4: Microscope and OCT guided 3D virtual fixture law: (a) 2D microscope image based virtual fixture: the unconstrained slave twist will be projected along the local tangential direction and the velocity along $\hat{\mathbf{n}}_{tip}$ will be governed by the distance error d_{tip}. (b) OCT image based virtual fixture: the height from the tool tip to the retina surface or the vessel hole could be servoed for target tracking.

approximation to the affine transformation - especially when one deals with small motions typical of retinal procedures.

The 2D microscope-based VF law assists the user by applying an attractive field that brings the tool back to its intended path of motion (e.g. a blood vessel). The VF law (Fig. 6.4(a)) allows the surgeon to move freely along the blood vessel line while correcting the motion perpendicular to the blood vessel line with the tip offset d_{tip}. The microscope feedback information is sent by the Qt dialog through UDP packet to the telemanipulation slave robot controller. The UDP packet contains the gripper tip position ${}^{c}\mathbf{p}_{tip}$ and the unit vector pointing from the gripper tip to the closest point on the target curve ${}^{c}\hat{\mathbf{n}}_{tip}$ (the left superscript ^{c} indicates that these vectors are described in frame $\{\mathrm{c}\}$). In addition, the distance between the gripper tip and the closest point on the blood vessel d_{tip} is also included in the UDP packet. For example, these entities are shown in Fig. 6.3(d)). For brevity, we henceforth assume that all vectors have been transformed into a representation in frame $\{\mathrm{b}\}$ through the use of ${}^{b}\mathbf{R}_{c}$.

Let the symbol $\mathbf{t}$ be henceforth used for designating end effector twist such that the

linear velocity $\dot{\mathbf{x}}$ precedes the angular velocity $\boldsymbol{\omega}$ (i.e. $\mathbf{t} = \left[\dot{\mathbf{x}}^{\mathrm{T}}, \boldsymbol{\omega}^{\mathrm{T}}\right]^{\mathrm{T}}$. During telemanipulation, the twist of the telemanipulation master is designated $\mathbf{t}_m$. Similarly, the corresponding commanded slave robot twist is designated by $\mathbf{t}_s$. The twists $\mathbf{t}_m$ and $\mathbf{t}_s$ are typically related by a diagonal motion scaling matrix $\mathbf{m}_s \triangleq [diag\,(\mathbf{m}_{sx}, \mathbf{m}_{s\omega})]$ such that $\mathbf{t}_s = \mathbf{m}_s \mathbf{t}_m$.

The VF telemanipulation law relating $\mathbf{t}_m$ to $\mathbf{t}_s$ overrides the value of $\mathbf{t}_s$ and replaces it with a corrected value $\mathbf{t}'_s$. To accommodate direct image feedback for assisting the user to follow the path despite integration errors, a proportional velocity gain g_{image} having units of $mm/(sec * pixel)$ is used to relate the offset d_{tip} to a corrective translational speed bringing the tool tip back to the desired path. The following equation defines the VF for a planar curve:

$$\mathbf{t}'_s = \begin{bmatrix} \mathbf{m}_{sx}\left(\mathbf{I} - \hat{\mathbf{n}}_{tip}\hat{\mathbf{n}}_{tip}^{\mathrm{T}}\right) & \mathbf{0} \\ \mathbf{0} & \mathbf{m}_{s\omega} \end{bmatrix} \mathbf{t}_m + \begin{bmatrix} g_{image}\hat{\mathbf{n}}_{tip} \\ \mathbf{0} \end{bmatrix} d_{tip} \tag{6.6}$$

During telemanipulation, we found that using $\mathbf{m}_{s\omega} = \mathbf{I}$ is preferred by the users. Since our experiments were carried out in an agar open environment, we used $\mathbf{m}_{s\omega} = \mathbf{0}$ to enforce translational motion of the device so as to keep the OCT probe perpendicular to the mockup retina surface.

6.2.4 Real-time B-scan OCT Probe Based 3D Virtual Fixture

The OCT probe can image the retina within a small tilting range of $\approx 30^{\circ}$ relative to the local surface normal $\hat{\mathbf{n}}_p$ [254]. After fixing the position of the OCT probe with respect to the injection syringe, the real-time OCT images are acquired and segmented. The OCT VF law regulates the gripper velocity in the depth direction in a manner that does not violate the motion constrain specified by Eq. 6.6. A proportional gain g_{oct} is used to define corrective gripper velocity maintaining the tool at a desired distance h_{des} from the retina. This corrective velocity is proportional to the height difference between the desired height h_{des} and the measured height h_{oct}. Given the OCT depth direction $\hat{\mathbf{n}}_{depth}$ in robot frame

(Figure 6.4), g_{oct} is used to obtain a corrected gripper twist command $\mathbf{t}_s''$.

$$\mathbf{t}_s'' = \mathbf{t}_s' + \begin{bmatrix} g_{oct}\left(\hat{\mathbf{n}}_p^{\mathrm{T}}\hat{\mathbf{n}}_{depth}\right)\hat{\mathbf{n}}_p \\ \mathbf{0} \end{bmatrix} (h_{des} - h_{oct}) \tag{6.7}$$

The term $\left(\hat{\mathbf{n}}_p^{\mathrm{T}}\hat{\mathbf{n}}_{depth}\right)$ scales the proportional gain g_{oct} as a function of the OCT probe tilt relative to the local tissue normal $\hat{\mathbf{n}}_p$. Assuming that the world z-axis $\hat{\mathbf{z}}_w$ points upwards in the same hemisphere containing $\hat{\mathbf{n}}_p$, the estimate of $\hat{\mathbf{n}}_p$ is obtained using:

$$\hat{\mathbf{n}}_p \approx sgn\left(\left(\hat{\chi} \times \hat{\mathbf{n}}_{tip}\right)^{\mathrm{T}} \hat{\mathbf{z}}_w\right)\left(\hat{\chi} \times \hat{\mathbf{n}}_{tip}\right) \tag{6.8}$$

where $\hat{\chi}$ is a unit vector locally tangent to the desired gripper path, $\hat{\mathbf{n}}_{tip}$ is the unit vector pointing from the gripper's tip to the closest point on the desired gripper path. Both $\hat{\chi}$ and $\hat{\mathbf{n}}_{tip}$ are approximated using observations from the microscope.

6.3 Experimental Evaluation of Assistive Telemanipulation

The evaluation experiments presented herein aim to achieve three goals. The first goal is to characterize the expected control performance of our proposed system when using combined OCT and vision-based feedback. The second goal is to provide preliminary verification of the proposed approaches for VF as presented in section 6.2. The third goal is to demonstrate the feasibility of semi-automating sub-retinal injections.

The first evaluation experiment captures the performance of our system in automated tasks (i.e. without user input contaminating system performance) when using OCT feedback to control the distance of robot tip from a 3D surface. The experiment elucidates the effect of time lag in obtaining low-frequency OCT feedback. The second evaluation experiment demonstrates the VF law for following curves in 3D while evaluating tracking performance in the depth and lateral directions. Since the goal is to obtain preliminary verification, we limit the scope of this work to obtaining early evaluation with a single user. Finally, a third experiment is designed whereby the vision-based VF is used to control lat-

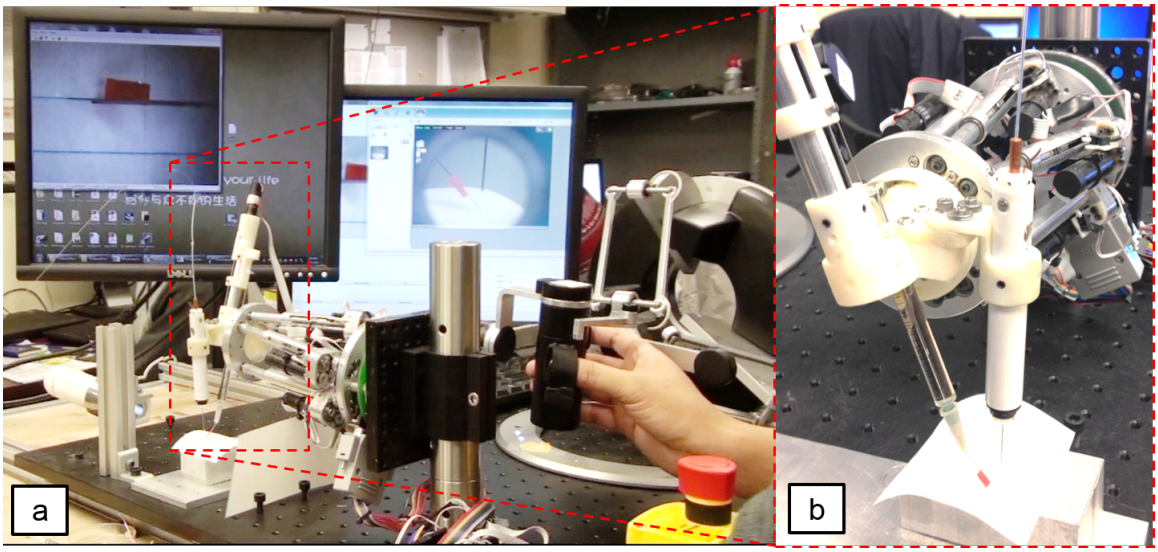

Figure 6.5: Experimental setup for assistive telemanipulation on tracking a curved line in space. (a) User telemanipulated the robotic manipulator under VF law. (b) The proposed robotic manipulator (Fig. 6.2) moved above a piece of bent paper

eral motion and OCT user feedback is used to assist the user in targeting a micro-pipette for a mockup sub-retinal injection.

Figure 6.5(a) shows the experimental setup. A rapid-prototyped adaptor was designed to align the OCT probe to image the tip of the end effector in a manner similar to Fig. 6.2. The end effector in the following experiments was either a thin wire or a micro-pipette tip. The experimental setup was used with the control and telemanipulation framework shown in Fig. 3.12. For experiments in sections 6.3.1 and 6.3.3 no telemanipulation was used.

6.3.1 Quantifying the Tracking Results in Depth Direction

In Figure 6.6(a), we set up the experiments to quantify the tracking accuracy in depth direction. The tracking surface was made from a rapid prototyped sinusoidal curve with a wavelength of 16mm and amplitude of 1.5mm. The robot was commanded to move one full cycle from left to right under different constant speed varying from 0.1 to 1.6 mm/s. Part 1 of the multimedia extension and Figure 6.6(a) show the post-segmented tip path under three different velocities. The tracking error was converted from the pixel error

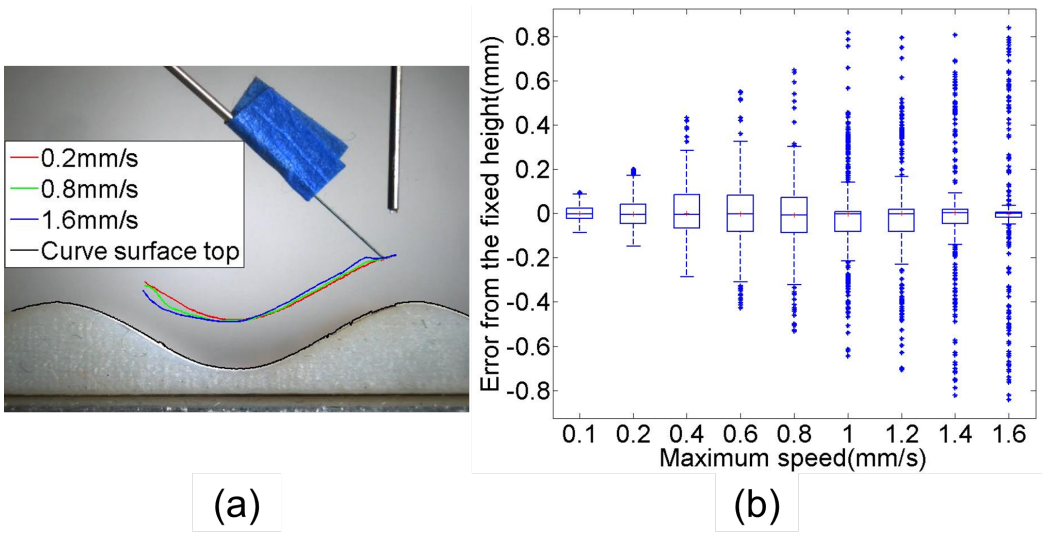

Figure 6.6: Experiment results of tracking a sinusoidal curve surface using only OCT feedback to quantify the tracking accuracy (Part 1 of multimedia extension). (a) Experimental setup of OCT probe and tool tip above the sinusoidal curve. Three tip paths represent a constant speed of 0.2mm/s, 0.8mm/s and 1.6mm/s. (b) Descriptive box plot of experimental results under different speeds.

measured by the real-time OCT stream with a scale acquired from the OCT calibration in the previous section. The error we present here is the real-time tracking error instead of a steady state error. Figure 6.6(b) shows the descriptive box plot of the experimental data under different speeds. The effect of the low OCT feedback rate can be seen clearly in figure 6.6 where tracking performance degrades as the tool tip horizontal speed is increased. With the robot moving around 0.1 mm/s, we could achieve a real-time maximum tracking error of $0.087mm$ and 25% quartile of $0.022mm$. We note that tool tip speeds of around $0.1mm/s$ were observed in [256]. Also, in [253] a hand-held micro-gripper with OCT control feedback for tremor cancellation in the depth direction demonstrated a tracking error of $0.350mm$ during grasp attempts. Although $0.087mm$ maximum tracking error is still large, we believe that further speedup of the OCT data acquisition rate from 5Hz to at least 30Hz will contribute to a significant improvement in tracking performance.

6.3.2 Evaluation of Assistive Telemanipulation for Tracking 3D Curves on a Surface

The task for this experiment was to trace a curve on a 3D surface while maintaining a fixed distance from a curved paper. While in the previous experiment the robot was commanded to move at a constant horizontal speed, in this experiment the robot was telemanipulated by a user. For example, Fig. 6.5(b) shows the task of following a curve on a bent paper.

During the experiment, the user telemanipulated the robot with an Omega-7® master device (Force-Dimension, Nyon Switzerland). More details on the telemanipulation framework are available in [228].

Part 2 of the multimedia extension and Figs. 6.7 (a) and (b) show the result of line tool tip tracking in top and side views. The top view was obtained using a boom microscope (Omano E-ZVU/V-15®) and the side view was provided by a Dino-Lite® microscope. The blue dots in the figures and multimedia extension show the tool tip motion trace.

The same experiment was repeated for following a 16 mm circle on a bent piece of paper. The experiment is shown in Part 3 of the multimedia extension and in Figs. 6.7 (c) and (d).

Finally, the experiment was also performed on a rubber eye model with painted blood vessel lines (GWB International®, 062411). These experiments are available in Part 4 of the multimedia extension and in Figs. 6.7 (e) and (f).

For the line experiment, 957 points were segmented along a single pass following the line. The mean tracking error was 0.073mm with a standard deviation of 0.052. The maximal error was 0.159mm. For the circle following experiment 10,150 points were segmented along multiple passes of the motion path and deviation of the tool tip from the circle was calculated also based on color-segmentation. The tracking error had a mean of 0.065mm, a standard deviation of 0.062mm and a maximal error of 0.300mm. For the mockup blood vessel tracking experiment, it is not easy to acquire a pixel to mm image scale. We segmented 6,002 data samples and the tracking pixel error had a mean of 3.4444 pixels, a

standard deviation of 1.9991 pixels and a maximal error of 10.9060 pixels.

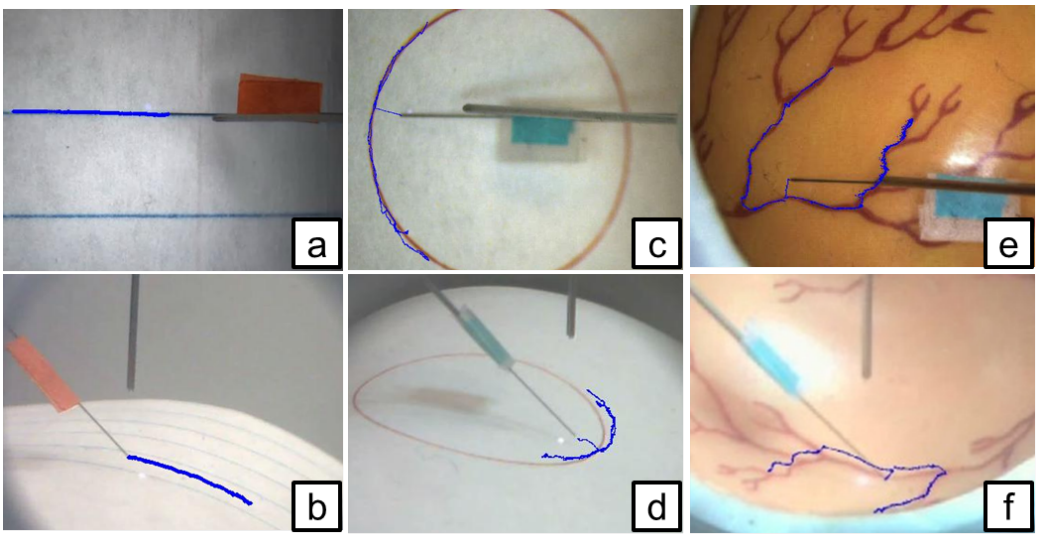

Figure 6.7: Experimental results for assistive telemanipulation on tracking 3D structures with microscope view on the top and side camera view on the bottom (Parts 2-4 of multimedia extension). (a)-(b) Tracking a line on a curved paper. (c)-(d) Tracking a circle on a curved paper. (e)-(f) Tracking phantom blood vessel on an eye model.

6.3.3 Semi-automated Micro-injection

Micro-injection into a $200\mu m$ phantom blood vessel channel embedded under an agar model was chosen to evaluate our VF law. Since our group is still developing segmentation algorithms for the B-mode OCT image, in this evaluation we only enabled the microscope-based VF and allowed the user to control the penetration depth. We adjusted the OCT probe scanning direction to be along the blood vessel line since, otherwise, the tool tip would always block the view beneath it. Initially, the robot was enabled with microscope based VF and the micro-pipette tip was automatically locked onto the phantom vessel. Then the user commanded the robot to move in depth direction to approach the phantom. Part 5 of the multimedia extension and Figure 6.8 show the steps of injection from the real-time B-mode OCT image stream. Once the tool tip was inserted into the phantom vessel, the injecting tool was actuated to deliver milk. The phantom vessel changed from empty to filled from Fig. 6.8(b) to (d).

With the microscope based VF enabled in this experiment, we could easily lock the tool tip onto the blood vessel. The same experiment was repeated four times by the same user. The microscope VF law successfully located the blood vessel every time and delivered the milk.

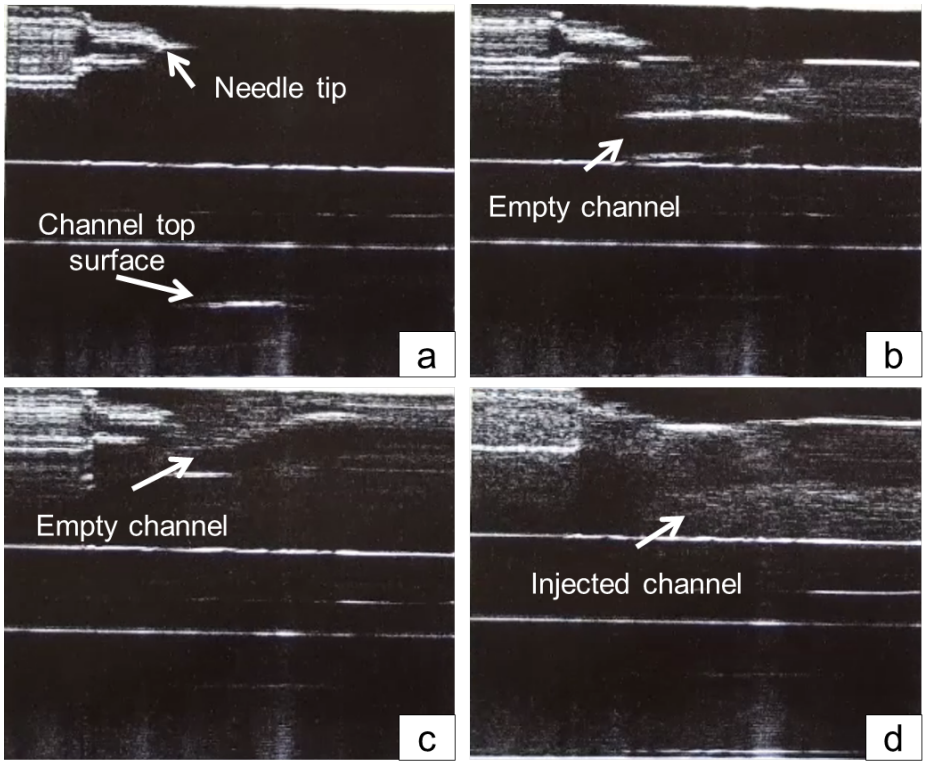

Figure 6.8: B-mode OCT images of injecting milk into phantom blood vessel (Part 5 of multimedia extension). (a) The micro-pipette tip location was fixed in the OCT image and the phantom blood vessel channel started to show while approaching. (b) The micro-pipette tip touched the top surface of the phantom and the phantom channel was empty with air. (c) The micro-pipette tip was inserted into the phantom vessel. (d) After injection, the micro-pipette tip left the phantom and the channel was filled with milk.

6.4 Conclusions

This chapter first introduces the telemanipulation integration architecture from the master device to the slave robot. It contains the design of an UDP protocol for communication between host and target computer, scaling down the motion, calculating the desired twist, a high level path planner and a low level PID controller.

Then we discussed the OCT and microscope combined 3D virtual fixture and its contribution to assistive telemanipulation. For 2D microscope based virtual fixture, the control law regulates the desired slave twist to be a projection speed onto the virtual fixture plane and a correction speed along the error direction from the tool tip to the target. When B-mode OCT image is introduced. The newly calculated twist is projected onto the perpendicular plane of the depth direction and the depth motion is servoed by the fixed distance from the tool tip to the object plane. Both microscope and OCT feedback is acquired at a dual rate discussed in Chapter 3.

Experiments have been conducted to track 3D curves such as line, circle on curved paper and artificial blood vessel in rubber eye model. We also carried out experiments on semi-automated micro-injection. The experiments show good tracking results and successful delivery of milk into phantom blood vessels. Statistical analysis was also performed on recorded tracking results. When the robot was commanded to follow a 3D surface while maintaining a fixed distance and moving at different horizontal speeds, the results showed that with increase of horizontal speed the tracking errors increased. However, the tracking errors for speeds typical of micro-surgical retinal tasks (usually around $0.1mm/s$) revealed maximal errors of less than 0.087 mm. We believe that increased OCT data acquisition frequency will result in further improved performance therefore our future work will focus on improvements of OCT probe internal actuation and data acquisition frequency.

The work proposed in this chapter has been accepted to a journal article [239] together with the OCT dewarping, OCT registration from Chapter 4 and the dual-rate visual servoing algorithm from Chapter 3.

Chapter 7

Conclusions

This dissertation has presented our efforts to design and integrate the first system with online OCT feedback for assistive robotic intervention in retinal surgery. In the course of achieving this goal, the dissertation has presented technological and theoretical contributions. The following is a summary of the contributions of this work, lessons learned and recommendations for future research and improvements.

The first theoretical contributions presented in this dissertation include a kinematic modeling framework for constrained telemanipulation. This kinematic framework builds on the earlier work of [4] and expands this work by adding a telemanipulation framework and redundancy resolution for supporting safe ocular and intraocular operations. This work is the first of its kind to offer a modeling framework enabling constrained telemanipulation of the eyeball with simultaneous intraocular manipulation capabilities.

In addition to the above contribution, we have presented a modeling framework for calibrating a partially constrained eyeball being manipulated by surgical tools subject to scleral incision constraints. The modeling framework takes into account limitations of the clinical setting and the types of measurements that may be obtained using existing technologies. Compared to prior works on estimation of instantaneous screw motion from velocity or position measurements (e.g. [241, 242]) the approach presented offers more robust calibration estimates. The orbital calibration approach presented allows the use of minute motions through a process of exploratory manipulation to discern the estimate of the center of rotation of the eye and the location of the incision points in the eye in each robot frame.

The problem of OCT image calibration and dewarping to support safe integration of OCT control feedback has guided our efforts in a new direction that has not been previ-

ously explored. To the best of our knowledge, this work presents the first adaptation of a thin plate spline interpolation algorithm for calibration and image dewarping and scaling. This approach allows for calibration of custom-made OCT probes that may have nonlinear behaviours due to actuation artifacts and optical artifacts in a manner that extends beyond previous works which typically focus on calibrating OCT probe intrinsics. We also presented several approaches for calibrating the OCT image plane in robot frame and in probe frame. The problem of automated hand-eye calibration of an OCT probe however remains challenging.

From the technological standpoint, the dissertation has presented a comprehensive system integration effort of a first system using online B-mode OCT feedback for retinal micro-surgery. This required addressing mechanical design issues, design of new actuators for microsurgery - including a new modular unit for intraocular dexterity. In addition, critical issues such as fabrication and calibration of parallel robots to achieve high level of performance as required by the surgical setting have been presented. At the system level, we have presented modifications of virtual fixture control laws to allow use of both B-mode OCT information and computer vision information. Although conceptually simple, these assistive virtual fixtures have proved to be indispensable for tasks such as micro blood vessel cannulation. To achieve this working telemanipulation system we have devised a multi-rate control approach that uses low rate feedback from the OCT probe and a high rate joint feedback for position control. This approach has been tested for automated surface tracking performance, despite slow OCT feedback rate. The OCT feedback control approach has also been verified for helping semi-automate injection in mockup retinal blood vessels.

In the course of our study, we have carried out an extensive experimental study for evaluating the value of each feedback or assistance modality during key retinal micro-surgery tasks. This evaluation included agar phantom models of the retina and enucleated goat eyes. In a first effort of its kind, we have shown that OCT visual feedback to the user

during approach tasks is key to improving task performance. However, when compared to robot assistance alone or robot and OCT feedback it was shown that robot and OCT feedback can significantly improves performance. This points to the need to continue efforts to merge these two co-dependent technologies to continue improving and expanding the repertoire of tasks that surgeons can carry out in microsurgery.

Recommendations for future research efforts for completing this effort include focus on the development of combined OCT probes and tools in a manner that extends the work of [255]. Other areas of research include the development of algorithms for hand-eye calibration of OCT probes. A recent progress by [257] for Ultrasound hand-eye calibration offers a theoretical solution that theoretically could work if one could make an imaging phantom small enough for an OCT setting. The approach however will suffer from scaling artifacts by which errors in fabricating the imaging phantom relative to the phantom size increase as the size of the phantom is decreased. We therefore believe the future research is warranted to offer additional solutions approaches to address this problem. Using the combined B-scan OCT probe and forceps [254] presented in Chapter 3 shall further strengthen the proposed assistive telemanipulation algorithm in Chapter 6. So far we have only proved the concept of OCT and microscope guided 3D virtual fixture in open environment. Preliminary results show the feasibility of semi-automated surgical interventions. Future work should repeat the invivo experiments using the OCT integrated gripper [254] and OCT integration needle [255].

BIBLIOGRAPHY

[1] Wei Wei, Roger Goldman, Nabil Simaan, Howard Fine, and Stanley Chang. Design and Theoretical Evaluation of Micro-Surgical Manipulators for Orbital Manipulation and Intraocular Dexterity, 2007.

[2] Koji Ikuta, Takashi Kato, and Satoru Nagata. Development and experimental verification of micro active forceps for microsurgery. pages 229–234, Nagoya, Jpn, 1996. IEEE, Piscataway, NJ, USA.

[3] Koji Ikuta, Takashi Kato, and Satoru Nagata. Micro active forceps with optical fiber scope for intra-ocular microsurgery. volume 1496, pages 456–461, San Diego, CA, USA, 1996. IEEE, Piscataway, NJ, USA.

[4] Wei Wei, Roger Goldman, Howard Fine, Stanley Chang, and Nabil Simaan. Design and Dexterity Evaluation for a Dual-Arm Micro-Surgical Robotic System for Orbital Manipulation and Intraocular Dexterity. *IEEE Transactions on Robotics*, 25(1):147–157, 2009.

[5] W Wei and N Simaan. Modeling, Force Sensing and Control of Flexible Cannulas for Micro-Stent Delivery. *ASME Journal of Dynamic Systems, Measurement, and Control*, in press, 2010.

[6] A Chatterjee, W G Ryan, and E S Rosen. Back pain in ophthalmologists. *Eye (London, England)*, 8 (Pt 4):473–4, January 1994.

[7] Jennifer A Sivak-Callcott, Sebastian R Diaz, Alan M Ducatman, Charles L Rosen, Ashish D Nimbarte, and Judith A Sedgeman. A survey study of occupational pain and injury in ophthalmic plastic surgeons. *Ophthalmic plastic and reconstructive surgery*, 27(1):28–32.

[8] R L McIntosh, Q Mohamed, S M Saw, and T Y Wong. Interventions for branch retinal vein occlusion: an evidence-based systematic review. *Ophthalmology*, 114(5):835–854, 2007.

[9] G T Frangieh, W R Green, E Barraquer-Somers, and D Finkelstein. Histopathologic study of nine branch retinal vein occlusions. *Arch Ophthalmol.*, 100(7):1132–1140, 1982.

[10] Anonymous. Argon laser photocoagulation for macular edema in branch vein occlusion. The Branch Vein Occlusion Study Group. *Am J Ophthalmol*, 98(3):271–82, 1984.

[11] VanVeldhuisen P C Oden N L Blodi B A Fisher M Chan C K Gonzalez V H Singerman L J Tolentino M; SCORE Study Research Group. Scott IU Ip MS. A randomized trial comparing the efficacy and safety of intravitreal triamcinolone with standard care to treat vision loss associated with macular Edema secondary to branch retinal vein occlusion: the Standard Care vs Corticosteroid for Retinal Vein Occlu. *Arch Ophthalmol*, 127(9):1115–1128, 2009.

[12] Irini P Chatziralli, Adil Jaulim, Vasileios G Peponis, Panagiotis G Mitropoulos, and Marilita M Moschos. Branch retinal vein occlusion: treatment modalities: an update of the literature. *Seminars in ophthalmology*, 29(2):85–107, mar 2014.

[13] Charles S Osterloh MD. Surgical decompression of branch retinal vein occlusions. *Arch Ophthalmol.*, 106(10):1469–1471, 1988.

[14] Bruce R A Opremcak EM. Surgical decompression of branch retinal vein occlusion via arteriovenous crossing sheathotomy: a prospective review of 15 cases. *Retina*, 19(1):1–5, 1999.

[15] J Mason, R Feist, m White, J Swanner, G McGwin, and T Emond. Sheathotomy to

decompress branch retinal vein occlusion: a matched control study. *Ophthalmology*, 111(3):540–545, 2004.

[16] U Mester and P Dillinger. Vitrectomy with arteriovenous decompression and internal limiting membrane dissection in branch retinal vein occlusion. *Retina*, 22(6):740–746, 2002.

[17] I K Oh, S Kim, J Oh, and K Huh. Long-term visual outcome of arteriovenous adventitial sheathotomy on branch retinal vein occlusion induced macular edema. *Korean J Ophthalmol*, 22(1):1–5, 2008.

[18] N Rodanant and S Tjoongsuwan. Sheathotomy without separation of venule overlying arteriole at occlusion site in uncommon branch retinal vein occlusion. *J Med Assoc Thai.*, 88(9):143–150, 2005.

[19] S Yamamoto, W Saito, F Tagi, S Takeuchi, E Sato, and S Mizunoya. Vitrectomy with or without arteriovenous adventitial sheathotomy for macular edema associated with branch retinal vein occlusion. *Am J Ophthalmol*, 138(6):907–914, 2004.

[20] J C Hwang, S K Gelman, H F Fine, S Chang, and L V Del Priore. Combined arteriovenous sheathotomy and intraoperative intravitreal triamcinolone acetonide for branch retinal vein occlusion. *Br J Ophthalmol*, 94(11):1483–1489, 2010.

[21] G K Shah. Adventitial sheathotomy for treatment of macular edema associated with branch retinal vein occlusion. *Curr Opin Ophthalmol*, 11(3):171–174, 2000.

[22] Shin Yamane, Motohiro Kamei, Susumu Sakimoto, Maiko Inoue, Akira Arakawa, Mihoko Suzuki, Nagakazu Matsumura, and Kazuaki Kadonosono. Matched control study of visual outcomes after arteriovenous sheathotomy for branch retinal vein occlusion. *Clinical ophthalmology (Auckland, N.Z.)*, 8:471–6, 2014.

[23] E J Chung, H Lee, and H J Koh. Arteriovenous crossing sheathotomy versus intravitreal triamcinolone acetonide injection for treatment of macular edema associated with branch retinal vein occlusion. *Graefes Arch Clin Exp Ophthalmol*, 246(7):967–974, 2008.

[24] W E Smiddy. Economic Considerations of Macular Edema Therapies. *Ophthalmology*, 2011.

[25] M T Cahil, P K Kaiser, J E Sears, and S Fekrat. The effect of arteriovenous sheathotomy on cystoid macular oedema secondary to branch retinal vein occlusion. *Br J Ophthalmol*, 87(11):1329–1332, 2003.

[26] Tamaki Y Ueta T, Yamaguchi Y, Shirakawa Y, Nakano T, Ideta R, Noda Y, Morita A, Mochizuki R, Sugita N, Mitsuishi M. Robot-assisted vitreoretinal surgery: development of a prototype and feasibility studies in an animal model. *Ophthalmology*, 116(8):1538–43, 1543.e1–2, 2009.

[27] Balicki M Koo J Iordachita I Mitchell B Handa J Hager G Taylor R Fleming I. Cooperative robot assistant for retinal microsurgery., 2008.

[28] P S Jensen, M R Glucksberg, J E Colgate, K W Grace, and R Attariwala. Robotic Micromanipulator for Ophthalmic Surgery. pages 204–210, Pittsburgh, 1994.

[29] Attariwala R Colgate J E Glucksberg M R Jensen PS Grace KW. Toward robot-assisted vascular microsurgery in the retina. *Graefes Arch Clin Exp Ophthalmol*, 235(11):696–701, 1997.

[30] National Eye Institute. Facts About Diabetic Eye Disease, 2015.

[31] Frank Tost, Robert Kempin, Rico Grossjohann, and Sabine Herfurth. [Diabetic retinopathy–Current aspects of therapy]. *Medizinische Monatsschrift fur Pharmazeuten*, 39(4):148–56; quiz 157–8, apr 2016.

[32] Fatih C Gundogan, Umit Yolcu, Fahrettin Akay, Abdullah Ilhan, Gokhan Ozge, and Salih Uzun. Diabetic Macular Edema. *Pakistan journal of medical sciences*, 32(2):505–10.

[33] Rishi P Singh, Karishma Habbu, Justis P Ehlers, M Cecilia Lansang, Lauren Hill, and Ivaylo Stoilov. The Impact of Systemic Factors on Clinical Response to Ranibizumab for Diabetic Macular Edema. *Ophthalmology*, may 2016.

[34] Eric L Ross, David W Hutton, Joshua D Stein, Neil M Bressler, Lee M Jampol, Adam R Glassman, and Diabetic Retinopathy Clinical Research Network. Cost-effectiveness of Aflibercept, Bevacizumab, and Ranibizumab for Diabetic Macular Edema Treatment: Analysis From the Diabetic Retinopathy Clinical Research Network Comparative Effectiveness Trial. *JAMA ophthalmology*, jun 2016.

[35] Quan Dong Nguyen, David M. Brown, Dennis M. Marcus, David S. Boyer, Sunil Patel, Leonard Feiner, Andrea Gibson, Judy Sy, Amy Chen Rundle, J. Jill Hopkins, Roman G. Rubio, and Jason S. Ehrlich. Ranibizumab for Diabetic Macular Edema. *Ophthalmology*, 119(4):789–801, apr 2012.

[36] Paul Mitchell, Francesco Bandello, Ursula Schmidt-Erfurth, Gabriele E. Lang, Pascale Massin, Reinier O. Schlingemann, Florian Sutter, Christian Simader, Gabriela Burian, Ortrud Gerstner, and Andreas Weichselberger. The RESTORE Study. *Ophthalmology*, 118(4):615–625, apr 2011.

[37] P. Massin, F. Bandello, J. G. Garweg, L. L. Hansen, S. P. Harding, M. Larsen, P. Mitchell, D. Sharp, U. E. K. Wolf-Schnurrbusch, M. Gekkieva, A. Weichselberger, and S. Wolf. Safety and Efficacy of Ranibizumab in Diabetic Macular Edema (RESOLVE Study): A 12-month, randomized, controlled, double-masked, multicenter phase II study. *Diabetes Care*, 33(11):2399–2405, nov 2010.

[38] David M. Brown, Quan Dong Nguyen, Dennis M. Marcus, David S. Boyer, Sunil

Patel, Leonard Feiner, Patricio G. Schlottmann, Amy Chen Rundle, Jiameng Zhang, Roman G. Rubio, Anthony P. Adamis, Jason S. Ehrlich, and J. Jill Hopkins. Long-term Outcomes of Ranibizumab Therapy for Diabetic Macular Edema: The 36-Month Results from Two Phase III Trials. *Ophthalmology*, 120(10):2013–2022, oct 2013.

[39] Jean-François Korobelnik, Frank G. Holz, Johann Roider, Yuichiro Ogura, Christian Simader, Ursula Schmidt-Erfurth, Katrin Lorenz, Miki Honda, Robert Vitti, Alyson J. Berliner, Florian Hiemeyer, Brigitte Stemper, Oliver Zeitz, and Rupert Sandbrink. Intravitreal Aflibercept Injection for Macular Edema Resulting from Central Retinal Vein Occlusion. *Ophthalmology*, 121(1):202–208, jan 2014.

[40] Francisco Rosa Stefanini, Emmerson Badaró, Paulo Falabella, Michael Koss, Michel Eid Farah, and Maurício Maia. Anti-VEGF for the management of diabetic macular edema. *Journal of immunology research*, 2014:632307, 2014.

[41] Photocoagulation for diabetic macular edema. Early Treatment Diabetic Retinopathy Study report number 1. Early Treatment Diabetic Retinopathy Study research group. *Archives of ophthalmology (Chicago, Ill. : 1960)*, 103(12):1796–806, dec 1985.

[42] Diabetic Retinopathy Clinical Research Network, Michael J Elman, Lloyd Paul Aiello, Roy W Beck, Neil M Bressler, Susan B Bressler, Allison R Edwards, Frederick L Ferris, Scott M Friedman, Adam R Glassman, Kellee M Miller, Ingrid U Scott, Cynthia R Stockdale, and Jennifer K Sun. Randomized trial evaluating ranibizumab plus prompt or deferred laser or triamcinolone plus prompt laser for diabetic macular edema. *Ophthalmology*, 117(6):1064–1077.e35, jun 2010.

[43] M L Laursen. Subthreshold micropulse diode laser treatment in diabetic macular oedema. *British Journal of Ophthalmology*, 88(9):1173–1179, sep 2004.

[44] G W Blankenship. Diabetic macular edema and argon laser photocoagulation: a prospective randomized study. *Ophthalmology*, 86(1):69–78, jan 1979.

[45] Treatment Techniques and Clinical Guidelines for Photocoagulation of Diabetic Macular Edema. *Ophthalmology*, 94(7):761–774, jul 1987.

[46] Giuseppe Querques, Fatemeh Darvizeh, Lea Querques, Vittorio Capuano, Francesco Bandello, and Eric H Souied. Assessment of the Real-Life Usage of Intravitreal Dexamethasone Implant in the Treatment of Chronic Diabetic Macular Edema in France. *Journal of ocular pharmacology and therapeutics : the official journal of the Association for Ocular Pharmacology and Therapeutics*, jun 2016.

[47] J Chhablani, P Bansal, D Veritti, S Sambhana, V Sarao, F Pichi, P Carrai, D Massaro, A Lembo, A M Mansour, A Banker, S R Gupta, R Hamam, and P Lanzetta. Dexamethasone implant in diabetic macular edema in real-life situations. *Eye (London, England)*, 30(3):426–30, mar 2016.

[48] Yit Yang, Clare Bailey, Anat Loewenstein, and Pascale Massin. INTRAVITREAL CORTICOSTEROIDS IN DIABETIC MACULAR EDEMA: PHARMACOKINETIC CONSIDERATIONS. *Retina (Philadelphia, Pa.)*, 35(12):2440–9, dec 2015.

[49] Alejandra Daruich, Alexandre Matet, and Francine Behar-Cohen. Sustained-release steroids for the treatment of diabetic macular edema. *Current diabetes reports*, 15(11):99, nov 2015.

[50] Michael A. Singer, Daniel S. Kermany, Jana Waters, Michael E. Jansen, and Lyndon Tyler. Diabetic macular edema: it is more than just VEGF. *F1000Research*, 5:1019, may 2016.

[51] Christos Haritoglou, Wolfgang Mayer, and Armin Wolf. Fluocinolone acetonide for

the treatment of diabetic macular edema. *Expert review of clinical pharmacology*, 9(3):367–74, mar 2016.

[52] Masumi G Asahi, Gabriela L Bobarnac Dogaru, Spencer M Onishi, and Ron P Gallemore. Strong topical steroid, NSAID, and carbonic anhydrase inhibitor cocktail for treatment of cystoid macular edema. *International medical case reports journal*, 8:305–12, 2015.

[53] Jennifer R Evans, Manuele Michelessi, and Gianni Virgili. Laser photocoagulation for proliferative diabetic retinopathy. *The Cochrane database of systematic reviews*, (11):CD011234, 2014.

[54] A Ambresin, V Strueven, and J-A C Pournaras. Painless indirect argon laser in high risk proliferative diabetic retinopathy. *Klinische Monatsblatter fur Augenheilkunde*, 232(4):509–13, apr 2015.

[55] É M Kasimov, N I Alieva, and A N Mamedzade. [Results of YAG-laser vitreolysis in proliferative diabetic retinopathy complicated by vitreous hemorrhage]. *Vestnik oftalmologii*, 130(4):22–6.

[56] Jay Chhablani, Sarita Sambhana, Annie Mathai, Vishali Gupta, J Fernando Arevalo, and Igor Kozak. Clinical efficacy of navigated panretinal photocoagulation in proliferative diabetic retinopathy. *American journal of ophthalmology*, 159(5):884–9, may 2015.

[57] Tarek Alasil and Nadia K Waheed. Pan retinal photocoagulation for proliferative diabetic retinopathy: pattern scan laser versus argon laser. *Current opinion in ophthalmology*, 25(3):164–70, may 2014.

[58] Recep Göktu Seymenolu, Mahmut Ouz Ulusoy, and Esin Fatma Baer. Safety and efficacy of panretinal photocoagulation in patients with high-risk proliferative diabetic

retinopathy using pattern scan laser versus conventional YAG laser. *The Kaohsiung journal of medical sciences*, 32(1):22–6, jan 2016.

[59] Samuel H Yun and Ron A Adelman. Recent developments in laser treatment of diabetic retinopathy. *Middle East African journal of ophthalmology*, 22(2):157–63.

[60] P Osaadon, X J Fagan, T Lifshitz, and J Levy. A review of anti-VEGF agents for proliferative diabetic retinopathy. *Eye (London, England)*, 28(5):510–20, may 2014.

[61] National Eye Institute. Facts About Macular Hole, 2012.

[62] Colin A McCannel, Jennifer L Ensminger, Nancy N Diehl, and David N Hodge. Population-based incidence of macular holes. *Ophthalmology*, 116(7):1366–9, jul 2009.

[63] Andrea Maria Coppé, Guido Ripandelli, Vincenzo Parisi, Monica Varano, and Mario Stirpe. Prevalence of asymptomatic macular holes in highly myopic eyes. *Ophthalmology*, 112(12):2103–9, dec 2005.

[64] Wendel R T Kelly NE. Vitreous surgery for idiopathic macular holes: results of a pilot study. *Arch Ophthalmol*, 109(5):654–659, 1991.

[65] G A Williams. Macular holes: the latest in current management. *Retina*, 26(6 Suppl:S9–12, 2006.

[66] H L Brooks. Macular hole surgery with and without internal limiting membrane peeling. *Ophthalmology*, 107(10):1939–48; discussion 1948–9, oct 2000.

[67] D W Park, J O Sipperley, S R Sneed, P U Dugel, and J Jacobsen. Macular hole surgery with internal-limiting membrane peeling and intravitreous air. *Ophthalmology*, 106(7):1392–7; discussion 1397–8, jul 1999.

[68] R R Margherio, A R Margherio, G A Williams, D R Chow, and M J Banach. Effect of perifoveal tissue dissection in the management of acute idiopathic full-thickness

macular holes. *Archives of ophthalmology (Chicago, Ill. : 1960)*, 118(4):495–8, apr 2000.

[69] A P Da Mata, S E Burk, C D Riemann, R H Rosa, M E Snyder, M R Petersen, and R E Foster. Indocyanine green-assisted peeling of the retinal internal limiting membrane during vitrectomy surgery for macular hole repair. *Ophthalmology*, 108(7):1187–92, jul 2001.

[70] Tom G Sheidow, Kevin J Blinder, Nancy Holekamp, Daniel Joseph, Gaurav Shah, M Gilbert Grand, Mathew A Thomas, Jeff Bakal, and Sanjay Sharma. Outcome results in macular hole surgery: an evaluation of internal limiting membrane peeling with and without indocyanine green. *Ophthalmology*, 110(9):1697–701, sep 2003.

[71] Schaumberger M Gass C A Priglinger S G Kampik A Haritoglou C Reiniger IW. Five-year follow-up of macular hole surgery with peeling of the internal limiting membrane: update of a prospective study. *Retina.*, 26(6):618–622, 2006.

[72] Sneed S R Dugel P U Jacobsen J Park DW Sipperley JO. Macular hole surgery with internal-limiting membrane peeling and intravitreous air. *Ophthalmology.*, 106(7):1392–1397, 1999.

[73] Cordahi G Smiddy WE Feuer W. Internal limiting membrane peeling in macular hole surgery. *Ophthalmology.*, 108(8):1471–1476, 2001.

[74] A K H Kwok, T Y Y Lai, and V W Y Wong. Idiopathic macular hole surgery in Chinese patients: a randomised study to compare indocyanine green-assisted internal limiting membrane peeling with no internal limiting membrane peeling. *Hong Kong medical journal = Xianggang yi xue za zhi / Hong Kong Academy of Medicine*, 11(4):259–66, aug 2005.

[75] U C Christensen, K Krøyer, B Sander, M Larsen, V Henning, J Villumsen, and M la Cour. Value of internal limiting membrane peeling in surgery for idiopathic

macular hole stage 2 and 3: a randomised clinical trial. *The British journal of ophthalmology*, 93(8):1005–15, aug 2009.

[76] Noemi Lois, Jennifer Burr, John Norrie, Luke Vale, Jonathan Cook, Alison McDonald, and Full-Thickness Macular Hole and Internal Limiting Membrane Peeling Study (FILMS) Group. Clinical and cost-effectiveness of internal limiting membrane peeling for patients with idiopathic full thickness macular hole. Protocol for a randomised controlled trial: FILMS (Full-thickness Macular Hole and Internal Limiting Membrane Peeling Study). *Trials*, 9:61, 2008.

[77] Laura Ternent, Luke Vale, Charles Boachie, Jennifer M Burr, Noemi Lois, and Full-Thickness Macular Hole and Internal Limiting Membrane Peeling Study (FILMS) Group. Cost-effectiveness of internal limiting membrane peeling versus no peeling for patients with an idiopathic full-thickness macular hole: results from a randomised controlled trial. *The British journal of ophthalmology*, 96(3):438–43, mar 2012.

[78] R. Tadayoni, C. Creuzot-Garcher, J. F. Korobelnik, and Et Al. internal limiting membrane peeling for larger macular holes: a randomized, multicentric and controlled clinical trial. In *ARVO Meeting Abstracts*, 2009.

[79] Kurt Spiteri Cornish, Noemi Lois, Neil W Scott, Jennifer Burr, Jonathan Cook, Charles Boachie, Ramin Tadayoni, Morten la Cour, Ulrik Christensen, and Alvin K H Kwok. Vitrectomy with internal limiting membrane peeling versus no peeling for idiopathic full-thickness macular hole. *Ophthalmology*, 121(3):649–55, mar 2014.

[80] Hirabayashi Y Shimada S Ogura Y Matsunaga N Ozeki H. Histopathologic evaluation of the internal limiting membrane surgically excised from eyes with diabetic maculopathy. *Retina*, 25(3):311–316, 2005.

[81] Eduardo Dib, Eduardo Büchelle Rodrigues, Maurício Maia, Carsten H Meyer, Fernando Marcondes Penha, Bruno de Albuquerque Furlani, Elaine de Paula Fiod Costa, and Michel Eid Farah. Vital dyes in chromovitrectomy. *Arquivos brasileiros de oftalmologia*, 72(6):845–50.

[82] M Kernt, C Hirneiss, A Wolf, R Liegi, J Rueping, A Neubauer, C Alge, M Ulbig, A Gandorfer, A Kampik, and C Haritoglou. Indocyanine green increases light-induced oxidative stress, senescence, and matrix metalloproteinases 1 and 3 in human RPE cells. *Acta Ophthalmol*, Jul, 2010.

[83] C Haritoglou, C A Gass, M Schaumberger, O Ehrt, A Gandorfer, and A Kampik. Macular changes after peeling of the internal limiting membrane in macular hole surgery. *American journal of ophthalmology*, 132(3):363–8, sep 2001.

[84] P B Henrich, S G Priglinger, C Haritoglou, T Josifova, P R Ferreira, R W Strauss, J Flammer, and P C Cattin. Quantification of Contrast Recognizability During Brilliant Blue G (BBG) and Indocyanine Green (ICG) Assisted Chromovitrectomy. *Invest Ophthalmol Vis Sci.*, 2011.

[85] R G Michels. Vitreous surgery for macular pucker. *American journal of ophthalmology*, 92(5):628–39, nov 1981.

[86] S de Bustros, J T Thompson, R G Michels, T A Rice, and B M Glaser. Vitrectomy for idiopathic epiretinal membranes causing macular pucker. *British Journal of Ophthalmology*, 72(9):692–695, sep 1988.

[87] Jason R. Wilkins, Carmen a. Puliafito, Michael R. Hee, Jay S. Duker, Elias Reichel, Jeffery G. Coker, Joel S. Schuman, Eric a. Swanson, and James G. Fujimoto. Characterization of epiretinal membranes using optical coherence tomography. *Ophthalmology*, 103(12):2142–51, December 1996.

[88] National Eye Institute. Macular Pucker, 2012.

[89] ANTON HAAS, GERALD SEIDEL, IRIS STEINBRUGGER, RICHARD MAIER, VANESSA GASSER-STEINER, ANDREAS WEDRICH, and MARTIN WEGER. TWENTY-THREE-GAUGE AND 20-GAUGE VITRECTOMY IN EPIRETINAL MEMBRANE SURGERY. *Retina*, 30(1):112–116, jan 2010.

[90] Jongshin Kim, Kyoung Min Rhee, Se Joon Woo, Young Suk Yu, Hum Chung, and Kyu Hyung Park. Long-term Temporal Changes of Macular Thickness and Visual Outcome after Vitrectomy for Idiopathic Epiretinal Membrane. *American Journal of Ophthalmology*, 150(5):701–709.e1, nov 2010.

[91] Fumiki Okamoto, Yoshifumi Okamoto, Takahiro Hiraoka, and Tetsuro Oshika. Effect of Vitrectomy for Epiretinal Membrane on Visual Function and Vision-Related Quality of Life. *American Journal of Ophthalmology*, 147(5):869–874.e1, may 2009.

[92] R Grewing and U Mester. Results of surgery for epiretinal membranes and their recurrences. *British Journal of Ophthalmology*, 80(4):323–326, apr 1996.

[93] Stanley Chang, Emily M Gregory-Roberts, Sungpyo Park, Ketan Laud, Scott D Smith, and Quan V Hoang. Double peeling during vitrectomy for macular pucker: the Charles L. Schepens Lecture. *JAMA ophthalmology*, 131(4):525–30, apr 2013.

[94] Hiroyuki Shimada, Hiroyuki Nakashizuka, Takayuki Hattori, Ryusaburo Mori, Yoshihiro Mizutani, and Mitsuko Yuzawa. Double Staining with Brilliant Blue G and Double Peeling for Epiretinal Membranes. *Ophthalmology*, 116(7):1370–1376, jul 2009.

[95] The Retina Society Terminology Committee. The classification of retinal detachment with proliferative vitreoretinopathy. *Ophthalmology*, 90(2):121–5, feb 1983.

[96] Gian Paolo Giuliari and Sadaka. Proliferative vitreoretinopathy: current and emerging treatments. *Clinical Ophthalmology*, page 1325, aug 2012.

[97] W F Rachal and T C Burton. Changing concepts of failures after retinal detachment surgery. *Archives of ophthalmology (Chicago, Ill. : 1960)*, 97(3):480–3, mar 1979.

[98] A H Chignell, L G Fison, E W Davies, R E Hartley, and M F Gundry. Failure in retinal detachment surgery. *Modern problems in ophthalmology*, 12:20–8, 1974.

[99] H Heimann, X Zou, C Jandeck, U Kellner, N E Bechrakis, K M Kreusel, H Helbig, L Krause, A Schuler, N Bornfeld, and M H Foerster. Primary vitrectomy for rhegmatogenous retinal detachment: an analysis of 512 cases. *Graefes Arch Clin Exp Ophthalmol.*, 244(1):69–78, 2006.

[100] R G Michels. Surgery of retinal detachment with proliferative vitreoretinopathy. *Retina*, 4:63–83, 1984.

[101] D G Charteris. Proliferative vitreoretinopathy: pathobiology, surgical management, and adjunctive treatment. *The British journal of ophthalmology*, 79(10):953–60, oct 1995.

[102] J.Carlos Pastor. Proliferative Vitreoretinopathy. *Survey of Ophthalmology*, 43(1):3–18, jul 1998.

[103] S J Ryan. Traction retinal detachment. XLIX Edward Jackson Memorial Lecture. *American journal of ophthalmology*, 115(1):1–20, jan 1993.

[104] Kenneth W Grace, Patrick Jensen, J Edward Colgate, and Matthew Glucksberg. Teleoperation for ophthalmic surgery: From the Eye Robot to feature extracting force feedback . 16(4):293–310, 1998.

[105] Hari Das, Haya Zak, Jason Johnson, John Crouch, and Don Frambach. Evaluation of A Telerobotic System to Assist Surgeons in Microsurgery. *Computer Aided Surgery*, 4(1):15–25, 1999.

[106] Russell Taylor, Pat Jensen, Louis Whitcomb, Aaron Barnes, Rajesh Kumar, Dan Stoianovici, Puneet Gupta, ZhengXian Wang, Eugene DeJuan, and Louis Kavoussi. Steady-hand robotic system for microsurgical augmentation. *International Journal of Robotics Research*, 18(12):1201–1210, 1999.

[107] Cameron N Riviere, Wei Tech Ang, and Pradeep K Khosla. Toward Active Tremor Canceling in Handheld Microsurgical Instruments. *IEEE Trans. on Robotics and Automation*, 19(5):793–800, 2003.

[108] T Nakano, N Sugita, T Ueta, Y Tamaki, and Mitsuishi M. A parallel robot to assist vitreoretinal surgery. *Int J Comput Assist Radiol Surg.*, 4(6):517–526, 2009.

[109] A. Bettini, S. Lang, A. Okamura, and G. Hager. Vision assisted control for manipulation using virtual fixtures: experiments at macro and micro scales. In *Proceedings 2002 IEEE International Conference on Robotics and Automation (Cat. No.02CH37292)*, volume 4, pages 3354–3361. IEEE, 2002.

[110] Brian C Becker, Robert A Maclachlan, Louis A Lobes, Gregory D Hager, and Cameron N Riviere. Vision-Based Control of a Handheld Surgical Micromanipulator with Virtual Fixtures. *IEEE transactions on robotics : a publication of the IEEE Robotics and Automation Society*, 29(3):674–683, February 2013.

[111] W Wei, C Popplewell, H Fine, S Chang, and N Simaan. Enabling Technology for Micro-Vascular Stenting in Ophthalmic Surgery. *ASME Journal of Medical Devices (JMED*, 4 (to appe(2), 2010.

[112] B C Becker, R A MacLachlan, L A Lobes, and C N Riviere. Semiautomated intraocular laser surgery using handheld instruments. *Lasers Surg Med*, 42(3):264–273, 2010.

[113] Yasuo Noda, Yoshiki Ida, Shinichi Tanaka, Taku Toyama, Murilo Felix Roggia, Yasuhiro Tamaki, Naohiko Sugita, Mamoru Mitsuishi, and Takashi Ueta. Impact

of robotic assistance on precision of vitreoretinal surgical procedures. *PloS one*, 8(1):e54116, January 2013.

[114] Maneesh Dewan, Panadda Marayong, Allison M Okamura, and Gregory D Hager. Vision-based assistance for ophthalmic micro-surgery. volume 3217 of *Lecture Notes in Computer Science*, page 49, Saint-Malo, France, 2004. Springer Verlag, Heidelberg, D-69121, Germany.

[115] Brian C Becker, Sungwook Yang, Robert A Maclachlan, and Cameron N Riviere. Towards Vision-Based Control of a Handheld Micromanipulator for Retinal Cannulation in an Eyeball Phantom. In *Fourth IEEE RAS/EMBS International Conference on Biomedical Robotics and Biomechatronics (BIOROB)*, number c, pages 44–49, 2012.

[116] A Bettini, P Marayong, S Lang, A M Okamura, and G D Hager. Vision Assisted Control for Manipulation Using Virtual Fixtures. *IEEE Transactions on Robotics,*, 20(6):953–966, 2004.

[117] Marcin Balicki et al. Micro-force Sensing in Robot Assisted Membrane Peeling for Vitreoretinal Surgery. In *Proc. Med. Image. Comput. Comput. Assist. Interv.*, volume LNCS 6363, pages 303–310, Beijing, 2010. Springer.

[118] W Wei, C Popplewell, H Fine, S Chang, and N Simaan. Enabling Technology for Micro-Vascular Stenting in Ophthalmic Surgery. *ASME JMED*, 4(2):014503, 2010.

[119] W Wei and N Simaan. Modeling, Force Sensing and Control of Flexible Cannulas for Micro-Stent Delivery. *ASME Journal of Dynamic Systems, Measurement, and Control*, Under revi, 2010.

[120] C T Dotter and M P Judkins. Transluminal Treatment of Arteriosclerotic Obstruction, Description of A New Technic and a Preliminary Report of Its Application. *Circulation*, 30(5):654–670, 1964.

[121] G Lim and et Al. Future of active catheters. 56:113–121, 1996.

[122] Samad Hayati. Robot arm geometric link parameter estimation. In *The 22nd IEEE Conference on Decision and Control*, pages 1477–1483. IEEE, 1983.

[123] Hanqi Zhuang, Luke K Wang, and Zvi S. Roth. Error-model-based robot calibration using a modified CPC model. *Robotics and Computer-Integrated Manufacturing*, 10(4):287–299, August 1993.

[124] G. Yang and I.-M. Chen. A novel kinematic calibration algorithm for reconfigurable robotic systems. In *Proceedings of International Conference on Robotics and Automation*, volume 4, pages 3197–3202. IEEE, 1997.

[125] Haruka Kikuchi, Yusuke Maeda, Masao Sugi, and Tamio Arai. Automatic calibration of assembly robots for instantaneous installation 'plug and produce'. *Advanced Robotics*, pages 41–52, 2003.

[126] Ali Nahvi, John M Hollerbach, and Vincent Hayward. Calibration of a Parallel Robot Using Multiple Kinematic Closed. pages 407–412, 1994.

[127] Hanqi Zhuang. Self-calibration of parallel mechanisms with a case study on Stewart platforms. *IEEE Transactions on Robotics and Automation*, 13(3):387–397, June 1997.

[128] W. Khalil and S. Besnard. Self calibration of Stewart-Gough parallel robots without extra sensors. *IEEE Transactions on Robotics and Automation*, 15(6):1116–1121, 1999.

[129] Pouya N Dayani, Ramiro Maldonado, Sina Farsiu, and Cynthia A Toth. Intraoperative use of handheld spectral domain optical coherence tomography imaging in macular surgery. *Retina (Philadelphia, Pa.)*, 29(10):1457–68, 2009.

[130] Susanne Binder, Christiane I Falkner-Radler, Christoph Hauger, Holger Matz, and Carl Glittenberg. Feasibility of intrasurgical spectral-domain optical coherence tomography. *Retina (Philadelphia, Pa.)*, 31(7):1332–6, 2011.

[131] Justis P Ehlers, Yuankai K Tao, and Sunil K Srivastava. The value of intraoperative optical coherence tomography imaging in vitreoretinal surgery. *Current opinion in ophthalmology*, 25(3):221–7, May 2014.

[132] Justis P Ehlers, Tiffany Tam, Peter K Kaiser, Daniel F Martin, Gina M Smith, and Sunil K Srivastava. Utility of intraoperative optical coherence tomography during vitrectomy surgery for vitreomacular traction syndrome. *Retina (Philadelphia, Pa.)*, 34(7):1341–6, July 2014.

[133] Arghavan Almony, Eric Nudleman, Gaurav K Shah, Kevin J Blinder, Dean B Eliott, Robert A Mittra, and Asheesh Tewari. Techniques, rationale, and outcomes of internal limiting membrane peeling. *Retina (Philadelphia, Pa.)*, 32(5):877–91, May 2012.

[134] Cristian Carpentier, Mario Zanolli, Lihteh Wu, Gonzalo Sepulveda, Maria H Berrocal, Mario Saravia, Manuel Diaz-Llopis, Roberto Gallego-Pinazo, Luis Filsecker, Juan I Verdaguer-Diaz, Rodrigo Milan-Navarro, J Fernando Arevalo, and Mauricio Maia. Residual internal limiting membrane after epiretinal membrane peeling: results of the Pan-American Collaborative Retina Study Group. *Retina (Philadelphia, Pa.)*, 33(10):2026–31, 2013.

[135] Changho Lee, Kyungun Kim, Seunghoon Han, Sehui Kim, Jun Hoon Lee, Hong Kyun Kim, Chulhong Kim, Woonggyu Jung, and Jeehyun Kim. Stimulated penetrating keratoplasty using real-time virtual intraoperative surgical optical coherence tomography. *Journal of biomedical optics*, 19(3):30502, March 2014.

[136] Justis P Ehlers, Yuankai K Tao, Sina Farsiu, Ramiro Maldonado, Joseph A Izatt,

and Cynthia A Toth. Visualization of real-time intraoperative maneuvers with a microscope-mounted spectral domain optical coherence tomography system. *Retina (Philadelphia, Pa.)*, 33(1):232–6, January 2013.

[137] Paul Hahn, Justin Migacz, Rachelle O'Donnell, Shelley Day, Annie Lee, Phoebe Lin, Robin Vann, Anthony Kuo, Sharon Fekrat, Prithvi Mruthyunjaya, Eric A Postel, Joseph A Izatt, and Cynthia A Toth. Preclinical evaluation and intraoperative human retinal imaging with a high-resolution microscope-integrated spectral domain optical coherence tomography device. *Retina*, 33(7):1328–37, 2013.

[138] Yuankai K Tao, Sunil K Srivastava, and Justis P Ehlers. Microscope-integrated intraoperative OCT with electrically tunable focus and heads-up display for imaging of ophthalmic surgical maneuvers. *Biomedical optics express*, 5(6):1877–85, June 2014.

[139] Justis P Ehlers, Sunil K Srivastava, Daniel Feiler, Amanda I Noonan, Andrew M Rollins, and Yuankai K Tao. Integrative advances for OCT-guided ophthalmic surgery and intraoperative OCT: microscope integration, surgical instrumentation, and heads-up display surgeon feedback. *PloS one*, 9(8):e105224, January 2014.

[140] Jin U Kang, Yong Huang, Kang Zhang, Zuhaib Ibrahim, Jaepyeong Cha, W P Andrew Lee, Gerald Brandacher, and Peter L Gehlbach. Real-time three-dimensional Fourier-domain optical coherence tomography video image guided microsurgeries. *Journal of biomedical optics*, 17(8):081403–1, August 2012.

[141] Martin F Kraus, Jonathan J Liu, Julia Schottenhamml, Chieh-Li Chen, Attila Budai, Lauren Branchini, Tony Ko, Hiroshi Ishikawa, Gadi Wollstein, Joel Schuman, Jay S Duker, James G Fujimoto, and Joachim Hornegger. Quantitative 3D-OCT motion correction with tilt and illumination correction, robust similarity measure and regularization. *Biomedical optics express*, 5(8):2591–613, August 2014.

[142] Justis P Ehlers, Yuankai K Tao, Sina Farsiu, Ramiro Maldonado, Joseph A Izatt, and Cynthia A Toth. Integration of a spectral domain optical coherence tomography system into a surgical microscope for intraoperative imaging. *Investigative ophthalmology & visual science*, 52(6):3153–9, May 2011.

[143] Paul Hahn, Justin Migacz, Rachelle O'Connell, Ramiro S Maldonado, Joseph A Izatt, and Cynthia A Toth. The use of optical coherence tomography in intraoperative ophthalmic imaging. *Ophthalmic surgery, lasers & imaging : the official journal of the International Society for Imaging in the Eye*, 42 Suppl:S85–94, July 2011.

[144] Justis P Ehlers, Stephen A McNutt, Peter K Kaiser, and Sunil K Srivastava. Contrast-enhanced intraoperative optical coherence tomography. *The British journal of ophthalmology*, 97(11):1384–6, November 2013.

[145] Matthew T Witmer, George Parlitsis, Sarju Patel, and Szilárd Kiss. Comparison of ultra-widefield fluorescein angiography with the Heidelberg Spectralis() noncontact ultra-widefield module versus the Optos() Optomap(). *Clinical ophthalmology (Auckland, N.Z.)*, 7:389–94, January 2013.

[146] Daniel E Croft, Jano van Hemert, Charles C Wykoff, David Clifton, Michael Verhoek, Alan Fleming, and David M Brown. Precise montaging and metric quantification of retinal surface area from ultra-widefield fundus photography and fluorescein angiography. *Ophthalmic surgery, lasers & imaging retina*, 45(4):312–7, 2014.

[147] A F Low, G J Tearney, B E Bouma, and I K Jang. Technology insight: Optical coherence tomography current status and future development. *Nature Clinical Practice Cardiovascular Medicine*, 3(3):154–162, 2006.

[148] M Kawasaki, B E Bouma, J Bressner, S L Houser, S K Nadkarni, B D McNeill, I K Jang, H Fujiwara, and G J Tearney. Diagnostic accuracy of optical coherence tomography and integrated backscatter intravascular ultrasound images for tissue

characterization of human coronary plaques. *Journal of the American College of Cardiology*, 48(1):81–88, 2006.

[149] M S Jafri, R Tang, and C M Tang. Optical coherence tomography guided neurosurgical procedures in small rodents. *J Neurosci Methods*, 176(2):85–95, 2008.

[150] D E Vokes, R Jackson, S Guo, K A Perez, K Su, J M Ridgway, W B Armstrong, Z Chen, and B K Wong. Optical coherence tomography-enhanced microlaryngoscopy: preliminary report of a noncontact optical coherence tomography system integrated with a surgical microscope. *Ann Otol Rhinol Laryngol*, 117:538–547, 2008.

[151] Y Pan, T Q Xie, C W Du, S Bastacky, S Meyers, and M L Zeidel. Enhancing early bladder cancer detection with fluorescence-guided endoscopic optical coherence tomography. *Optics Letters*, 28(24):2484–2487, 2003.

[152] A Jain, A Kopa, Y Pan, G K Fedder, and H Xie. A two-axis electrothermal micromirror for endoscopic optical coherence tomography. *IEEE J Select Top Quant Electron*, 10(3):636–642, 2004.

[153] S A Boppart, B E Bouma, C Pitris, G J Tearney, J G Fujimoto, and M E Brezinski. Forward-imaging instruments for optical coherence tomography. *Optics Letters*, 22(21):1618–1629, 1997.

[154] Xuan Liu, M J Cobb, Y Chen, M B Kimmey, and X Li. Rapid-scanning forward-imaging miniature endoscope for real-time optical coherence tomography. *Optics Letters*, 29(15):1763–1765, 2004.

[155] N R Munce, A Mariampillai, B A Stadish, M Pop, K J Anderson, G Y Liu, T Luk, B K Courtney, G A Wright, I A Vitkin, and V X D Yang. Electrostatic forward-viewing scanning probe for Doppler optical coherence tomography using a dissipative polymer catheter. *Optics Letters*, 33(7):657–659, 2008.

[156] J Wu, M Corny, C Gu, F Wang, Z Yaqoob, and C Yang. Paired-angle-rotation scanning optical coherence tomography forward-imaging probe. *Optics Letters*, 31(9):1265–1267, 2006.

[157] T Xie, D Mukai, S Guo, and Z Brenner M Chen. Fiber-optic-bundle-based optical coherence tomography. *Optics Letters*, 30(14):1803–1805, 2005.

[158] N V Iftimia, B E Bouma, M B Pitman, B Goldberg, J Bressner, and G J Tearney. A portable, low coherence interferometry based instrument for fine needle aspiration biopsy guidance. *Reviwe of Scientific Instruments*, 76, 2005.

[159] Marcin Balicki, Jae-Ho Han, Iulian Iordachita, Peter Gehlbach, James Handa, Russell Taylor, and Jin Kang. Single fiber optical coherence tomography microsurgical instruments for computer and robot-assisted retinal surgery. *Medical image computing and computer-assisted intervention : MICCAI ... International Conference on Medical Image Computing and Computer-Assisted Intervention*, 12(Pt 1):108–15, January 2009.

[160] Xuan Liu, Marcin Balicki, Russel H Taylor, and Jin U Kang. Towards automatic calibration of Fourier-Domain OCT for robot-assisted vitreoretinal surgery. *Opt Express*, 18(23), 2010.

[161] Jin H Shen, John Kozub, Ratna Prasad, and Karen M Joos. An Intraocular OCT Probe. *Invest. Ophthalmol. Vis. Sci.*, 52: E-Abst, 2011.

[162] Karen M Joos and Jin-Hui Shen. Miniature real-time intraoperative forward-imaging optical coherence tomography probe. *Biomedical optics express*, 4(8):1342–50, January 2013.

[163] Volker Westphal, Andrew Rollins, Sunita Radhakrishnan, and Joseph Izatt. Correction of geometric and refractive image distortions in optical coherence tomography applying Fermat's principle. *Optics express*, 10(9):397–404, May 2002.

[164] Jun Xie, Shuhuai Huang, Zhengcheng Duan, Yusheng Shi, and Shifeng Wen. Correction of the image distortion for laser galvanometric scanning system. *Optics & Laser Technology*, 37(4):305–311, June 2005.

[165] Adrian Podoleanu, Ismini Charalambous, Lucian Plesea, Aristide Dogariu, and Richard Rosen. Correction of distortions in optical coherence tomography imaging of the eye. *Physics in medicine and biology*, 49(7):1277–94, April 2004.

[166] Sergio Ortiz, Damian Siedlecki, Laura Remon, and Susana Marcos. Optical coherence tomography for quantitative surface topography. *Applied optics*, 48(35):6708–15, December 2009.

[167] Sergio Ortiz, Damian Siedlecki, Ireneusz Grulkowski, Laura Remon, Daniel Pascual, Maciej Wojtkowski, and Susana Marcos. Optical distortion correction in optical coherence tomography for quantitative ocular anterior segment by three-dimensional imaging. *Optics express*, 18(3):2782–96, February 2010.

[168] Jing Tian, Pina Marziliano, Mani Baskaran, Hong-Tym Wong, and Tin Aung. Automatic anterior chamber angle assessment for HD-OCT images. *IEEE transactions on bio-medical engineering*, 58(11):3242–9, November 2011.

[169] Cuiru Sun, Kenneth K. C. Lee, Barry Vuong, Michael Cusimano, Alexander Brukson, Adrian Mariampillai, Beau a. Standish, and Victor X. D. Yang. Neurosurgical hand-held optical coherence tomography (OCT) forward-viewing probe. 8207:82074V–82074V–8, 2012.

[170] Damian Siedlecki, Alberto de Castro, Enrique Gambra, Sergio Ortiz, David Borja, Stephen Uhlhorn, Fabrice Manns, Susana Marcos, and Jean-Marie Parel. Distortion correction of OCT images of the crystalline lens: gradient index approach. *Optometry and vision science : official publication of the American Academy of Optometry*, 89(5):E709–18, May 2012.

[171] Sergio Ortiz, Damian Siedlecki, Pablo Pérez-Merino, Noelia Chia, Alberto de Castro, Maciej Szkulmowski, Maciej Wojtkowski, and Susana Marcos. Corneal topography from spectral optical coherence tomography (sOCT). *Biomedical optics express*, 2(12):3232–47, December 2011.

[172] Jin U. Kang and Xuan Liu. Distortion corrected optical coherence tomography system.

[173] Xuan Liu, Yong Huang, and Jin U. Kang. Distortion-free freehand-scanning OCT implemented with real-time scanning speed variance correction. *Optics Express*, 20(15):16567, July 2012.

[174] Yujun Guo, Priya N Werahera, Ramkrishnan Narayanan, Lu Li, Dinesh Kumar, E David Crawford, and Jasjit S Suri. Image registration accuracy of a 3-dimensional transrectal ultrasound-guided prostate biopsy system. *Journal of ultrasound in medicine : official journal of the American Institute of Ultrasound in Medicine*, 28(11):1561–8, November 2009.

[175] V V Karnik, A Fenster, J Bax, D W Cool, L Gardi, I Gyacskov, C Romagnoli, and A D Ward. Assessment of image registration accuracy in three-dimensional transrectal ultrasound guided prostate biopsy. *Medical physics*, 37(2):802–13, February 2010.

[176] David G. Gobbi, Roch M. Comeau, and Terry M. Peters. *Medical Image Computing and Computer-Assisted Intervention MICCAI 2000*, volume 1935 of *Lecture Notes in Computer Science*. Springer Berlin Heidelberg, Berlin, Heidelberg, 2000.

[177] Jhimli Mitra, Arnau Oliver, Robert Marti, Xavier Llado, Joan C. Vilanova, and Fabrice Meriaudeau. Multimodal Prostate Registration Using Thin-Plate Splines from Automatic Correspondences. In *2010 International Conference on Digital Image Computing: Techniques and Applications*, pages 587–592. IEEE, December 2010.

[178] G Brandt, K Radermacher, S Lavallee, H.-W. Staudte, and G Rau. A Compact Robot for Image Guided Orthopedic Surgery: Concept and preliminary Results. volume 1205, pages 767–776. Springer, 1997.

[179] Guido Brandt, Andreas Zimolong, Lionel Carrat, Philippe Merloz, Hans-Walter Staudte, Stephane Lavallee, Klaus Radermacher, and Guenter Rau. CRIGOS: A compact robot for image-guided orthopedic surgery. *IEEE Transactions on Information Technology in Biomedicine*, 3(4):252–260, 1999.

[180] M Fadda, D Bertelli, S Martelli, M Marcacci, P Dario, C Pagetti, D Caramella, and D Trippi. Computer Assisted Planning for Total Knee Arthoplasty. volume 1205, pages 619–628. Springer, 1997.

[181] S J Harris, W J Lin, R D Hibberd, J Cobb, R Middelton, and B L Davies. Experiences with Robotic Systems for Knee Surgery. volume 1205, pages 757–766. Springer, 1997.

[182] S C Ho, R D Hibberd, and B L Davies. Robot Assisted Knee Surgery. 14(May/June):292–299, 1995.

[183] P Kazanzides, B D Mittelstadt, B L Musits, W L Bargar, J F Zuhars, B Williamson, Ph. W Cain, and E J Carbone. An Integrated System for Cementless Hip Replacement. 14:307–312, 1995.

[184] T C Kienzle, S D Stulberg, M Peshkin, A Quaid, J Lea, A Goswami, and C.-h. Wu. Total Knee Replacement. 14(May/June):301–306, 1995.

[185] Jongwon Lee, Keehoon Kim, Wan Kyun Chung, Seungmoon Choi, and Young Soo Kim. Human-guided surgical robot system for spinal fusion surgery: CoRASS. pages 3881–3887, Pasadena, CA, United states, 2008. Institute of Electrical and Electronics Engineers Inc.

[186] F Leitner, F Picard, R Minefelde, H-J. Schultz, P Cinquin, and D Saragaglia. Computer-Assisted Knee Surgical Total Replacement. volume 1205, pages 629–. Springer, 1997.

[187] M Shoham, M Burman, E Zehavi, L Joskowicz, E Batkilin, and Y Kunicher. Bone-Mounted Miniature Robot for Surgical Procedures: Concept and Clinical Applications. *IEEE Transactions on Robotics and Automation*, 19(5):893–901, 2003.

[188] Russell Taylor, H A Paul, Peter Kazanzides, B D Mittestadt, W Hanson, J F Zuhars, B Williamson, B L Mustits, E Glassman, and W L Bargar. An image-directed robotic system for precise orthopedic surgery. *IEEE Transactions on Robotics and Automation*, 10:261–275, 1994.

[189] Alon Wolf and Branislav Jaramaz. MBARS: Mini bone attached robotic system for joint arthroplasty. volume 2006, pages 1053–1058, Pisa, Italy, 2006. Institute of Electrical and Electronics Engineers Computer Society, Piscataway, NJ 08855-1331, United States.

[190] B L Davies, K L Fan, R D Hibberd, M Jakopec, and S J Harris. ACROBOT - using robots and surgeons synergistically in knee surgery. pages 173–178, Monterey, CA, USA, 1997. IEEE, Piscataway, NJ, USA.

[191] Brian Davies. A Review of Robotics in Surgery. *Proceedings of the Institution of Mechanical Engineers. Part H, Journal of engineering in medicine*, 214(1):129–40, January 2000.

[192] B L Davies, F M Rodriguez y Baena, A R W Barrett, M P S F Gomes, S J Harris, M Jakopec, and J P Cobb. Robotic control in knee joint replacement surgery. *Proceedings of the Institution of Mechanical Engineers, Part H: Journal of Engineering in Medicine*, 221(Compendex):71–80, 2007.

[193] Geoffrey N Box and Thomas E Ahlering. Robotic radical prostatectomy: long-term outcomes. 18:173–179, 2008.

[194] Geoffrey N Box, Hak J Lee, Ricardo J S Santos, Jose Benito A Abraham, Michael K Louie, Aldrin Joseph R Gamboa, Resa Alipanah, Leslie Deane, Elspeth M McDougall, and Ralph V Clayman. Robot-Assited NOTES Nephrectomy: Initial Report. 22(3):503–505, 2008.

[195] P Chatzilias, Z Kamarianakis, S Golemati, and M Christodoulou. Robotic control in hand-assisted laparoscopic nephrectomy in humans - A pilot study. volume 26 IV, pages 2742–2745, San Francisco, CA, United states, 2004. Institute of Electrical and Electronics Engineers Inc.

[196] Georges-Pascal Haber, Michael a White, Riccardo Autorino, Pedro F Escobar, Matthew D Kroh, Sricharan Chalikonda, Rakesh Khanna, Sylvain Forest, Bo Yang, Fatih Altunrende, Robert J Stein, and Jihad H Kaouk. Novel robotic da Vinci instruments for laparoendoscopic single-site surgery. *Urology*, 76(6):1279–82, December 2010.

[197] J W Cannon, J A Stoll, S D Selha, P E Dupont, R D Howe, and D F Torchiana. Port Placement Planning in Robot-Assisted Coronary Artery Bypass . *IEEE Transactions on Robotics and Automation*, 19(5):912–917, 2003.

[198] Amir Degani, Howie Choset, Alon Wolf, and Marco A Zenati. Highly Articulated Robotic Probe for Minimally Invasive Surgery. pages 4167–4172, Orlando, Florida, 2006.

[199] Samuel B Kesner and Robert D Howe. Design and control of motion compensation cardiac catheters. In *Proceedings - IEEE International Conference on Robotics and Automation*, pages 1059–1065, Anchorage, AK, United states, 2010.

[200] Takeyoshi Ota, Amir Degani, David Schwartzman, Brett Zubiate, Jeremy McGarvey, Howie Choset, and Marco A Zenati. A Novel Highly Articulated Robotic Surgical System For Epicardial Ablation. pages 250–253, Vancouver, British Columbia, Canada, 2008.

[201] Nicholas Patronik, Marco Zenati, and Cameron Riviere. Crawling on the heart: a mobile robotics device for minimally invasive cardiac interventions. volume LNCS 3217, pages 9–16, 2004.

[202] O Schnider, J Troccaz, O Chananon, and D Blin. PADyC: a Synergetic Robot for Cardiac Puncturing. pages 2883–2888, San Francisco, CA, 2000.

[203] A L Trejos and R V Patel. Port placement for endoscopic cardiac surgery based on robot dexterity optimization. volume 2005, pages 912–917, Barcelona, Spain, 2005. Institute of Electrical and Electronics Engineers Inc.

[204] Brian M Benway, Sam B Bhayani, Craig G Rogers, James R Porter, Nicolò M Buffi, Robert S Figenshau, and Alexandre Mottrie. Robot-Assisted Partial Nephrectomy: An International Experience. *European urology*, 57:815–820, January 2010.

[205] Craig Rogers M D. Robotic Partial Nephrectomy : Tips and Tricks. *Urology*.

[206] Tom Deklaj, David a Lifshitz, Sergey a Shikanov, Mark H Katz, Kevin C Zorn, and Arieh L Shalhav. Laparoscopic radical versus laparoscopic partial nephrectomy for clinical T1bN0M0 renal tumors: comparison of perioperative, pathological, and functional outcomes. *Journal of endourology / Endourological Society*, 24(10):1603–7, October 2010.

[207] Yu Gong, Chuanjun Du, David Y Josephson, Timothy G Wilson, and Rebecca Nelson. Four-arm robotic partial nephrectomy for complex renal cell carcinoma. *World journal of urology*, 28(1):111–5, February 2010.

[208] Sanjeev Kaul, Rajesh Laungani, Richard Sarle, Hans Stricker, James Peabody, Ray Littleton, and Mani Menon. da Vinci-assisted robotic partial nephrectomy: technique and results at a mean of 15 months of follow-up. *European urology*, 51(1):186–91; discussion 191–2, January 2007.

[209] Michael W Phelan, Kent T Perry, John Gore, and Peter G Schulam. Laparoscopic partial nephrectomy and minimally invasive nephron-sparing surgery. *Current urology reports*, 4(1):13–20, February 2003.

[210] Francesco Porpiglia. Editorial comments to "da Vinci-assisted robotic partial nephrectomy: technique and results at a mean of 15 months of follow-up". *European urology*, 51(1):191, 2007.

[211] Craig G Rogers, Adam Metwalli, Adam M Blatt, Gennady Bratslavsky, Mani Menon, W Marston Linehan, and Peter a Pinto. Robotic partial nephrectomy for renal hilar tumors: a multi-institutional analysis. *The Journal of urology*, 180(6):2353–6; discussion 2356, December 2008.

[212] Craig Rogers, Shyam Sukumar, and Inderbir S Gill. Robotic partial nephrectomy: the real benefit. *Current opinion in urology*, 21(1):60–4, January 2011.

[213] Libor Safarik. Editorial comments to "da Vinci-assisted robotic partial nephrectomy: technique and results at a mean of 15 months of follow-up". *European urology*, 51(1):192, 2007.

[214] L.-M. Su, B Vagvolgyi, R Agarwal, C Reiley, R Taylor, and G Hager. Augmented Reality During Robot-assisted Laparoscopic Partial Nephrectomy: Toward Real-Time 3D-CT to Stereoscopic Video Registration. 73:896–900, 2009.

[215] Gyung Tak Sung and Inderbir S Gill. Robotic Laparoscopic Surgery: a Comparison of the DA Vinci and Zeus Systems. 58(6):893–898, 2001.

[216] Murat Cenk Cavusoglu, W Williams, Frank Tendick, and Shankar Sastry. Robotics for Telesurgery: Second Generation Berkley/UCSF Laprascopic Telesurgical Workstation and Looking towards the Future Applications. Number 1, page Invited Paper, Monticello, Italy, 2001.

[217] Hiromasa Yamashita, Nobuhiko Hata, Makoto Hashizume, and Takeyoshi Dohi. Handheld Laprascopic Forceps manipulator Using Multi-slider Linkage Mechanisms. volume LNCS 3217, pages 121–128, 2004.

[218] G Dogangil, B L Davies, and F Rodriguez Y Baena. A review of medical robotics for minimally invasive soft tissue surgery. *Proceedings of the Institution of Mechanical Engineers, Part H: Journal of Engineering in Medicine*, 224(Compendex):653–679, 2010.

[219] Daisuke Asai, Surman Katopo, Jumpei Arata, Shin'ichi Warisawa, Mamoru Mitsuishi, Akio Morita, Shigeo Sora, Takaaki Kirino, and Ryo Mochizuki. Micro-Neurosurgical System in the Deep Surgical Field, 2004.

[220] Paolo Dario, Maria Chiara Carrozza, Eugenio Guglielmelli, Cecilia Laschi, Arianna Menciassi, Silvestro Micera, and Fabrizio Vecchi. Robotics as a future and emerging technology: Biomimetics, cybernetics, and neuro-robotics in European projects. 12(2):29–45, 2005.

[221] Kazuhiro Hongo, H Kobayashi, Yukinari Kakizawa, Jun-ichi Koyama, Tetsuya Goto, Hiroshi Okeudera, Kazutoshi Kan, Masakatsu Fujie, Hiroshi Iseki, and Kintomo Takakura. NeuRobot: Telecontrolled Micromanipulator System for Minimally Invasive Microneurosurgery - Preliminary Results. 51(4):985–988, 2002.

[222] Ryoichi Nakamura, Shigeo Omori, Yoshihiro Muragaki, Katsuhiro Miura, Masao Doi, Ichiro Sakuma, and Hiroshi Iseki. A robotic neurosurgery system with aut-

ofocusing motion control for mid-infrared laser ablation. Copenhagen, Denmark, 2006.

[223] Bert O'Malley and Gregory Weinstein. Robotic Anterior and Midline Skull Base Surgery: Preclinical Investigations. 69(2):s125–2128, 2007.

[224] A. Gijbels, N. Wouters, P. Stalmans, H. Van Brussel, D. Reynaerts, and E. Vander Poorten. Design and realisation of a novel robotic manipulator for retinal surgery. In *2013 IEEE/RSJ International Conference on Intelligent Robots and Systems*, pages 3598–3603. IEEE, November 2013.

[225] Hyosig Kang and J.T. Wen. Robotic knot tying in minimally invasive surgeries. In *IEEE/RSJ International Conference on Intelligent Robots and System*, volume 2, pages 1421–1426. IEEE, 2002.

[226] A Kapoor and R H Taylor. A Constrained Optimization Approach to Virtual Fixtures for Multi-Handed Tasks, 2008.

[227] Marcin Balicki, J H Han, I Iordachita, P Gehlbach, J Handa, Russel H Taylor, and Jin U Kang. Single fiber optical coherence tomography microsurgical instruments for computer and robot-assisted retinal surgery, 2009.

[228] Haoran Yu, Jin-Hui Hui Shen, Karen M. Joos, and Nabil Simaan. Design, calibration and preliminary testing of a robotic telemanipulator for OCT guided retinal surgery. In *2013 IEEE International Conference on Robotics and Automation*, pages 225–231. IEEE, May 2013.

[229] Haoran Yu, Jin-Hui Shen, Rohan J. Shah, Nabil Simaan, and Karen M. Joos. Evaluation of microsurgical tasks with OCT-guided and/or robot-assisted ophthalmic forceps. *Biomedical Optics Express*, 6(2):457, January 2015.

[230] F J LoRusso and R L Font. Use of agar in ophthalmic pathology: a technique to improve the handling and diagnosis of temporal artery biopsies, subfoveal membranes, lens capsules, and other ocular tissues. *Ophthalmology*, 106(11):2106–8, November 1999.

[231] Mohan N Iyer and Dennis P Han. An eye model for practicing vitreoretinal membrane peeling. *Archives of ophthalmology*, 124(1):108–10, January 2006.

[232] Tsuneo Yoshikawa. *Foundations of Robotics: Analysis and Control*. The MIT Press, 2003.

[233] A. A. Maciejewski and C. A. Klein. Obstacle Avoidance for Kinematically Redundant Manipulators in Dynamically Varying Environments. *The International Journal of Robotics Research*, 4(3):109–117, September 1985.

[234] Matthew T Witmer, George Parlitsis, Sarju Patel, and Szilárd Kiss. Comparison of ultra-widefield fluorescein angiography with the Heidelberg Spectralis() noncontact ultra-widefield module versus the Optos() Optomap(). *Clinical ophthalmology (Auckland, N.Z.)*, 7:389–94, January 2013.

[235] Daniel E Croft, Jano van Hemert, Charles C Wykoff, David Clifton, Michael Verhoek, Alan Fleming, and David M Brown. Precise montaging and metric quantification of retinal surface area from ultra-widefield fundus photography and fluorescein angiography. *Ophthalmic surgery, lasers & imaging retina*, 45(4):312–7, 2014.

[236] J M Schmitt, S H Xiang, and K M Yung. Speckle in optical coherence tomography. *Journal of biomedical optics*, 4(1):95–105, January 1999.

[237] Azadeh Yazdanpanah, Ghassan Hamarneh, Benjamin R Smith, and Marinko V Sarunic. Segmentation of intra-retinal layers from optical coherence tomography images using an active contour approach. *IEEE transactions on medical imaging*, 30(2):484–96, February 2011.

[238] Paul Hahn, Justin Migacz, Rachelle O'Connell, Joseph A Izatt, and Cynthia A Toth. Unprocessed real-time imaging of vitreoretinal surgical maneuvers using a microscope-integrated spectral-domain optical coherence tomography system. *Graefe's archive for clinical and experimental ophthalmology = Albrecht von Graefes Archiv für klinische und experimentelle Ophthalmologie*, 251(1):213–20, January 2013.

[239] Haoran Yu, JinHui Shen, Karen M. Joos, and Nabil Simaan. Calibration and Integration of B-mode Optical Coherence Tomography for Assistive Control in Robotic Micro-Surgery. *IEEE/ASME Transactions on Mechatronics (TMECH), doi:10.1109/TMECH.2016.2583259*, 2016.

[240] Xingchi He, Marcin Balicki, Peter Gehlbach, James Handa, Russell Taylor, and Iulian Iordachita. A Novel Dual Force Sensing Instrument with Cooperative Robotic Assistant for Vitreoretinal Surgery. *IEEE International Conference on Robotics and Automation : ICRA : [proceedings] IEEE International Conference on Robotics and Automation*, 2013:213–218, December 2013.

[241] Jorge Angeles. Automatic Computation of the Screw Parameters of Rigid-Body Motions. Part I: Finitely-Separated Positions. *Journal of Dynamic Systems, Measurement, and Control*, 108(1):32, 1986.

[242] Jorge Angeles. Automatic Computation of the Screw Parameters of Rigid-Body Motions. Part II: Infinitesimally-Separated Positions. *Journal of Dynamic Systems, Measurement, and Control*, 108(1):39, 1986.

[243] F.L. Bookstein. Principal warps: thin-plate splines and the decomposition of deformations. *IEEE Transactions on Pattern Analysis and Machine Intelligence*, 11, 1989.

[244] A. Nahvi and J.M. Hollerbach. The noise amplification index for optimal pose se-

lection in robot calibration. In *Proceedings of IEEE International Conference on Robotics and Automation*, volume 1, pages 647–654. IEEE.

[245] Yong Huang and Jin U Kang. Real-time reference A-line subtraction and saturation artifact removal using graphics processing unit for high-frame-rate Fourier-domain optical coherence tomography video imaging. *Optical Engineering*, 51(7):073203, July 2012.

[246] Kenneth W Grace. *Kinematic Design of An Ophthalmic Surgery Robot and Feature Extracting Bilateral Manipulation*. PhD thesis, 1995.

[247] Steve Charles, Hari Das, Timothy Ohm, Curtis Boswell, Guillermo Rodriguez, Robert Steele, and Dan Istrade. Dexterity-enhanced telerobotic microsurgery . pages 5–10, Monterey, CA, USA, 1997.

[248] Sungwook Yang, M. Balicki, R.A. MacLachlan, Xuan Liu, J.U. Kang, R.H. Taylor, and C.N. Riviere. Optical coherence tomography scanning with a handheld vitreoretinal micromanipulator. In *Engineering in Medicine and Biology Society (EMBC), 2012 Annual International Conference of the IEEE*, pages 948–951, Aug 2012.

[249] Karen M. Joos and Jin-Hui Shen. A miniature forward-imaging optical coherence tomography (OCT) probe. 8209:82090Z–82090Z–7, 2012.

[250] L.B. Rosenberg. Virtual fixtures: Perceptual tools for telerobotic manipulation. In *Virtual Reality Annual International Symposium, 1993., 1993 IEEE*, pages 76–82, Sep 1993.

[251] M.A. Nasseri, P. Gschirr, M. Eder, S. Nair, K. Kobuch, M. Maier, D. Zapp, C. Lohmann, and A. Knoll. Virtual fixture control of a hybrid parallel-serial robot for assisting ophthalmic surgery: An experimental study. In *Biomedical Robotics and Biomechatronics (2014 5th IEEE RAS EMBS International Conference on*, pages 732–738, Aug 2014.

[252] Cheol Song, Peter L. Gehlbach, and Jin U. Kang. Active tremor cancellation by a "smart" handheld vitreoretinal microsurgical tool using swept source optical coherence tomography. *Opt. Express*, 20(21):23414–23421, Oct 2012.

[253] Cheol Song, Dong Yong Park, Peter L. Gehlbach, Seong Jin Park, and Jin U. Kang. Fiber-optic oct sensor guided “smart” micro-forceps for microsurgery. *Biomed. Opt. Express*, 4(7):1045–1050, Jul 2013.

[254] Haoran Yu, Jin-Hui Shen, Rohan J. Shah, Nabil Simaan, and Karen M. Joos. Evaluation of microsurgical tasks with OCT-guided and/or robot-assisted ophthalmic forceps. *Biomedical Optics Express*, 6(2):457, January 2015.

[255] Karen Joos and Jin-Hui Shen. Preliminary Design and Evaluation of a B-Scan OCT-Guided Needle. *Photonics*, 1(3):260–266, sep 2014.

[256] Berk Gonenc, Peter Gehlbach, James Handa, Russell H Taylor, and Iulian Iordachita. Motorized force-sensing micro-forceps with tremor cancelling and controlled micro-vibrations for easier membrane peeling. In *Biomedical Robotics and Biomechatronics (2014 5th IEEE RAS & EMBS International Conference on*, pages 244–251. IEEE, 2014.

[257] M. Kendal Ackerman and Gregory S. Chirikjian. *Geometric Science of Information: First International Conference, GSI 2013, Paris, France, August 28-30, 2013. Proceedings*, chapter A Probabilistic Solution to the AX=XB Problem: Sensor Calibration without Correspondence, pages 693–701. Springer Berlin Heidelberg, Berlin, Heidelberg, 2013.